

DESIGN AND IMPLEMENTATION OF A WIRELESS PASSIVE SENSING SYSTEM FOR STRUCTURAL HEALTH MONITORING

A DISSERTATION SUBMITTED TO
THE GRADUATE SCHOOL OF ENGINEERING AND SCIENCE
OF BILKENT UNIVERSITY
IN PARTIAL FULFILLMENT OF THE REQUIREMENTS FOR
THE DEGREE OF
DOCTOR OF PHILOSOPHY
IN
ELECTRICAL AND ELECTRONICS ENGINEERING

By
Burak Özbey
June 2016

DESIGN AND IMPLEMENTATION OF A WIRELESS PASSIVE
SENSING SYSTEM FOR STRUCTURAL HEALTH MONITORING

By Burak Özbey

June 2016

We certify that we have read this dissertation and that in our opinion it is fully adequate, in scope and in quality, as a dissertation for the degree of Doctor of Philosophy.

Ayhan Altıntaş (Advisor)

Hilmi Volkan Demir (Advisor)

Vakur B. Ertürk (Advisor)

Ergin Atalar

Özgür Kurç

Sencer Koç

Özlem Aydın Çivi

Approved for the Graduate School of Engineering and Science:

Levent Onural
Director of the Graduate School

ABSTRACT

DESIGN AND IMPLEMENTATION OF A WIRELESS PASSIVE SENSING SYSTEM FOR STRUCTURAL HEALTH MONITORING

Burak Özbey

Ph.D. in Electrical and Electronics Engineering

Advisors: Ayhan Altıntaş, Hilmi Volkan Demir, Vakur B. Ertürk

June 2016

Structural health monitoring (SHM) aims to ensure detection and prevention of damage in structures and protection of human life via observation of certain damage indicators. In SHM, one of the most important damage indicators is the strain forming on the steel reinforcing bars (rebars) embedded inside concrete. This strain can slowly develop over time, or can suddenly occur due to an overload such as an earthquake. In this dissertation, a novel wireless passive sensing system is presented for detecting and measuring the level of strain and relative displacement in structures. The sensing system comprises a nested split-ring resonator (NSRR) probe along with a transceiver antenna. These two elements form an electromagnetically coupled system that yields very high sensitivity and resolution of displacement and strain sensing accompanied with a wide dynamic range of measurement. Using this wireless system, it is possible to track strain/displacement in both the elastic (reversible-linear) and plastic (irreversible-nonlinear) deformation regions of steel rebars. In the dissertation, the results of the following experiments are presented: Characterization experiments carried out on a translation stage in laboratory environment, tensile test experiments where a rebar is loaded with a pulling force until fracture, and simply supported beam experiments where a beam undergoes loading, which leads to tensile strains on rebars at the bottom of the beam. Especially, the simply supported beam experiments constitute a decisive step toward a real-life application of the proposed sensing system. The sensing system is shown to acquire accurate data until the end of the measurements in which the wired devices such as strain gages break down and fail to capture. Furthermore, the effects of the complex electromagnetic medium formed by the rebars and the concrete on sensing are investigated. In addition, a multi-point sensing capability via multiple probes and single antenna is proposed and experimentally demonstrated, which can be used in 2-D surface strain mapping with further improvements. Finally, an equivalent circuit model is

given for the NSRR structure, the results of which are compared to and found to be in good agreement with full-wave simulations and measurements. This study shows that the designed sensing system has the potential to be an alternative for both microstrain-level SHM and large displacement measurements, which can be useful for post-earthquake damage assessment.

Keywords: Structural health monitoring, wireless passive sensors, displacement/strain sensors, nested split ring resonators, complex electromagnetic medium, multi-point sensing, equivalent circuit model.

ÖZET

YAPISAL SAĞLIK İZLEME İÇİN KABLOSUZ PASİF BİR ALGILAYICI SİSTEMİN TASARLANMASI VE GERÇEKLEŞTİRİLMESİ

Burak Özbey

Elektrik ve Elektronik Mühendisliği, Doktora

Tez Danışmanları: Ayhan Altıntaş, Hilmi Volkan Demir, Vakur B. Ertürk

Haziran 2016

Yapısal sağlık izleme, belirli hasar göstergelerinin gözlemlenerek, yapılarda hasarın tespit edilmesini ve önüne geçilmesini ve insan yaşamının korunmasını amaçlar. Yapısal sağlık izlemedeki en önemli hasar göstergelerinden biri, betonun içinde gömülü halde bulunan çelik donatılarda oluşan gerinimdir. Bu gerinim, zaman içerisinde yavaşça oluşabileceği gibi, deprem gibi aşırı yüklemeler sonucu birdenbire de meydana gelebilir. Bu çalışmada, yapılarda oluşan gerinim ve bağıl yer değiştirme seviyelerinin algılanarak ölçülmesi amaçlı yeni bir kablosuz pasif algılayıcı sistem sunulmaktadır. Algılayıcı sistem, bir iç içe geçmiş yarık-halka rezonatör prob (NSRR) ile alıcı-verici bir antenden oluşmaktadır. Bu iki eleman elektromanyetik bağlaşık bir sistem oluşturarak çok yüksek bir hassasiyet ve çözünürlük ile beraber geniş bir dinamik menzili mümkün kılmaktadır. Bu sistemle, çelik donatıların elastik (geri döndürülebilir-doğrusal) ve plastik (geri döndürülemez-doğrusal olmayan) deformasyon bölgelerindeki gerinim/yer değiştirmeyi takip etmek mümkündür. Bu çalışmada, şu deneyler için sonuçlar verilmektedir: Laboratuvar ortamında yer değiştirme düzeneğinde gerçekleştirilen karakterizasyon deneyleri, çelik bir donatının kırılmaya kadar çekici bir kuvvet ile yüklendiği çekme deneyleri ve bir kirişin yüklenerek kirişin aşağısında bulunan donatılarda uzamanın gözlemlendiği basit mesnetli kiriş deneyleri. Özellikle, basit mesnetli kiriş deneyleri, önerilen algılayıcı sistemin gerçek hayat uygulaması olarak kullanılması yolunda son basamak olma özelliği taşımaktadır. Algılayıcı sistemin, gerinim pulu gibi kablolu aygıtların bozulup ölçüm yapamadıkları noktalardan çok daha sonra bile doğru olarak veri almaya devam ettiği gösterilmektedir. Ayrıca, donatılar ve betonun oluşturduğu karmaşık elektromanyetik ortamın algılamaya olan etkileri de incelenmektedir. Bunlara ek olarak, geliştirildiği takdirde ileride iki boyutlu gerinim haritası çıkarma gibi uygulamalarda yararlanılabilecek, birden çok prob ve tek anten ile gerçekleştirilen bir çoklu algılama

kabiliyeti öne sürülüp deneylerle kanıtlanmaktadır. Son olarak, NSRR yapısı için bir eşdeğer devre modeli önerilmekte, bu modelin sonuçlarının, tam dalga benzetimler ve ölçüm sonuçlarıyla örtüştüğü gösterilmektedir. Bu çalışma, tasarlanan algılayıcı sistemin mikrogerinim seviyesinde yapısal sağlık izleme uygulamaları ile deprem sonrası hasar tespiti açısından faydalı olabilecek yüksek seviyedeki yer değiştirmelerin ölçülmesi için de bir alternatif oluşturma potansiyeli olduğunu ortaya koymaktadır.

Anahtar sözcükler: Yapısal sağlık izleme, kablosuz pasif algılayıcılar, yer değiştirme/gerinim algılayıcıları, iç içe geçmiş yarık halka rezonatörleri, karmaşık elektromanyetik ortam, çoklu algılama, eşdeğer devre modeli.

Acknowledgement

I would like to express my gratitude to Prof. Ayhan Altıntaş, Prof. Hilmi Volkan Demir and Prof. Vakur Ertürk for acting as supervisors during my PhD Studies. Although challenging at times, without a doubt, working with three advisors also has many advantages: One can learn many things and can gain different insights, as well as benefit from ideas and points of view coming from different backgrounds at approaching a problem. Their valuable guidance has been of much help to me. I hope I will have a chance to cooperate with them in some way also in the future.

This PhD dissertation is the product of a multidisciplinary study combining electrical and civil engineering. I would also like to thank Prof. Özgür Kurç for instructing me about everything related with the civil engineering side of this work, and designing and superintending the METU experiments. Working closely with him, I had a chance to learn many interesting things about a completely different discipline, which I am sure will help me in many different ways.

I would like to thank Prof. Ergin Atalar for taking part in my thesis monitoring committee and also for reading and evaluating my dissertation.

I would also like to thank Prof. Sencer Koç and Prof. Özlem Aydın Çivi for agreeing to evaluate my dissertation as jury members.

I would like to acknowledge the valuable efforts of Dr. Ramazan Özçelik, Utku Albostan, Deniz Ruhi Yalçın, Özlem Temel and Hasan Metin in preparation of the setup and conducting of the experiments in Middle East Technical University.

I also thank Emre Ünal and our other research group members, my officemates, and staff of our department for their help.

I also acknowledge the financial support of TÜBİTAK, which has funded this study under the EEEAG grant no. 112E255.

Finally, I would like to thank my mother and my father, who have supported me in everything I have done in my life. I am sure that it would be impossible to complete this dissertation without their encouragement.

Contents

1	Introduction	1
2	Sensing System	9
2.1	Components of the Sensing System	9
2.1.1	NSRR probe	9
2.1.2	Antenna	12
2.2	Operation Principles of the Sensing System	13
2.3	Characterization of the Sensing System with Experiments	18
2.3.1	Frequency shift with d	18
2.3.2	Resolution	24
2.3.3	Sensitivity	24
2.3.4	Linearity	25
2.3.5	Dynamic range and monitoring distance (D_m)	26
2.3.6	The coupling frequency pattern	33
2.3.7	Misalignments of the NSRR probe	36
3	Tensile Testing of the Sensing System	40
3.1	Elastic deformation region	41
3.1.1	Effect of the concrete cover	46
3.2	Plastic deformation region	49
4	Effects of the Complex Electromagnetic Medium on Sensing	53
4.1	Transmission through and reflection from the reinforced concrete .	55
4.2	Numerical fit to the calibration curve	58
4.3	Measurements in complex media	61
4.3.1	Effect of the rebar grid	62

4.3.2	Effect of the concrete cover	65
4.3.3	Effect of the backside reinforced concrete	68
5	Simply Supported Beam Experiments	73
5.1	Experiment setup	74
5.2	Elastic deformation region	78
5.3	Discrete-time measurements	85
5.4	Plastic deformation region	86
6	Multi-point Sensing by Multiple Probes	94
6.1	Experimental validation	96
6.2	Inter-coupling between the probes	101
7	Equivalent Circuit Model of the NSRR	105
7.1	Parameters of the model	106
7.1.1	Capacitance between two coplanar strips (C_s)	108
7.1.2	Average inductance of a strip (L_s)	110
7.1.3	Capacitance between a coplanar opposing strip pair (C_{gap})	115
7.1.4	Inductance of the thin jumper wire (L_{wire})	116
7.2	Comparison with experiments and simulations	119
8	Conclusions	124
A	Coefficient of determination (R^2)	127

List of Figures

2.1	Top: Modified NSRR structure for displacement/strain measurement in structural health monitoring, Bottom: Regular NSRR structure.	10
2.2	Modified NSRR structure designs with different resonance frequencies.	13
2.3	The photograph of the fabricated microstrip single-slot antenna: a) Front side with the slot, b) Backside with the feedline.	14
2.4	The measured and simulated reflection coefficient versus frequency for the microstrip single-slot antenna.	15
2.5	a) Electric field map numerically calculated on the antenna, on the 1-mm-separated NSRR probe, and at several cross-sections between the antenna and the probe when the simulation frequency is the resonance frequency of $d = 1$ mm (406 MHz), and b) when $d = 1$ mm again but the simulation frequency is 448 MHz (off-resonance case for $d = 1$ mm). (Reprinted, with permission, from “Wireless Displacement Sensing Enabled by Metamaterial Probes for Remote Structural Health Monitoring,” by B. Ozbey, E. Unal, H. Ertugrul, O. Kurc, C. M. Puttlitz, V. B. Erturk, H. V. Demir and A. Altintas, <i>Sensors</i> , under the Creative Commons Attribution License (http://creativecommons.org/licenses/by/4.0/).)	16

2.6 a) Electric field map on the antenna, on the 5-mm-separated NSRR probe and at several cross-sections between the antenna and the probe when the simulation frequency is the resonance frequency of $d = 5$ mm (448 MHz), and b) when $d = 5$ mm again but the simulation frequency is 406 MHz (off-resonance case for $d = 5$ mm).(Reprinted, with permission, from “Wireless Displacement Sensing Enabled by Metamaterial Probes for Remote Structural Health Monitoring,” by B. Ozbey, E. Unal, H. Ertugrul, O. Kurc, C. M. Puttlitz, V. B. Erturk, H. V. Demir and A. Altintas, Sensors, under the Creative Commons Attribution License (<http://creativecommons.org/licenses/by/4.0/>).) 17

2.7 The displacement experiment setup including the sensing system elements and the xyz translation stage. (Reprinted, with permission, from “Wireless Displacement Sensing Enabled by Metamaterial Probes for Remote Structural Health Monitoring,” by B. Ozbey, E. Unal, H. Ertugrul, O. Kurc, C. M. Puttlitz, V. B. Erturk, H. V. Demir and A. Altintas, Sensors, under the Creative Commons Attribution License (<http://creativecommons.org/licenses/by/4.0/>).) 20

2.8 The change of antenna reflection coefficient via a change in d . The case where NSRR probe is not present represents only the antenna response. (Reprinted, with permission, from “Wireless Measurement of Elastic and Plastic Deformation by a Metamaterial-Based Sensor” by B. Ozbey, H. V. Demir, O. Kurc, V. B. Erturk and A. Altintas, Sensors, under the Creative Commons Attribution License (<http://creativecommons.org/licenses/by/4.0/>).) 21

2.9 The full system simulation mimicking the displacement experiments. a) The simulation setup, b) The simulation results showing the shift of frequency peaks in antenna reflection coefficient as d is varied from 0 to 10 mm. 23

2.10 The displacement experiment results where d is varied from 1 to 10 mm: a) The shift of frequency peaks, b) The change of the NSRR probe resonance frequency obtained from the experiment and simulation. A more linear portion of the curve (3 to 8 mm) is given as an inset on top left. (Reprinted, with permission, from “Wireless Displacement Sensing Enabled by Metamaterial Probes for Remote Structural Health Monitoring,” by B. Ozbey, E. Unal, H. Ertugrul, O. Kurc, C. M. Puttlitz, V. B. Erturk, H. V. Demir and A. Altintas, *Sensors*, under the Creative Commons Attribution License (<http://creativecommons.org/licenses/by/4.0/>).) 23

2.11 The displacement experiment results where d is changed from 2.8 mm to 2.82 mm in 0.5 μm steps. 24

2.12 Dynamic range of the sensing system plotted for different monitoring distances D_m at a tracking threshold of 1 dB. (Reprinted, with permission, from “Wireless Displacement Sensing Enabled by Metamaterial Probes for Remote Structural Health Monitoring,” by B. Ozbey, E. Unal, H. Ertugrul, O. Kurc, C. M. Puttlitz, V. B. Erturk, H. V. Demir and A. Altintas, *Sensors*, under the Creative Commons Attribution License (<http://creativecommons.org/licenses/by/4.0/>).) 28

2.13 a) The points on which the NSRR probe is positioned for the coupling pattern experiment, b) Color map demonstrating the coupling strength between the NSRR probe and the antenna in a 2-D pattern. The antenna position is also shown on the plot ($D_m = 10$ cm). 30

2.14 Experiment at $D_m = 30$ cm: a) $|S_{11}|$ curves obtained from an experiment where d is changed from 0 to 10 mm in 10 steps, b) $|S_{11}|$ curves from which $|S_{11}|_0$ is subtracted. 32

2.15 Experiment at $D_m = 50$ cm: Consecutive subtraction of $|S_{11}|_{i-1}$ curves from $|S_{11}|_i$ curves. In the experiment, d is changed from 0 to 10 mm in 10 steps. 33

2.16 Color map demonstrating the coupling frequency, that is, the resonance frequency of the NSRR probe observed in the antenna reflection coefficient through electromagnetic coupling in a 2-D pattern. The antenna position is also shown on the plot. The values in the color bar are in MHz. 34

2.17 The change of the NSRR probe resonance frequency observed from the antenna reflection coefficient for different positions of the probe in x - and y -axes. d is changed from 1.4 mm to 3.4 mm in 0.2 mm steps at all points. 35

2.18 A possible misalignment where two NSRR probe parts on a rebar are rotated on the same plane. 36

2.19 Inward bending of the NSRR probe parts characterized by recording the shift of sensing system frequency with d , given for three different angles: 5° , 10° and 15° . (Reprinted, with permission, from “Wireless Measurement of Elastic and Plastic Deformation by a Metamaterial-Based Sensor” by B. Ozbey, H. V. Demir, O. Kurc, V. B. Erturk and A. Altintas, Sensors, under the Creative Commons Attribution License (<http://creativecommons.org/licenses/by/4.0/>).) 37

2.20 Outward bending of the NSRR probe parts characterized by recording the shift of sensing system frequency with d , given for three different angles: 5° , 10° and 15° . (Reprinted, with permission, from “Wireless Measurement of Elastic and Plastic Deformation by a Metamaterial-Based Sensor” by B. Ozbey, H. V. Demir, O. Kurc, V. B. Erturk and A. Altintas, Sensors, under the Creative Commons Attribution License (<http://creativecommons.org/licenses/by/4.0/>).) 38

2.21 Twisting of the NSRR probe parts characterized by recording the shift of sensing system frequency with d , given for three different angles: 10° , 20° and 30° . (Reprinted, with permission, from “Wireless Measurement of Elastic and Plastic Deformation by a Metamaterial-Based Sensor” by B. Ozbey, H. V. Demir, O. Kurc, V. B. Erturk and A. Altintas, Sensors, under the Creative Commons Attribution License (<http://creativecommons.org/licenses/by/4.0/>).) 39

3.1 The tensile test setup shown with the sensing system elements antenna and the NSRR probe on a standard 8-mm diameter rebar. (Reprinted, with permission, from “Wireless Measurement of Elastic and Plastic Deformation by a Metamaterial-Based Sensor” by B. Ozbey, H. V. Demir, O. Kurc, V. B. Erturk and A. Altintas, Sensors, under the Creative Commons Attribution License (<http://creativecommons.org/licenses/by/4.0/>).) 41

3.2 The installment of the strain gages and the NSRR probe shown on a cross section of the rebar. The sums of the strains read from the elements across each other are assumed to be the same. 43

3.3 Elastic region experiment: a) The applied force versus time, b) Stress versus microstrain measured by the sensor, compared to the average of the strain gage readings. Corresponding resonance frequencies are also displayed on the upper horizontal-axis, c) Shift of the frequency minima over time as the force is linearly increased, which is used to plot (b). (Reprinted, with permission, from “Wireless Displacement Sensing Enabled by Metamaterial Probes for Remote Structural Health Monitoring,” by B. Ozbey, E. Unal, H. Ertugrul, O. Kurc, C. M. Puttlitz, V. B. Erturk, H. V. Demir and A. Altintas, Sensors, Sensors, under the Creative Commons Attribution License (<http://creativecommons.org/licenses/by/4.0/>).) 44

3.4 Elastic region experiment: a) Applied periodic force regime versus time, b) Strain measured in time by the sensing system compared to the average strain gage data. (Reprinted, with permission, from “Wireless Measurement of Elastic and Plastic Deformation by a Metamaterial-Based Sensor” by B. Ozbey, H. V. Demir, O. Kurc, V. B. Erturk and A. Altintas, Sensors, under the Creative Commons Attribution License (<http://creativecommons.org/licenses/by/4.0/>).) 45

3.5 Elastic region experiment with concrete cover: a) The measurement setup with the concrete block serving as the clear cover, b) Strain measured in time by the sensing system compared to the average strain gage data. (Reprinted, with permission, from “Wireless Measurement of Elastic and Plastic Deformation by a Metamaterial-Based Sensor” by B. Ozbey, H. V. Demir, O. Kurc, V. B. Erturk and A. Altintas, Sensors, under the Creative Commons Attribution License (<http://creativecommons.org/licenses/by/4.0/>).) 48

3.6 Typical stress-strain curve of steel. 50

3.7 Plastic region strain and displacement measurements: a) The applied force, b) Displacement data from the sensing system compared to the extensometer data. Corresponding resonance frequencies of the sensor are also given on the right vertical axis. Top left: Zoomed elastic region (inset), c) Stress versus strain acquired from the sensor and from the extensometer. Bottom right: Zoomed elastic region (inset). (Reprinted, with permission, from “Wireless Measurement of Elastic and Plastic Deformation by a Metamaterial-Based Sensor” by B. Ozbey, H. V. Demir, O. Kurc, V. B. Erturk and A. Altintas, Sensors, under the Creative Commons Attribution License (<http://creativecommons.org/licenses/by/4.0/>).) 52

4.1 Configuration of the sensing system elements in a real-life application. (Reprinted, with permission, from “Wireless Sensing in Complex Electromagnetic Media: Construction Materials and Structural Monitoring” by B. Ozbey, H. V. Demir, O. Kurc, V. B. Erturk and A. Altintas, IEEE Sensors Journal © 2015 IEEE.) . . . 54

4.2 a) The simulated rebar grid lattice, b) Transmission through and reflection from a rebar grid lattice with the dimensions $P = 7.62$ cm and $D = 1.91$ cm. 56

4.3 Transmission through and reflection from a concrete wall with the following properties: $\epsilon_r = 6$, $\sigma = 1.95$ mS/m, $W = 20.3$ cm. 56

4.4 Transmission through and reflection from a reinforced concrete wall with the following properties: $P = 7.62$ cm, $D = 1.91$ cm and $W = 15.2$ cm. 57

4.5 Measured sensor resonance frequency as a function of displacement (d), shown for different jumper wire lengths (l). Measurement performed on an xyz translation stage, where no rebar or concrete is present around the sensor elements. 59

4.6 Measured change of sensor resonance frequency with displacement (d) for different jumper wire lengths (l), where $f(d = 0)$ is subtracted from each curve. Measurement performed on a translation stage, where no rebar or concrete is present around the sensor elements. 60

4.7 Change of the NSRR probe resonance frequency from measurement and numerical fit, for varying d , parametrized with respect to l . The numerical fit is exponential, which is plotted for each l . Measurement performed on a translation stage, where no rebar or concrete is present around the sensor elements. 61

4.8 A fragment of the rebar grid placed behind the NSRR probe in a) vertical and b) horizontal positions. The backside images are shown in (c) and (d). (Reprinted, with permission, from “Wireless Sensing in Complex Electromagnetic Media: Construction Materials and Structural Monitoring” by B. Ozbey, H. V. Demir, O. Kurc, V. B. Erturk and A. Altintas, IEEE Sensors Journal © 2015 IEEE.) 63

4.9 Translation stage measurements of the change of the sensor resonance frequency with d at the no-rebar case and for the cases of vertical and horizontal placement of the rebar grid fragment behind the NSRR probe, shown along with the exponential fits for each case. $l = 2$ cm in all cases. 64

4.10 Experimental setup of the scenario in which a 4 cm thick concrete plate is present between the antenna and the NSRR probe. (Reprinted, with permission, from “Wireless Sensing in Complex Electromagnetic Media: Construction Materials and Structural Monitoring” by B. Ozbey, H. V. Demir, O. Kurc, V. B. Erturk and A. Altintas, IEEE Sensors Journal © 2015 IEEE.) 66

4.11 Measured change of the sensing system frequency with varying displacement for different placements of the 4 cm thick concrete plate between the antenna and the NSRR probe. (Reprinted, with permission, from “Wireless Sensing in Complex Electromagnetic Media: Construction Materials and Structural Monitoring” by B. Ozbey, H. V. Demir, O. Kurc, V. B. Erturk and A. Altintas, IEEE Sensors Journal © 2015 IEEE.) 66

4.12 Measured resolution of the sensing system in the presence of a 4-cm-thick concrete plate: Sensing system frequency versus d for a 30 μm range with 1 μm steps, where $l = 4$ cm. 67

4.13 Experimental setup for the measurement of frequency change versus displacement when a concrete block is present behind the NSRR probe. (Reprinted, with permission, from “Wireless Sensing in Complex Electromagnetic Media: Construction Materials and Structural Monitoring” by B. Ozbey, H. V. Demir, O. Kurc, V. B. Erturk and A. Altintas, IEEE Sensors Journal © 2015 IEEE.) 68

4.14 Measured change of sensing system frequency when the concrete block is behind the NSRR probe, shown for several concrete block distances. The exponential fits are also shown. 69

4.15 Graphical representation of the change of the fit parameters k_1 and k_2 with concrete block distance to the NSRR probe. 70

4.16 Change of frequency with displacement for three different concrete samples with varying ages and rebar grid presence. The blocks are placed at a distance of 2 cm behind the NSRR probe. 72

5.1 a) The arrangement of the NSRR probes actually used in the experiment at the bottom of the beam, b) Close-up of a strain gage attached on a rebar before the concrete beam is produced, c) Placement of the protective plexiglass cover in front of the NSRR sensors (not the actual setup used in the experiment, but from a beam sample used for the preliminary tests before the actual experiment), d) Placement of the antenna at the bottom of the beam, which is closed with a plaster layer after the placement of the sensors and the plexiglass cover, e) Simply supported beam experiment setup, where the slot antenna and a representative NSRR probe are shown at one side of the beam (the preliminary test setup). (Reprinted, with permission, from “A Wireless Passive Sensing System for Displacement/Strain Measurement in Reinforced Concrete Members” by B. Ozbey, V.B. Erturk, H.V. Demir, A. Altintas and O. Kurc, *Sensors*, under the Creative Commons Attribution License (<http://creativecommons.org/licenses/by/4.0/>).) 75

5.2 The 1-cm thick polystyrene foam separators fastened to the backsides of the NSRR probes. (Reprinted, with permission, from “A Wireless Passive Sensing System for Displacement/Strain Measurement in Reinforced Concrete Members” by B. Ozbey, V.B. Erturk, H.V. Demir, A. Altintas and O. Kurc, *Sensors*, under the Creative Commons Attribution License (<http://creativecommons.org/licenses/by/4.0/>).) 76

5.3 Elastic deformation region experiment results of NSRR #1: a) Applied vertical force read from the load cell, b) Shifting of the NSRR #1 resonance frequency peaks with strain forming due to applied load, c) NSRR #1 peak frequency plotted by using the raw reflection coefficient data (blue), after a low-pass filter is applied to the raw data (red), and after 5th degree polynomial fitting is applied to the raw data (green), d) The transformation curve obtained in laboratory before the beam experiments by a controlled translational stage, which is used for converting the frequency shift into displacement and strain, e) Strain obtained by the NSRR #1 plotted versus time, and compared to the data from the strain gages. (Reprinted, with permission, from “A Wireless Passive Sensing System for Displacement/Strain Measurement in Reinforced Concrete Members” by B. Ozbey, V.B. Erturk, H.V. Demir, A. Altintas and O. Kurc, Sensors, under the Creative Commons Attribution License (<http://creativecommons.org/licenses/by/4.0/>).) 80

5.4 Elastic deformation region experiment results of NSRR #2: a) Applied vertical force read from the load cell, b) Shifting of the NSRR #2 resonance frequency peaks with strain forming due to applied load, c) Strain obtained from NSRR #2 plotted versus time, and compared to the data from the strain gages. (Reprinted, with permission, from “A Wireless Passive Sensing System for Displacement/Strain Measurement in Reinforced Concrete Members” by B. Ozbey, V.B. Erturk, H.V. Demir, A. Altintas and O. Kurc, Sensors, under the Creative Commons Attribution License (<http://creativecommons.org/licenses/by/4.0/>).) 83

5.5 Elastic deformation region experiment results of NSRR #3: a) Applied vertical force read from the load cell, b) Shifting of the NSRR #3 resonance frequency peaks with strain forming due to applied load, c) Strain obtained from NSRR #3 plotted versus time, and compared to the data from the strain gages. (Reprinted, with permission, from “A Wireless Passive Sensing System for Displacement/Strain Measurement in Reinforced Concrete Members” by B. Ozbey, V.B. Erturk, H.V. Demir, A. Altintas and O. Kurc, Sensors, under the Creative Commons Attribution License (<http://creativecommons.org/licenses/by/4.0/>).) 84

5.6 Discrete-time measurements: a) Applied force levels, b) Strain read by the sensing system with NSRR #2 and by strain gages, plotted versus time, c) Average of the strain values for each force level plotted versus the force. (Reprinted, with permission, from “A Wireless Passive Sensing System for Displacement/Strain Measurement in Reinforced Concrete Members” by B. Ozbey, V.B. Erturk, H.V. Demir, A. Altintas and O. Kurc, Sensors, under the Creative Commons Attribution License (<http://creativecommons.org/licenses/by/4.0/>).) 87

5.7 Plastic deformation region measurements: a) Applied vertical force read from the load cell, b) Absolute vertical displacement of the midpoint at the bottom of the beam (LVDT reading), c) The beam sample with visible cracks after the experiments. (Reprinted, with permission, from “A Wireless Passive Sensing System for Displacement/Strain Measurement in Reinforced Concrete Members” by B. Ozbey, V.B. Erturk, H.V. Demir, A. Altintas and O. Kurc, Sensors, under the Creative Commons Attribution License (<http://creativecommons.org/licenses/by/4.0/>).) 88

5.8 Plastic deformation region measurements: a) Shifting of NSRR #1 resonance peaks, b) Strain obtained by NSRR #1 plotted versus time, and compared to the data from the strain gages until the strain gages break down, c) The force-strain curve plotted with both NSRR #1 and strain gage data. (Reprinted, with permission, from “A Wireless Passive Sensing System for Displacement/Strain Measurement in Reinforced Concrete Members” by B. Ozbey, V.B. Erturk, H.V. Demir, A. Altintas and O. Kurc, Sensors, under the Creative Commons Attribution License (<http://creativecommons.org/licenses/by/4.0/>).) 90

5.9 Plastic deformation region measurements: a) Shifting of NSRR #1 resonance peaks, b) Strain obtained by NSRR #1 plotted versus time, and compared to the data from the strain gages until the strain gages break down, c) The force-strain curve plotted with both NSRR #1 and strain gage data, d) The piece of concrete stuck in NSRR #2 during the experiment. (Reprinted, with permission, from “A Wireless Passive Sensing System for Displacement/Strain Measurement in Reinforced Concrete Members” by B. Ozbey, V.B. Erturk, H.V. Demir, A. Altintas and O. Kurc, Sensors, under the Creative Commons Attribution License (<http://creativecommons.org/licenses/by/4.0/>).) 92

6.1 Concept of the proposed multi-point wireless passive architecture consisting of n nested split ring resonator (NSRR) probes and wireless spectral sensing response of each sensor shown on the frequency-antenna input impedance characteristics. 95

6.2 a) The shift of resonance frequency for each NSRR probe in the sensor array ($n = 3$) when d is increased from d_0 to $d_0 + 1$ mm. $D_m = 10$ cm. The resonance frequencies of the probes are determined by modification of d_0 . Left (inset): Experiment setup. Right (inset): Photograph of the NSRR probe employed in the experiment, b) The change of the resonance frequency versus the change in d for each probe. 97

6.3 a) The shift of resonance frequency for each NSRR probe in the sensor array ($n = 2$) when d is increased from 2.5 to 3.5 mm. $D_m = 10$ cm. The resonance frequencies of the probes are determined by modification of l , where $l_1 = 5$ cm and $l_2 = 4$ cm, b) The change of the resonance frequency versus the change in d for each probe. 98

6.4 a) The result of an experiment where $n = 6$: Initial case is shown in blue, the case where d is slightly increased for NSRR # 6 is shown in red, and the case where d is slightly increased for NSRR # 1 is shown in green. All other d 's remain the same. The experiment setup is shown in the right bottom corner. b) Simulation results of a 4×4 array ($n = 16$) with d varying between 1 to 4 mm in 0.2 mm steps, and when d is increased by $100 \mu\text{m}$ 100

6.5 Experiments related to the inter-coupling in the sensing system where $n = 2$: a) Fractional variation in the resonance frequency of an NSRR probe ($l_1 = 4$ cm) when another probe ($l_2 = 8$ cm) is located at edge-to-edge distances (D_c) varying from 0 to 40 mm along top, bottom, right and left axes. $d = 0$ for both probes, b) Same experiment except the resonance frequencies are set by assigning the probes different d_0 's instead of different l 's. $d_1 = 2$ mm, $d_2 = 0$, and $l = 3.5$ mm for both cases. 103

7.1 Nested split-ring resonator geometry modified for displacement sensing with design parameters. 106

7.2 Parameters of the proposed equivalent model geometry for NSRRs. 107

7.3 Parameters of a single-layer coplanar stripline shown on a schematic. 108

7.4 Calculation of the mutual inductance M_{total} between parallel strips for $N = 4, 5, 6$ 112

7.5 Geometry for calculating the mutual inductance between two parallel wire segments. 113

7.6 Calculation of the mutual inductance $M_{r,total}$ between opposing strips for several N values. 115

7.7 The change of average strip inductance L_s with the number of strips N 117

7.8 A typical transmission spectrum plot obtained via the proposed equivalent model, where the magnitude and phase of S_{21} are shown. Here, $N = 29$, $d = 0$ and $l = 0$ 120

7.9 The change of f_{res} with N , shown for both equivalent model and full-wave simulations. Here, $d = 0$ and $l = 0$ 120

7.10 Change of resonance frequency, f_{res} , with displacement between the opposing strips, d , that is obtained from the equivalent circuit model, is compared to measurement and full-wave simulation. $l = 4$ cm for simulations and measurement. 122

7.11 Change of resonance frequency, f_{res} , with shorting wire length, l , that is obtained from the equivalent circuit model, compared to measurement and full-wave simulation. $d = 4$ mm for simulations and measurement. 122

7.12 Change of resonance frequency, f_{res} , with physical NSRR parameters, w , D and l_t , that is obtained from the equivalent circuit model, compared to full-wave simulation ($N = 29$, $d = 0$, and $l = 0$). 123

List of Tables

- 2.1 Properties of the two NSRR designs employed in this work 12
- 2.2 Sensitivity and linearity levels observed for different ranges of d for the d - f_{res} curve given in Figure 2.10-b. 26
- 4.1 Modification of fit parameters when a rebar grid is placed behind the NSRR probe in vertical and horizontal positions. 65
- 4.2 Modification of fit parameters when a concrete block is placed behind the NSRR probe at several distances. 70
- 7.1 The change of L_{wire} with l ($r_w = 0.1$ mm) 117
- 7.2 Equivalent model parameter values for different N and d computed for Design A, where $w = 0.800$ mm, $D = 0.800$ mm, $l_s = 21.6$ mm, $h = 0.508$ mm, and $\epsilon_r = 3.2$ (all capacitances are in pF; all inductances are in nH; d in mm). 118

Chapter 1

Introduction

Structural health monitoring (SHM) is a field with growing worldwide interest that is critical to ensure both the reliability of structures and the protection of human life. One of the most important damage indices in SHM is the relative displacement and strain experienced in structural components, including reinforcing bars (rebars) embedded into concrete. The displacement can either occur due to a sudden overload such as an earthquake, or can slowly develop over time, in the form of a contraction or an elongation. Therefore, being able to measure strain from time to time, or monitoring it continuously provides valuable information regarding the state of the damage induced. Strain (or engineering strain) is defined as the ratio of the relative displacement occurring between two points to the original distance between those two points as shown below:

$$e = \frac{\Delta L}{L} \quad (1.1)$$

where e is the strain, L is the original length, and ΔL is the change in L . Young's modulus, or elastic modulus, is an intrinsic mechanical property of elastic solid materials and is given as:

$$E \text{ (Pa or N/m}^2\text{)} = \frac{\sigma \text{ (Pa or N/m}^2\text{)}}{e} \quad (1.2)$$

where E is the Young's modulus and σ is the tensile stress. The tensile stress forming on the structural component is also related to the strain by Young's

modulus, an intrinsic mechanical property as follows:

$$\sigma \text{ (Pa or N/m}^2\text{)} = \frac{F \text{ (N)}}{A \text{ (m}^2\text{)}} \quad (1.3)$$

where F is the exerted force and A is the cross-sectional area through which the force is applied. It should be noted that these formulas are only valid in the case of small displacement/deformation levels and they hold only in the elastic deformation region of steel.

In literature, especially in recent years, there is an increasing interest on the technologies developed for the measurement of strain and displacement. However, many of these technologies are wired and/or active, meaning they incorporate a sensor which requires the use of electrical energy for operation (for transmitters). Furthermore, the practical challenges arising from the fact that majority of the commonly used devices in SHM (such as strain gages) are wired, are highly undesired, since a large bulk of cables that is sticking out of the monitored beams/columns constitutes a problem. Therefore, a wireless exchange of data is preferred between the receiver and the sensing part that generally remains embedded inside the concrete.

Among the techniques proposed for measuring strain in literature, one of the most studied are the RFID-based methods [1–6]. Especially, passive RFID is an emerging technology where a passive tag transfers the information about the sensed quantity (e.g., temperature, humidity or density of chemical compounds, as well as strain or relative displacement) via an impedance change to the transmitter, which in turn sends the digitalized signal wirelessly to the receiver. The signal collected by the receiver is further processed to obtain the change of the sensed quantity in terms of radar cross section or turn-on power of the RFID chip. A completely passive system is possible by converting the interrogating RF signal to direct current so that it is used to feed the transmitter, making the passive-RFID quite appealing. Nevertheless, RFID-based displacement sensors can only offer a resolution on the order of millimeters [2, 3]. This constitutes a major problem when it is considered that generally micrometer-scale changes are in question in SHM applications. In [5], a resolution as low as 20 microstrains was shown by an RFID-based strain sensor, but the measurements were made in

free-space in laboratory environment.

Another frequently used strain sensing technology is the surface acoustic wave (SAW) [7–10]. SAW-based sensors monitor strain by detecting the change of the acoustic wave velocity due to deformation. However, excess amount of losses and the difficulty of creating a coupling between the acoustic waves and the sensed quantity are serious drawbacks of such systems [11, 12]. Studies have been done in the literature where antennas are utilized as sensors for detecting the sensed quantity based on the changes in the radiation pattern of the antenna stemming from a deformation [5, 13–16]. Other wireless and passive strain sensors include magnetostrictive sensors which can change their shapes with changing magnetic fields [17, 18]; microfluidic sensors in which the flow of a liquid in a very thin channel is monitored ultrasonically [19, 20]; smart skin sensors [21]; flexible LC circuit-based designs [14, 22, 23]; and RF cavity transducers where the cavity resonance frequency is a function of strain [24]. On the other hand, none of these methods has been able to find a widespread area of use due to several reasons including difficulty of application, complexity of design and/or limited sensitivity and resolution. In SHM, there have also been efforts to exploit several of these methods for wireless and passive measurement of damage indices such as displacement, strain, corrosion, humidity, as well as the presence and propagation of cracks [1–5, 13, 14, 24–35]. The works that incorporate passive wireless sensors for the purpose of SHM were summarized by a paper by Deivasigamani et al. [36].

Works have also been shown in the literature for detection of surface strain on industrial materials [37–45]. Fiber optic sensors are the most widely used type of technology, especially for detection of surface strain on composite materials. Among them, fiber-Bragg gratings and long-period fiber gratings are the most preferred sensors. These structures are based on the principle of detecting a change in the reflection and refraction characteristics of light in a fiber cable from the elongation/contraction due to the strain induced on the material. They hold significant advantages such as being compact, low-loss and resilient to electrical effects (such as a lightning) due to them being insulators; as well as being easily integrated into composites [46]. However, they also have major drawbacks such

as being very sensitive to heat, and having high costs and limited number of producers [46]. It was also shown that fiber optic sensors reduce the static strength and failure strength of materials, as well as the threshold for crack initiation due to their large diameter, which is 5-10 times the diameter of the reinforcement fibers which causes them to act as a notch in the composite material [47, 48].

Other methods were also proposed in the literature for measurement of the surface strain of materials. One of them is the self-sensing based method, which aims to use the material itself as a sensor rather than employing an external device for sensing [38, 41, 49–52]. For instance, this method was utilized for fiber-reinforced laminate structures in sensors developed by Todoroki et al. in [49, 50], which makes use of the conductivity in specific directions due to the presence of the carbon fiber in the normally insulating material of laminate. The change of electrical or electromagnetic properties, such as resistance or radiation characteristics, can then be investigated for sensing the strain. While they can be used for demonstration of a change in the mechanical properties of the material, the most important drawback in these kinds of sensors is the inability to characterize the deformation in terms of the location and strength. Another very important disadvantage is that the strain can only be sensed only after it produces a deformation in the material.

Wireless sensor networks (WSNs) are also widely used for modern SHM of buildings, bridges, airplane wings, and aircraft and turbine blades. These networks are composed of many active sensors located on critical points, each of which determines the deformation on the point on which it is located, and sends the data wirelessly to a transmitter for processing. In literature, a large number of studies was shown based on WSN's [43, 44, 53–57]. However, many issues remain unsolved regarding the WSNs, which can be summarized in a few groups as follows [58]: 1) The acquisition of data: In WSNs, issues such as bandwidth, system memory and power are very important considerations, and data to be collected and transmitted have to be selected very carefully. 2) Local processing of data: The data have to be pre-processed before being sent to the transmitters, which increases the complexity of the sensor. 3) Synchronization of the sensors: In SHM, change of the deformation indices such as strain versus time have to

be detected accurately. A synchronization problem among the sensors makes the tracking of the monitored parameter very difficult [38, 59].

In recent years, metamaterial-inspired structures, most commonly, several variants of split-ring resonators (SRRs) have also been employed for the purpose of sensing, utilized as biosensors [60], thin-film sensors [61], and strain and displacement sensors [30, 62–68]. Our research group has actively studied and pioneered the use of SRR structures for wireless strain measurement in various biomedical applications including the evaluation of bone fracture healing and the development of smart bioimplants [62–66]. A review by Chen et al. describes in detail the employment of metamaterial-inspired structures in sensing applications [69].

More recently, a novel SRR geometry was proposed by our group [62]. This structure, called as the nested split ring resonator (NSRR), was shown to be highly convenient for sensitive strain measurements with its high field localization. In this dissertation, we explore the capabilities of a wireless and passive sensing system based on a sensor probe designed in this geometry, as well as a transceiver antenna. The displacement sensing ability of such a system was first shown in [70] in an MS thesis prepared in Electrical and Electronics Engineering Department of Bilkent University. In this work, it was demonstrated that the presence of the NSRR probe created a local peak (at its own resonance frequency) in the reflection coefficient spectrum of the monitoring antenna, and this peak was subject to a shift by a mechanical change in the sensing probe. Here, in this study, we understand the characteristics and limits of this sensing, which is enhanced by a single-slot microstrip antenna and the NSRR geometry modified to measure the displacement in Chapter 2. Then, in Chapter 3, we show the results of a set of tensile test experiments performed on the sensing system, where the modified NSRR probe is attached on a rebar which is loaded with a vertical force that results in the elongation or contraction of the rebar. By its high sensitivity and resolution, the sensing system is shown to be suitable for being employed as a wireless and passive technique for detecting displacement and average strain in SHM. In addition, it can also be utilized as an accurate and quantitative method of understanding post-earthquake damage due to its high dynamic range and robustness. The results of these characterization experiments, first on a

translation stage where controlled displacement is created, and then via the tensile loading setup, were published in *Sensors* [71, 72].

In Chapter 4, we explore in detail the effects of the complex electromagnetic medium due to the combination of the concrete and the rebar grid present within the reinforced concrete in structures, on sensing. These effects, which previously were not covered adequately in literature, are inevitable for the wireless sensing techniques designed to operate in SHM applications. Thus, it is important to understand how the sensing characteristics are affected by each and every scenario of the complex media that is present in a real-life case. We present a numerical fit on the displacement-resonance frequency curve, which in essence is the basis of the transformation from the measured frequency shift to the displacement and strain. The exactness of this curve is vital for an accurate calibration; in other words, for evolution of the sensing into measurement. The effects of each complex medium scenario on the fit parameters are also discussed in Chapter 4. In addition, a solution is brought to the most disrupting scenario of placement of the NSRR probe directly on the reinforced concrete. The results of this study were also published, in *IEEE Sensors Journal* [73].

In Chapter 5, the results of the simply supported beam experiments are presented. Like the tensile tests, the simply supported beam experiments are also carried out in Structural Engineering Laboratory of Civil Engineering Department in Middle East Technical University. In these experiments, the NSRR probes are attached on several rebars of a grid inside a reinforced concrete member, which is a standard structural beam in our case. Then, the beam undergoes bending under a vertical force, where the transverse loading causes compressive strains at the top and tensile strains on the rebars at the bottom. The operation of the sensing system in simply supported beam experiments is very important since this forms the final step for the real-life testing of a sensor, where the probes stay completely embedded within the beam and the antenna monitors them from outside. The practical challenges encountered and the solutions are discussed in Chapter 5. The results of the simply supported beam experiment were covered in detail in an article published in *Sensors* [74].

An important application of the sensing system is to employ multiple probes on critical parts of the structure and perform measurements simultaneously via these probes. In literature, wired SRR ring-based sensors that possess a 2-D sensing capability via a single passive structure (which in essence is generally an array of such structures) were shown: In [75], Withayachumnankul et al. utilized the coupling of different SRR structures to a microstrip transmission line for thin-film sensing. Each structure created a resonance at a specific frequency and a shift observed in each dip provided information related to the dielectric properties as well as the location of the sample, increasing the throughput. In [76], a similar approach was used by Puentes et al. for resolving the relative changes in 2-D dielectric properties of organic tissues by a 12-element SRR array. In [33], Horestani et al. demonstrated an alignment and displacement sensor based on two movable broadside coupled SRRs oriented at 90° angle with respect to each other to detect changes in x and y directions. Although these sensors provide better comprehension and characterization of the planar distribution of their respective sensed quantities, they are all arranged in a wired configuration and the samples have to be placed directly in contact with the sensors. This constitutes a major problem preventing their use in important applications, e.g., in harsh environmental conditions, remote sensing platforms, and in structural health monitoring (SHM) when the sensors have to be embedded inside the concrete. A passive wireless sensor was shown by Xu and Huang for detection of the location and propagation of cracks in a material, on which microstrip patch antennas of different resonant frequencies were located [77]. When a crack is observed at a point where the antenna is placed, the antenna radiation characteristics become subject to a change and this can be observed by sending and recovering the backscattered signal by an interrogator antenna. By this technique, combined with spatial division, where two antennas with the same resonant frequency are switched ON and OFF, specific responses from four different antenna-sensors can be obtained. This frequency division technique can be improved to a wireless passive 2-D sensing mechanism by employing multiple sensors with a predefined resonant frequency and bandwidth, where the responses from every sensors can be captured in a single frequency sweep. In Chapter 6, we show that multi-point sensing is possible by our sensing system, where a single antenna can be used for communicating

with more than one NSRR probe, and responses of many probes can be acquired and observed in the antenna reflection coefficient spectrum separately and simultaneously, without giving away from the superior sensing characteristics of the system.

Finally, in Chapter 7, we propose an equivalent circuit model of the nested split ring resonator probe, which forms the basis of sensing in this study. Although originally designed for biosensing by Melik et al. [62], the NSRRs have since been exploited in many applications as part of an antenna [22, 78, 79], a compact low-phase noise oscillator [80], a compact NSRR-based filter [81], and a thin-film sensor [82] besides this study. In literature, equivalent circuit models of different types of two or three dimensional SRRs (classical, cross embedded, U-shaped, etc.) have extensively been studied and models based on different distributed line or lumped circuits were shown [83–99]. On the other hand, despite having superiority over the conventional SRR geometry and being utilized in different application areas, an equivalent model which can explain the operation of the NSRR was not previously covered in literature. In Chapter 7, we show a circuit-based model of the NSRR geometry, and demonstrate that the model is valid, through comparison of the outputs of the model to full-wave simulations and measurements. This dissertation is concluded with Chapter 8, where the novelties and the advantages of this study are summarized and possible improvements and future work are discussed.

Chapter 2

Sensing System

2.1 Components of the Sensing System

2.1.1 NSRR probe

The sensing probes employed in this work are in nested split ring resonator (NSRR) geometry. This geometry is also referred to as the “comb-like” NSRR. The NSRR geometry was first proposed by Melik et al. in [62] for a more compact size and a better sensitivity compared to classical SRRs. In this structure, there exists a number of parallel strip pairs which are connected from one side but symmetrically separated from the other by a gap between every pair. Each strip forms a path with the uppermost strip that is split by this gap, therefore, the whole structure can be considered as a combination of nested split-rings. The smaller size of the NSRR becomes possible via an increase in the number of metal

Some paragraphs in this chapter are reprinted, with permission, from “Wireless Displacement Sensing Enabled by Metamaterial Probes for Remote Structural Health Monitoring,” by B. Ozbey, E. Unal, H. Ertugrul, O. Kurc, C. M. Puttlitz, V. B. Erturk, H. V. Demir, A. Altintas, *Sensors*, vol. 14, pp 1691-1704 (2014) and “Wireless Measurement of Elastic and Plastic Deformation by a Metamaterial-Based Sensor” by B. Ozbey, H. V. Demir, O. Kurc, V. B. Erturk, A. Altintas, *Sensors*, vol. 14, pp 19609-19621 (2014).

strips, which in turn increases the overall capacitance and inductance of the structure and lowers the resonance frequency. Also, by the increased number of gaps, a high-Q resonator characteristic is achieved, bringing in better sensitivity and resolution.

Previous work by our group employed NSRR structure for wireless strain measurement in biosensing applications in which the strain that formed on the structure propagated onto the sensor chip and could be monitored [62]. This required the sensor to stretch (or contract), thus the sensing was limited to the Young modulus of the sensor material. The substrate of the NSRR is made of mostly a dielectric and it sometimes comprises a ground plane (to capacitively load the meta-structure and further lower the operating frequency if needed), which means that it is not a relatively compliant material. The regular NSRR structure is shown on a steel reinforcing bar (in short, rebar) in the bottom of Figure 2.1.

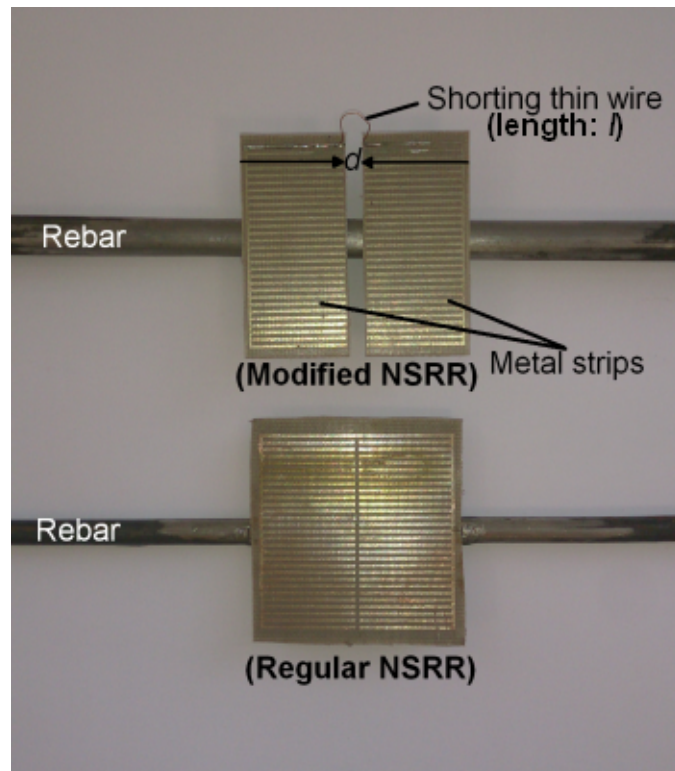


Figure 2.1: Top: Modified NSRR structure for displacement/strain measurement in structural health monitoring, Bottom: Regular NSRR structure.

For an application in SHM, the NSRR structure was modified as follows: The

NSRR was symmetrically split into two partitions with respect to the gap between the teeth. These two parts, free to move with respect to each other, were further short-circuited on one end by soldering a thin, loose enough jumper wire to the normally continuous outermost pair of strips (the structure on top in Figure 2.1). This way, when a displacement occurs between the two attachment points on the structure on which the NSRR is fixed, these two moving parts are separated from (or brought closer to) each other by the amount of the displacement that has formed. This translates into a capacitive change in the modified NSRR structure, which in turn shifts the spectrum of the coupled system response. The splitting of the sensor into two electrically shorted but freely-moving parts removes the limitation on the maximum measurable strain dictated by the Young modulus of the substrate material on which the metallic strips are etched (either Rogers Duroid or FR-4). This also transforms the strain sensor into mainly a displacement sensor. The edge-to-edge distance between the two NSRR parts is denoted as d , as shown in Figure 2.1. This sensing structure, which will be referred to as the NSRR probe, is fastened on the structure to be monitored, e.g. a rebar, via two points at each moving parts. These attachment points should have areas as small as possible in order to avoid the strain propagation through the hard epoxy onto the probe parts, which eliminates the probe detachment problem at high levels of strain. In addition to measuring displacement via correct calibration, this probe can also be utilized for measuring the average strain, since the ratio of the relative displacement to the distance between the attachment points gives the strain. It should also be noted that the maximum displacement/strain that can be measured is only limited by the wire length via the modified NSRR configuration, unlike the regular NSRR structure. Therefore, the maximum measurable strain is substantially increased. The length of the thin shorting wire is typically selected as a few centimeters since a very long wire increases the overall inductance and causes the system resonance frequency to drop out of the antenna bandwidth.

For the studies conducted in this dissertation, several modified NSRR designs with different resonance frequencies were developed. Here, special attention will be given to two designs that are shown in Figure 2.2. The first design, referred

to as Design A, resonates at around 400 MHz, while the second design, referred to as Design B, resonates at around 800 MHz. The resonance frequencies are mainly determined via the number of the strip pairs (N) as well as the widths and lengths of each strip. The design of the probes were made in commercial CAD software CST Microwave Studio[®], where the resonance frequency was determined by changing the physical dimensions. After the design, the NSRR probes are etched on a one-sided Rogers Duroid 4232 substrate with an ϵ_r of 3.2. The physical dimensions and the electrical properties of these two designs are given in Table 2.1. In order to monitor the displacement and/or strain forming along a rebar embedded in concrete, the operating frequency of the sensing system should be selected such that the electromagnetic waves can penetrate through the concrete wall without much attenuation as well as be reflected back from the NSRR probe without experiencing an absorption or transmission. The operating frequency is also important in determining the size of the NSRR probes which should be compatible with the diameter of the rebar. By considering these issues, the frequencies 400 and 800 MHz are selected for the sensing system. This is further discussed in detail in Chapter 4. The Styrofoam separators shown in Figure 2.2 are necessary for reducing the effects of the complex electromagnetic medium formed by the concrete and rebar grid, which is also explained in detail in Chapter 4.

Table 2.1: Properties of the two NSRR designs employed in this work

	N	f_{res}	Footprint size	ϵ_r	Substrate thickness
Design A	29	400 MHz	47 mm \times 47 mm	3.2	0.508 mm
Design B	50	800 MHz	25 mm \times 25 mm	3.2	0.508 mm

2.1.2 Antenna

The antenna used in the sensing system is a single-slot microstrip antenna based on the design proposed by Latif et al. in [100]. It is modified here to operate around 440 MHz with a sufficiently high bandwidth of 8% where $|S_{11}| < -8$ dB to be used along with NSRR Design A. This antenna type is selected mainly because it allows for a much reduced size with respect to the wavelength (the

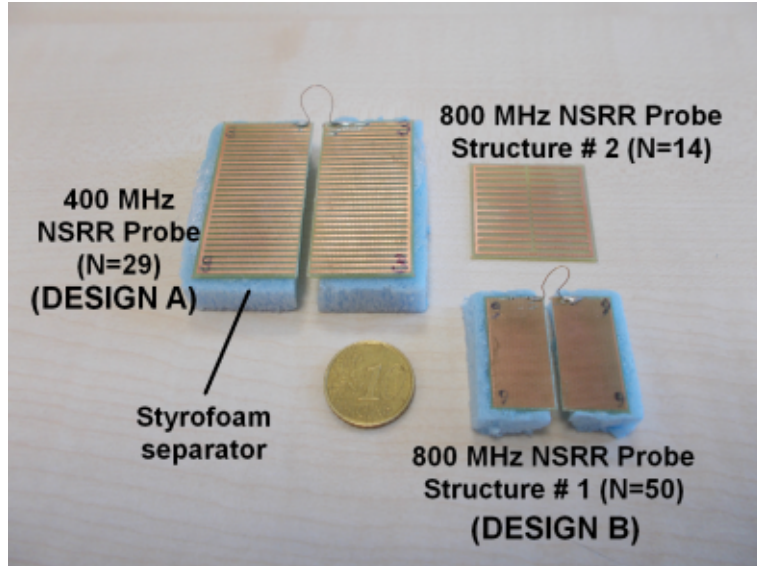


Figure 2.2: Modified NSRR structure designs with different resonance frequencies.

maximum antenna size is 18 cm at a wavelength of 75 cm) along with an increased bandwidth. The slot antenna comprises a 50Ω microstrip feedline at one side of the dielectric substrate and a ground plane with a monopole slot at the other side. The antenna is excited through this feedline at the backside of the substrate, resulting in a horizontally-polarized E-field being transmitted from the slot at the other side of the substrate. When the antenna is brought in a position which is face-to-face with the NSRR, and illuminates the NSRR whose metal strips and gaps are also horizontally directed; a strong coupling is formed between the two structures. The photograph and the reflection characteristics (S_{11}) of the microstrip single-slot antenna for both measurements and simulations in CST Microwave Studio are given in Figure 2.3 and Figure 2.4, respectively.

2.2 Operation Principles of the Sensing System

The underlying concept behind the sensing system is the electromagnetic coupling formed between the NSRR probe and the antenna. Any kind of change occurring on the NSRR probe is directly reflected to the antenna and can be observed in its reflection coefficient through this electromagnetic coupling. That is to say,

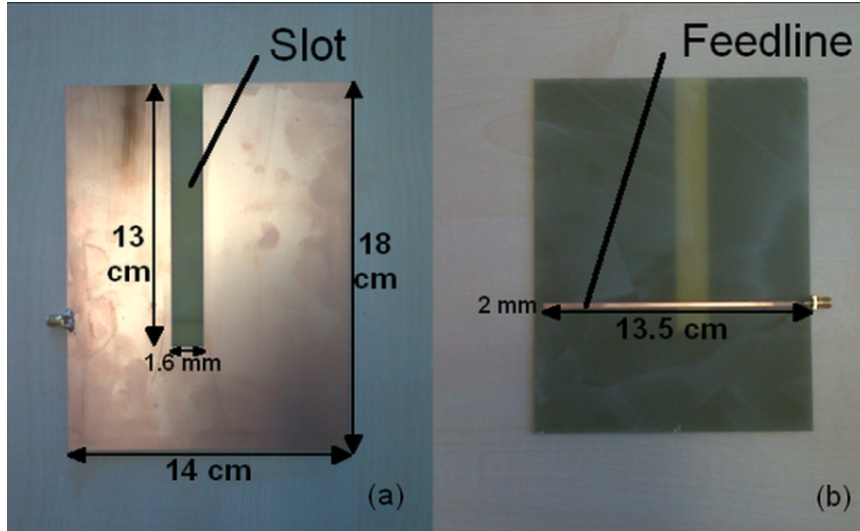


Figure 2.3: The photograph of the fabricated microstrip single-slot antenna: a) Front side with the slot, b) Backside with the feedline.

the NSRR probe manifests itself as a local peak at its own resonance frequency on the reflection coefficient spectrum of the antenna. By monitoring this peak (frequency of the maximum point of this peak, or zero crossing of the phase, etc.), it is possible to understand the mechanical changes occurring on the NSRR probe, more specifically, the change of strain or displacement between the two attachment points for this particular case. This forms the basis of the sensing made possible via two system elements and a network analyzer.

In the sensing system, the antenna acts as a transceiver (transmitting the waves it is fed with from the network analyzer to the NSRR probe and collecting the backscattered signal) for the NSRR probe which is placed within the near-field of the antenna. As mentioned before, the strong coupling is due to the way the NSRR probe is excited: The horizontally polarized illumination from the slot antenna creates a well-coupled system with the NSRR probe, where the splits and gaps are also horizontal. In the case of cross-polarization, e.g., when the antenna is rotated 90° around the z -axis, coupling is not observed. A strong electromagnetic coupling yields a higher sensitivity and resolution of the observed quantity when compared to other types of wireless sensors shown in the literature.

In order to predict the coupling behavior and to develop a better insight for

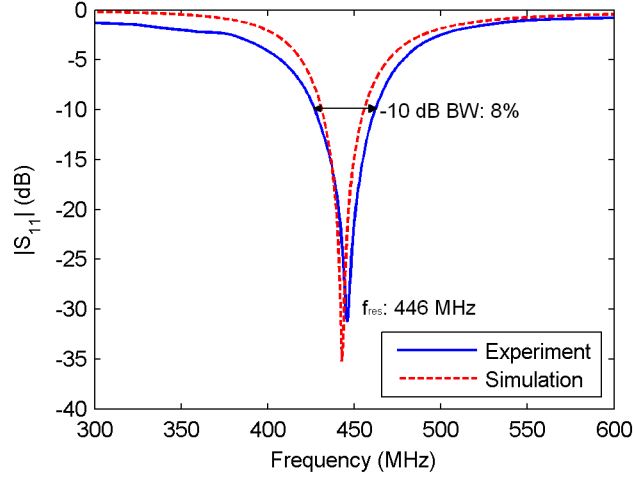


Figure 2.4: The measured and simulated reflection coefficient versus frequency for the microstrip single-slot antenna.

its operation, numerical studies were carried out using the transient solver of CST. These simulations were used to compare the localization of fields on the NSRR when the NSRR is excited within the near field of the antenna for four different scenarios. In these scenarios, the monitoring distance (D_m , which is the separating distance between the antenna and the NSRR) is kept at 5 cm for all cases. The cross-sections of the electric field intensities for these four cases are shown in Figure 2.5 and Figure 2.6. In the first scenario (see Figure 2.5)-a, the gap between the two sides of the NSRR probe is 1 mm, and the simulation frequency is 406 MHz, which is the resonance frequency corresponding to the 1 mm displacement in the simulations. As can be observed from the figure, a high localization of fields is achieved on the NSRR for this resonance case. The NSRR creates a localized field (significantly dominant at $z = 45$ mm) which reflects back to the antenna on which we observe the coupled system response. On the other hand, in the scenario presented in Figure 2.5-b, we still have a 1 mm gap between the two parts of the NSRR, but the simulation frequency is 448 MHz, which is the resonance case for a 5 mm gap. Here, we can observe that the localization on the NSRR is much poorer and the field that is reflected back to the antenna is much less although this frequency also stays within the bandwidth of the antenna. This is also the case that is demonstrated in Figure 2.6-a and Figure 2.6-b, where the gap between the two NSRR parts is 5 mm and the simulation frequencies are

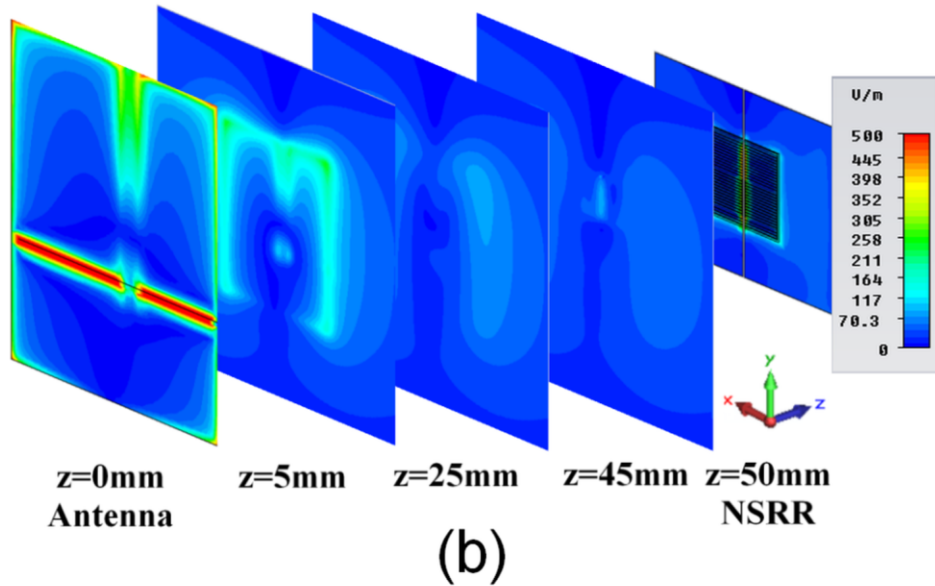
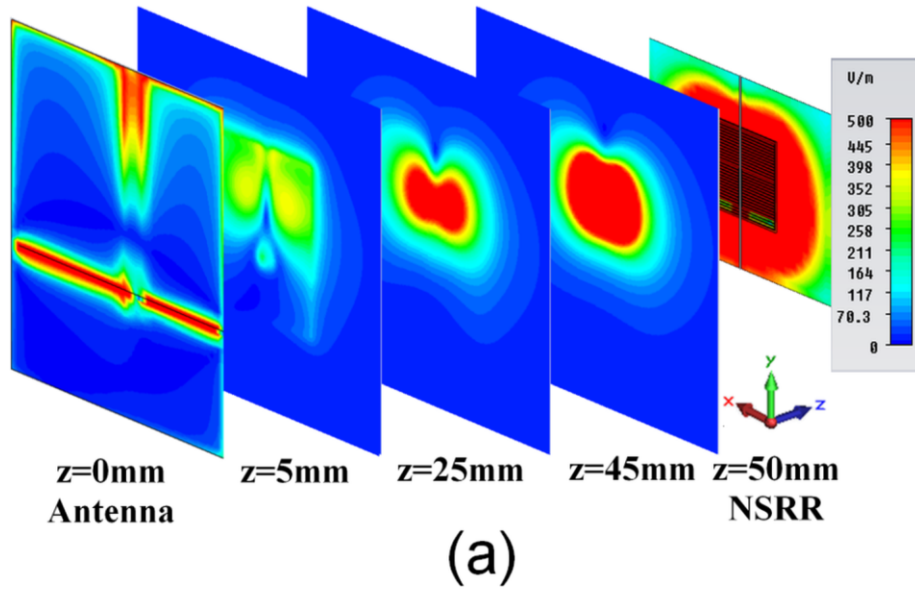


Figure 2.5: a) Electric field map numerically calculated on the antenna, on the 1-mm-separated NSRR probe, and at several cross-sections between the antenna and the probe when the simulation frequency is the resonance frequency of $d = 1$ mm (406 MHz), and b) when $d = 1$ mm again but the simulation frequency is 448 MHz (off-resonance case for $d = 1$ mm). (Reprinted, with permission, from “Wireless Displacement Sensing Enabled by Metamaterial Probes for Remote Structural Health Monitoring,” by B. Ozbey, E. Unal, H. Ertugrul, O. Kurc, C. M. Puttlitz, V. B. Erturk, H. V. Demir and A. Altintas, *Sensors*, under the Creative Commons Attribution License (<http://creativecommons.org/licenses/by/4.0/>).)

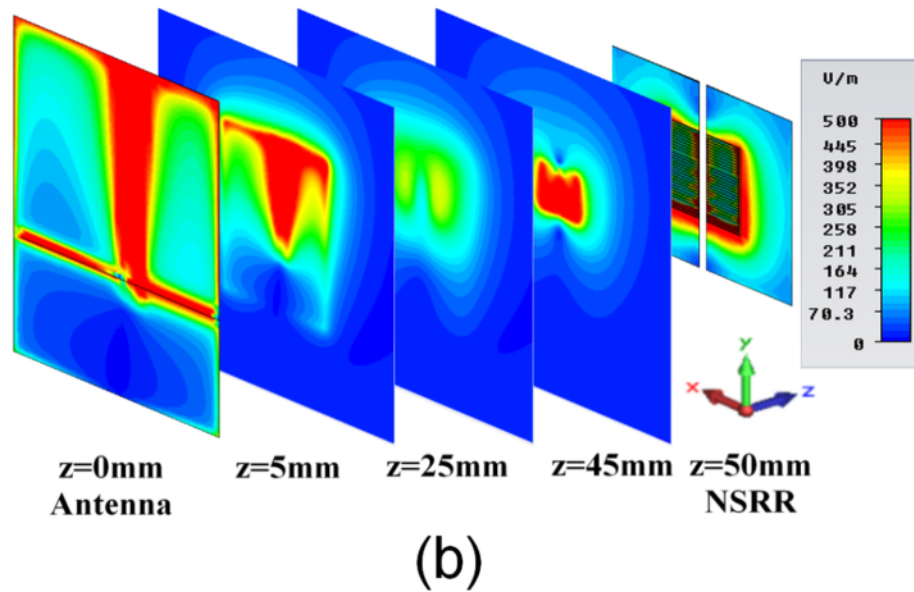
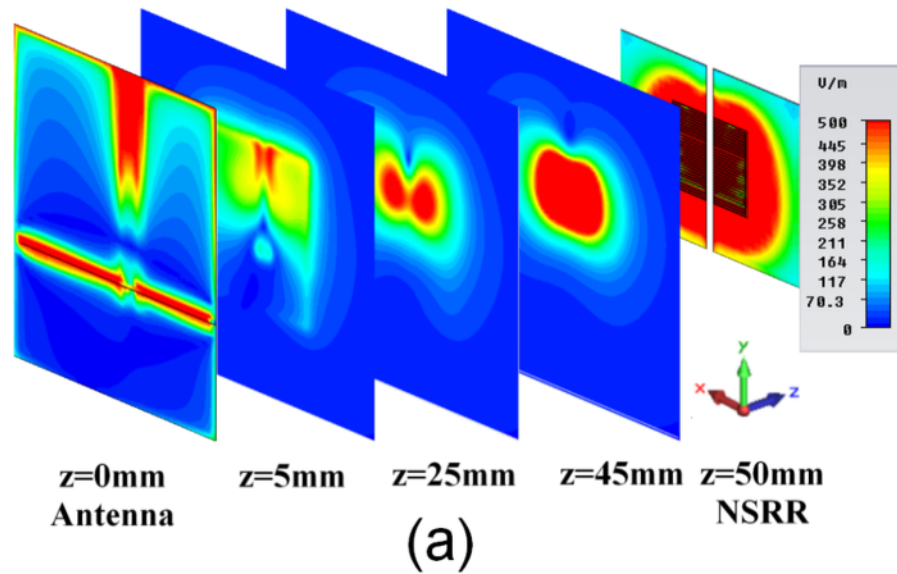


Figure 2.6: a) Electric field map on the antenna, on the 5-mm-separated NSRR probe and at several cross-sections between the antenna and the probe when the simulation frequency is the resonance frequency of $d = 5$ mm (448 MHz), and b) when $d = 5$ mm again but the simulation frequency is 406 MHz (off-resonance case for $d = 5$ mm). (Reprinted, with permission, from “Wireless Displacement Sensing Enabled by Metamaterial Probes for Remote Structural Health Monitoring,” by B. Ozbey, E. Unal, H. Ertugrul, O. Kurc, C. M. Puttlitz, V. B. Erturk, H. V. Demir and A. Altintas, *Sensors*, under the Creative Commons Attribution License (<http://creativecommons.org/licenses/by/4.0/>).)

448 and 406 MHz, respectively, which represent the resonance and off-resonance cases for the system at 5 mm displacement level. In Figure 2.6-a and 2.6-b, there is again a significant difference between the resonance and off-resonance cases in terms of localization. The magnitudes of the electric fields shown in these figures depend on the excitation and do not reflect the real values; however, the true value of this comparison is that it demonstrates that a significantly high localization is obtained regardless of the displacement level when the NSRR is illuminated in the resonance of the coupled system corresponding to the current gap between the NSRR parts.

2.3 Characterization of the Sensing System with Experiments

The electromagnetic behavior of the sensing system should be thoroughly characterized before it is employed in a real-life application. In order to understand the characteristics of the system, several different types of experiments were conducted. These experiments are covered in the subsequent sections.

2.3.1 Frequency shift with d

In the first of the characterization experiments, the edge-to-edge distance between the two mechanically separated parts of the modified NSRR probe, d , is made subject to a change in a controlled fashion. This is possible via a PC-controlled xyz translation stage, which can be made to move in three different directions with a minimum step size of 5 μm (see Figure 2.7). In this experiment, d is changed from 0 to 6 mm with a step size of 2 mm, and the results are presented in Figure 2.8. The case where NSRR probe is not placed in front of the antenna (no-coupling case) is also given in the figure. It is observed that the presence of the NSRR probe can clearly be understood by a local peak (or dip) in the antenna reflection coefficient and the frequency of this peak (or dip) shifts as d is

varied. As d is increased, two parts of the NSRR probe are moved far away from each other, leading to a decrease in the overall capacitance, which results in an increased resonance frequency since $f_{res} = 1/\sqrt{L_{nsrr}C_{nsrr}}$. Vice versa, a decrease in d leads to a decreased resonance frequency. This is visible in Figure 2.8. For this experiment, the monitoring distance D_m , that is, the distance between the antenna and the NSRR probe, is 10 cm. For all the experiments in this section, the length of the shorting wire, l , is 4 cm.

Throughout this dissertation, the term “resonance” is used for the tracked local peak frequency observed from the antenna reflection spectrum. The reason for this can be described as follows: The behavior of the NSRR probe when it is decoupled from the antenna can be identified by exciting it with a plane wave and inspecting the reflection coefficient. In such an experiment, the resonance is in the form of a dip in the reflection plot (much of the energy sent to the probe is stored in the probe, and does not return back). However, in the coupled case, the NSRR probe stays within the near-field of the antenna, and the valley behavior is not observed. Instead, a peak that shifts is observed in the antenna reflection coefficient spectrum as the displacement d is varied. This shift corresponds to a shift of the valley observed in the waveguide experiment (when only the NSRR response is present) when the displacement between the NSRR probe parts is changed. Since both shifts are characterized to yield the same behavior in the coupled and the decoupled cases, the peak is defined as resonance.

The full translation stage experiment setup, including the NSRR probe, the single-slot antenna and the cardboard on which the NSRR probe is fixed (see Figure 2.7) is also simulated in CST Microwave Studio. These simulations provide a means of verification of the experiment results as well as the only source of information in case no controlled experiment is possible (e.g. when the NSRR probe is placed inside a concrete beam). The reason why cardboard is included in the experiments is the following: It has been observed that the frequency shift regime is open to the effects of the surrounding medium, especially the dielectric material which touches the NSRR probe and acts as an additional capacitance. Therefore, the overall effect of this cardboard is to decrease the resonance frequency of the structure. The simulation setup and the shifting of

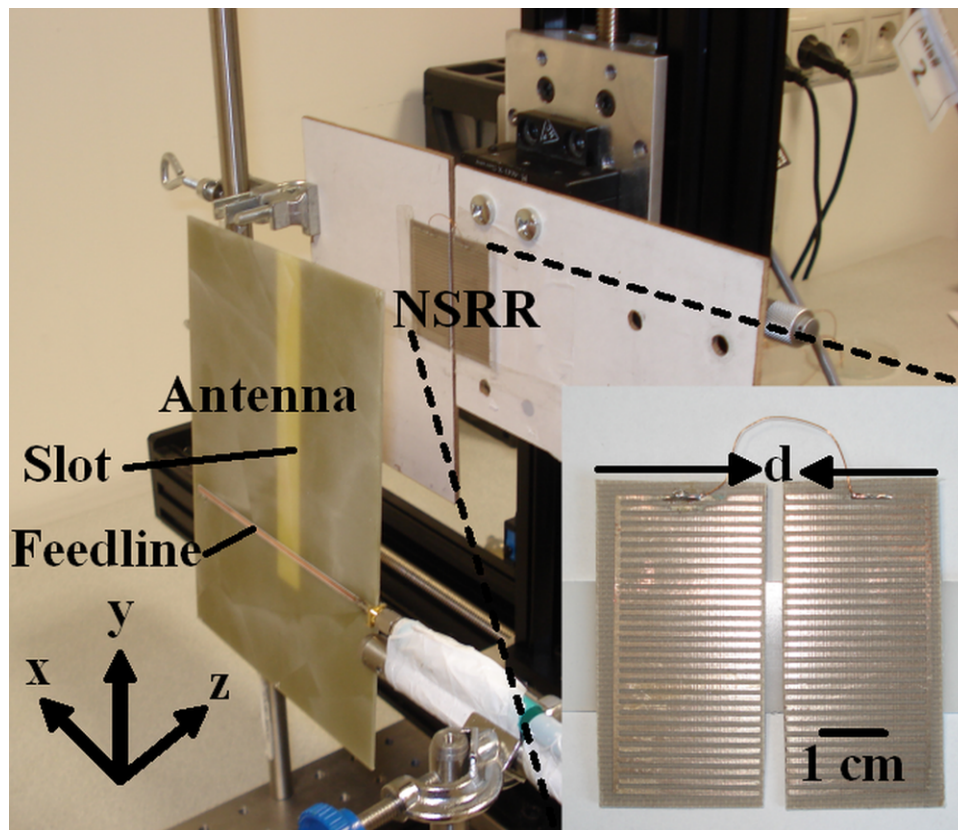


Figure 2.7: The displacement experiment setup including the sensing system elements and the xyz translation stage. (Reprinted, with permission, from “Wireless Displacement Sensing Enabled by Metamaterial Probes for Remote Structural Health Monitoring,” by B. Ozbey, E. Unal, H. Ertugrul, O. Kurc, C. M. Puttlitz, V. B. Erturk, H. V. Demir and A. Altintas, *Sensors*, under the Creative Commons Attribution License (<http://creativecommons.org/licenses/by/4.0/>).)

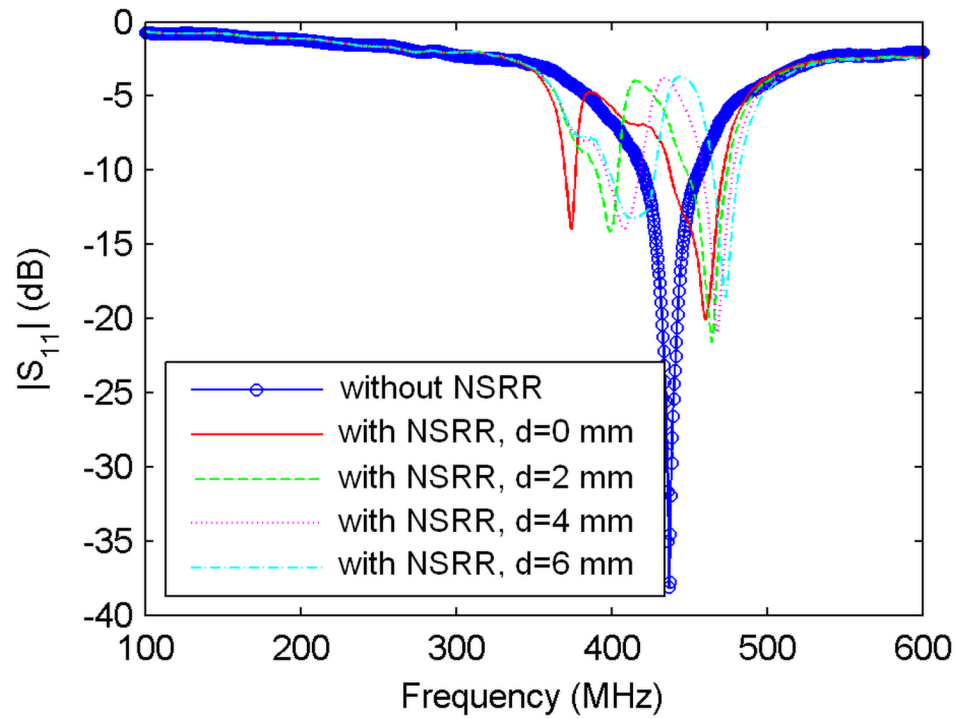


Figure 2.8: The change of antenna reflection coefficient via a change in d . The case where NSRR probe is not present represents only the antenna response. (Reprinted, with permission, from “Wireless Measurement of Elastic and Plastic Deformation by a Metamaterial-Based Sensor” by B. Ozbey, H. V. Demir, O. Kurc, V. B. Erturk and A. Altintas, *Sensors*, under the Creative Commons Attribution License (<http://creativecommons.org/licenses/by/4.0/>).)

the peaks are shown in Figure 2.9. In the simulations, d is varied from 0 to 10 mm.

The frequency shift obtained in a displacement setup is displayed in Figure 2.10. The shifting peaks are shown in Figure 2.10-a, whereas the change of the resonance frequency with d is shown in Figure 2.10-b. The experiment result is also compared the full system simulation result. The exact point of the resonance is determined by the frequency of the maximum point of the local peak corresponding to the NSRR probe. It is observed that the change of the NSRR probe resonance frequency with d takes a nonlinear fashion when the range of d is 9 mm, which is quite wide. In SHM, the strain levels which occur on steel rebars with time are in microstrain range, which correspond to a few tens of μm 's. Therefore, a detectable range of a few mm's is more than enough for the purpose of SHM. On the other hand, another important application area for the sensing system is the detection of displacement/strain after a sudden overloading impact such as an earthquake. Therefore, the displacement levels required in post-earthquake damage assessment are higher than those required in SHM, but they also typically do not exceed 1 mm. The sensing system is observed as being able to monitor these levels from the experiment results. For a narrower range of d , however, the linearity is observed to be much higher. A more linear range of $d = 3$ to 8 mm is shown in the inset of Figure 2.10-b.

Understanding of the frequency shift with d is one of the vital steps in the characterization of the sensing system. Since the proposed application area of the sensing system is in SHM, where the NSRR probe is attached on top of a rebar completely embedded in concrete, there is no way to reach to the probe after its installation. Therefore, it is of utmost importance that the frequency shift regime is well characterized before the installation in order to ensure that the measured frequency change can correctly be converted into displacement and/or strain information in SHM. An important feature of the frequency shift characteristics of the sensor is that it is 1-to-1, which means that a specific resonance frequency corresponds to only one d value and vice versa. Furthermore, the curve shown in Figure 2.10-b does not show any hysteresis, and the same resonance frequency for a specific d is obtained after it is increased or decreased and brought

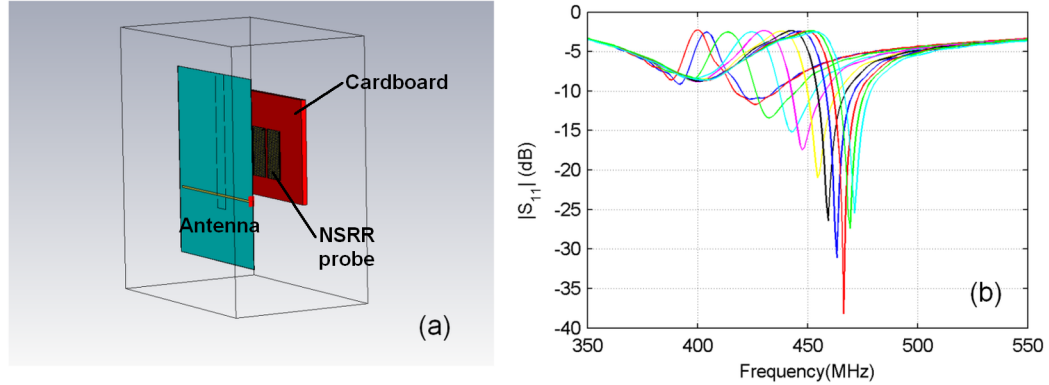


Figure 2.9: The full system simulation mimicking the displacement experiments. a) The simulation setup, b) The simulation results showing the shift of frequency peaks in antenna reflection coefficient as d is varied from 0 to 10 mm.

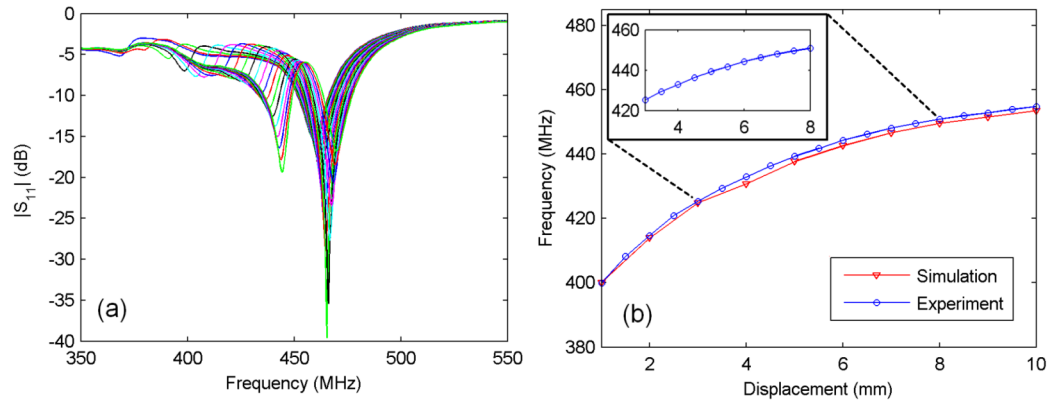


Figure 2.10: The displacement experiment results where d is varied from 1 to 10 mm: a) The shift of frequency peaks, b) The change of the NSRR probe resonance frequency obtained from the experiment and simulation. A more linear portion of the curve (3 to 8 mm) is given as an inset on top left. (Reprinted, with permission, from “Wireless Displacement Sensing Enabled by Metamaterial Probes for Remote Structural Health Monitoring,” by B. Ozbey, E. Unal, H. Ertugrul, O. Kurc, C. M. Puttlitz, V. B. Erturk, H. V. Demir and A. Altintas, *Sensors*, under the Creative Commons Attribution License (<http://creativecommons.org/licenses/by/4.0/>).)

to the same value.

2.3.2 Resolution

The resolution of the sensor is defined as the minimum level of displacement that can be measured without any significant effect of noise. The results of the experiment performed to test the resolution of the sensing system are shown in Figure 2.11. In this experiment, d is changed from 2.8 mm to 2.82 mm in $0.5 \mu\text{m}$ steps by using a Newport DM-13 micrometer, which allows for a $0.5 \mu\text{m}$ minimum graduation level. Although the effect of the system noise can be observed on the resonance frequency, it is also clear that the sensing system can respond to the changes in μm (or a few μm 's) scale. As mentioned earlier, a resolution in the order of μm 's is especially critical in SHM, where very slight changes have to be tracked on the structural parts over time.

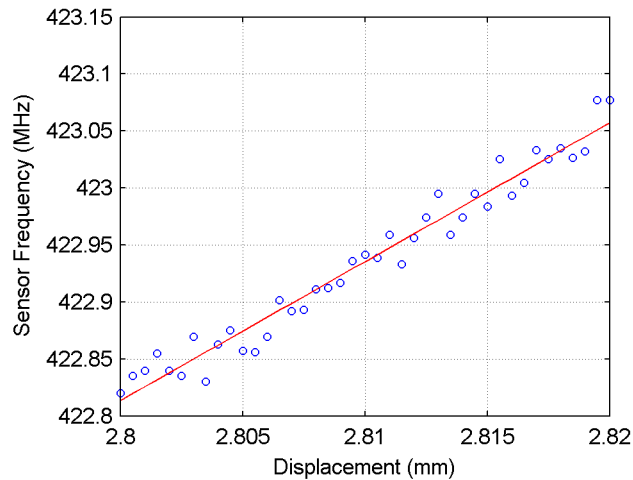


Figure 2.11: The displacement experiment results where d is changed from 2.8 mm to 2.82 mm in $0.5 \mu\text{m}$ steps.

2.3.3 Sensitivity

Sensitivity can be defined as the response of the sensing system to a change in d . Therefore, it is defined as the ratio of the change of resonance frequency to the

change in d , or, in other words, the slope of the displacement-frequency curve. It is observed in Figure 2.10-b that the system becomes less sensitive as d is increased and vice versa. However, a sensitivity over 10 MHz/mm is possible for selected regions in the d - f_{res} curve. This value corresponds to 10 kHz/ μ m, which is very high compared to the other sensors in literature. This value is also adequate for the SHM when it is considered that 10 kHz step size is well within the measurement range of the network analyzer. For various ranges of d , the levels of sensitivity are listed in Table 2.2.

2.3.4 Linearity

Linearity of the d - f_{res} curve can be evaluated by using a parameter called the coefficient of determination, also known as R^2 . The definition of R^2 is given in Appendix A. R^2 changes between 0 and 1, where a value close to 1 indicates a high linearity. For various ranges of d , the levels of linearity are listed in Table 2.2. Although the linearity degrades as the displacement range is increased, it is still above 0.95 for a range of over 7 mm. As observed in Table 2.2, another advantage of the sensor is that it can be utilized in several initial values of d without sacrificing its linear response. Thus, an initial separation can be allowed on the NSRR probe to create the frequency offset, and the sensor can be utilized in a higher-displacement region depending on the linearity and resolution of the region. As observed in Table 2.2, R^2 is equal to 0.99 for 3-8 mm. On the other hand, as pointed out before, saturation is observed at high displacement levels, implying that the rate of change of frequency with displacement decreases. This in turn leads to a lower sensitivity. Therefore, an optimum displacement range can be selected subject to the limitations set by the structure (e.g. rebar) geometry and the desired operation frequency of the sensor.

Table 2.2: Sensitivity and linearity levels observed for different ranges of d for the d - f_{res} curve given in Figure 2.10-b.

d_{min} - d_{max} (mm)	R^2	Sensitivity (MHz/mm)
1-3	0.988	12.70
1-6	0.970	8.86
1-8	0.955	6.61
2-7	0.984	6.69
3-7	0.995	5.68
3-8	0.990	5.12
4-8	0.991	4.48

2.3.5 Dynamic range and monitoring distance (D_m)

The dynamic range of the sensing system is defined as the maximum range of displacement that can be monitored. In Figure 2.10-b, a dynamic range of 9 mm is shown to be measured by the system. This value can easily be increased. In fact, a dynamic range of over 20 mm was observed in the experiment, although clearly at the expense of a reduced sensitivity and linearity. The dynamic range of 20 mm can be observed in Figure 2.12. No theoretical limit can be set on the dynamic range, but a practical limit is l , the length of the shorting wire.

The monitoring distance, or, the interrogation distance, is the distance between the antenna and the NSRR probe. Since the NSRR probe is located in the near-field of the antenna, it can very broadly be suggested that $D_{m,max} \approx \lambda = 75$ cm. Increasing the transmitter power is observed to have no effect on D_m since the network analyzer monitors the ratio of the received signal to the transmitted signal and this ratio is not related with power. The theoretical limit of λ is observed to be surpassed in the experiments, however, when the measurements are performed on a metal table which serves as a reflector of the scattered fields. On the other hand, this should be accepted as an extraordinary situation which is out of the scope of applications that the sensing system is developed for. A natural expectation is to increase D_m as far as possible. When a D_m in the order of several meters is achieved, one has the capability of recording measurements from outside of a damaged building so as not to risk human life. However, when the levels of sensitivity and resolution already attained via the present design

are also aimed to be preserved, this goal proves to be too ambitious. Therefore, the most reasonable application for the sensing system is to acquire data by placing the antenna just outside the structural component. This way, the goal of nondestructive testing is still attained while maintaining wireless and high-resolution sensing at the same time.

The dynamic range and D_m are closely related with the concept of tracking threshold and the illumination pattern of the antenna which determines the coupling strength. These are covered in the next section.

2.3.5.1 Tracking threshold

As previously mentioned, dynamic range is the maximum displacement range that can be captured by the antenna. This range can be deduced from the shift of the peaks that can be distinguished as a local maximum or minimum by a peak detection mechanism, e.g., a computer program. In order to determine the displacement tracking range, a threshold for tracking is desired. First, for the $|S_{11}|$ magnitude curve corresponding to the initial displacement level ($d = d_0$) which is the case where no external force is applied on the sample, a local maximum or minimum is selected at or around the resonance frequency and defined as $|S_{11}|_0$. Whenever a force is applied, a displacement $d > d_0$ or $d < d_0$ occurs leading to a new $|S_{11}|$ versus frequency curve. We record $|S_{11}|$ for each d (defined as $|S_{11}|_{\text{new}}$), and we monitor $|S_{11}|_{\text{new}} - |S_{11}|_0$. If, initially a local maximum point is chosen, the difference at this point will be in the form of a dip (if a local minimum is selected, it will be a peak). Then, tracking threshold corresponds to a preselected minimum difference in dB below which we do not consider the point as tracked (or sensed). The dynamic range is plotted for different monitoring distance levels in Figure 2.12 for a tracking threshold of 1 dB.

As seen in Figure 2.12, when the distance between the antenna and the NSRR probe is 7.5 cm, the whole displacement range of 20 mm can be tracked by the sensor at the specified tracking threshold. However, the dynamic range decreases as the antenna is moved away from the NSRR probe, and reduces to about 2

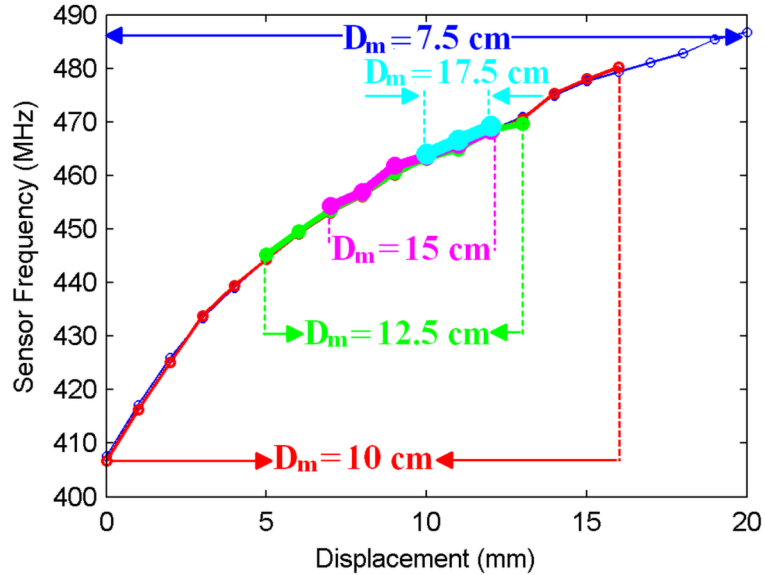


Figure 2.12: Dynamic range of the sensing system plotted for different monitoring distances D_m at a tracking threshold of 1 dB. (Reprinted, with permission, from “Wireless Displacement Sensing Enabled by Metamaterial Probes for Remote Structural Health Monitoring,” by B. Ozbey, E. Unal, H. Ertugrul, O. Kurc, C. M. Puttlitz, V. B. Erturk, H. V. Demir and A. Altintas, *Sensors*, under the Creative Commons Attribution License (<http://creativecommons.org/licenses/by/4.0/>).)

mm for a monitoring distance of 17.5 cm for the tracking threshold of 1 dB. This implies that the portion of the displacement range that can be measured is 2 mm for $D_m = 17.5$ cm, when the peak detection is only performed for a local peak of more than 1 dB resonance depth. As the tracking threshold is decreased, the tracking range naturally increases. However, reducing the tracking threshold too much complicates the detection, in case it becomes comparable with the system noise level.

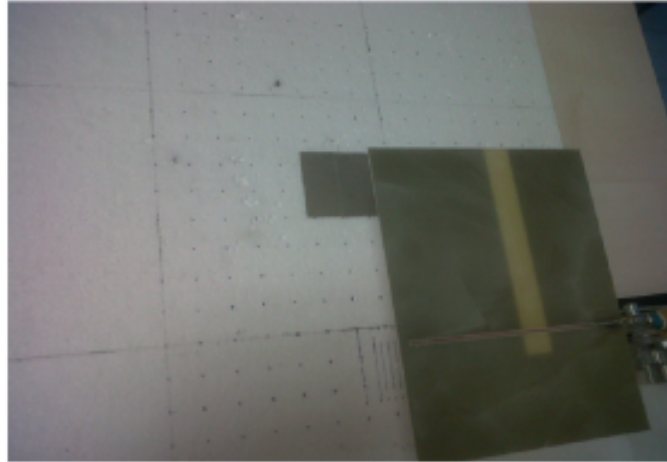
2.3.5.2 The coupling strength pattern

The dynamic range is closely related with the positions of the antenna and the NSRR probe with respect to each other. As shown in Figure 2.12, this range is shrunk as D_m is increased. Furthermore, it is also expected to decrease when the NSRR probe is relatively out of the “sight” of the antenna, or, the illumination

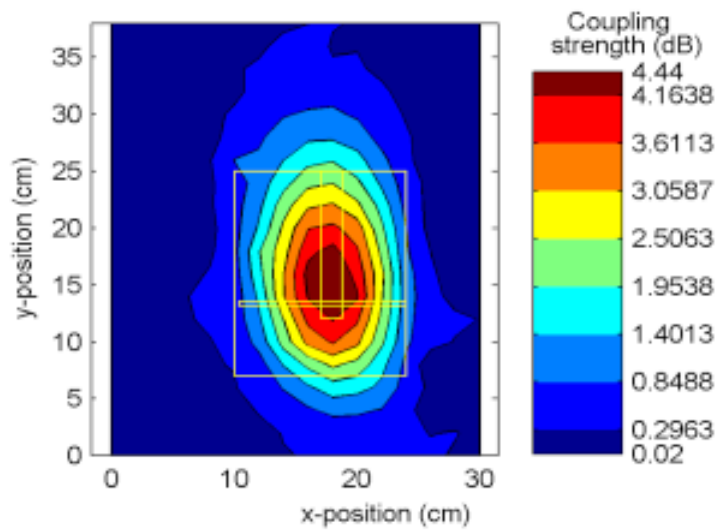
pattern of the antenna. In fact, the position of the NSRR probe with respect to the antenna determines the strength of the resonance observed from the antenna reflection coefficient. Therefore, the quality of the electromagnetic coupling between the antenna and the NSRR probe completely depends on their positions with respect to each other. In order to understand how the coupling takes place between the antenna and the NSRR probe, the following experiment is carried out: An NSRR probe is positioned in front of the antenna at 320 different points in an area which is 20 cm \times 38 cm wide (see Figure 2.13-a). At each point, $|S_{11}|$ is measured and the resonance depth is found after subtracting from each curve the $|S_{11}|$ for the case when there is no NSRR probe present. As previously mentioned, the resonance depth determines the quality of coupling, and also the dynamic range for the same value of tracking threshold. For the experiment, $D_m = 10$ cm, $d = 0$ mm, and $l = 4$ cm. The color map of the resonance depths obtained with this experiment is shown in Figure 2.13-b. The sketch showing the antenna position is also superimposed on the coupling strength pattern. As can be observed in the figure, the coupling is directly related with the illumination pattern of the antenna. The microstrip single-slot antenna is known to radiate from the slot introduced at the other side of the feedline. The strongest coupling is observed at the point where the feedline meets the slot (around the center of the antenna), diminishing gradually by forming elliptic contours due to the slot. This coupling strength pattern demonstrates the interaction between the sensing system elements in two dimensions, where the third dimension which is normal to this plane determines D_m . Although it is seen in Figure 2.12 that the sensing becomes difficult as D_m is increased above a certain level (dynamic range is shrunk to 2 mm after 17.5 cm), certain measures can be taken to extend the monitoring distance to a value comparable to the operation wavelength. This is discussed in the next section.

2.3.5.3 Subtraction of $|S_{11}|_0$ from $|S_{11}|_i$

It has been previously discussed that $|S_{11}|_0$, which is the $|S_{11}|$ curve obtained for $d = d_0$ (d_0 is the initial value of d , when no external force is applied) is subtracted



(a)



(b)

Figure 2.13: a) The points on which the NSRR probe is positioned for the coupling pattern experiment, b) Color map demonstrating the coupling strength between the NSRR probe and the antenna in a 2-D pattern. The antenna position is also shown on the plot ($D_m = 10$ cm).

from $|S_{11}|_i$, all $|S_{11}|$ curves corresponding to $d = d_i$, for the calculation of the resonance depth and comparison to the tracking threshold. This operation, in essence, serves as a filter for reducing the effect of the clutter, which acts as noise that increases as D_m is increased; and contaminates the backscattered sensing signal. In fact, the level of the effect of the clutter on the antenna always stays the same, however, since the reflection signal from the NSRR probe diminishes with increasing D_m , the signal-to-noise ratio is decreased, eventually leading the sensing signal to disappear. In other words, the tracking threshold cannot be decreased limitlessly (the minimum resonance depth in Figure 2.13-b is around 0.02 dB). Therefore, subtraction of the original $|S_{11}|$ curve from all other curves acts as a calibration which reduces the effect of the clutter, helping retrieve the seemingly lost sensing signal. This subtraction is made in dB, therefore it actually corresponds to a division in linear domain. Hence, this division gives the ratio of each obtained $|S_{11}|_i$ to the original $|S_{11}|_0$, which acts as a calibration curve. The $|S_{11}|$ curves obtained by an experiment where d is changed from 0 to 10 mm in 10 steps ($D_m = 30$ cm) is shown in Figure 2.14-a. $|S_{11}|_i$ from which $|S_{11}|_0$ is subtracted are shown in Figure 2.14-b. It can be understood that the subtraction of $|S_{11}|_0$ enables to diminish the effect of the clutter and makes the system sensitive to resonance depth levels as low as 0.1 dB.

For the subtraction methodology described above, there may be problems in tracking the frequency shift of the local peaks (or dips). In Figure 2.14-b, it is observed that a sharp transition from the negative to positive values exists at the frequency of the antenna resonance (around 437 MHz). In order to overcome this issue, another type of subtraction (or division in linear domain) is proposed. In this subtraction, the $|S_{11}|$ curve of the last measurement is subtracted from the current $|S_{11}|$. For example, for the experiment shown in Figure 2.14, the $|S_{11}|$ curve corresponding to $d = 0$ mm is subtracted from the $|S_{11}|$ curve corresponding to $d = 1$ mm; and $|S_{11}|$ curve corresponding to $d = 1$ mm is subtracted from the $|S_{11}|$ curve corresponding to $d = 2$ mm, and so on. Thus, the resulting curves, shown for an experiment where $D_m = 50$ cm in Figure 2.15, are produced from comparison of the present curve ($|S_{11}|_i$) to the lastly acquired curve ($|S_{11}|_{i-1}$). This type of subtraction is denoted as the consecutive subtraction. Either of the

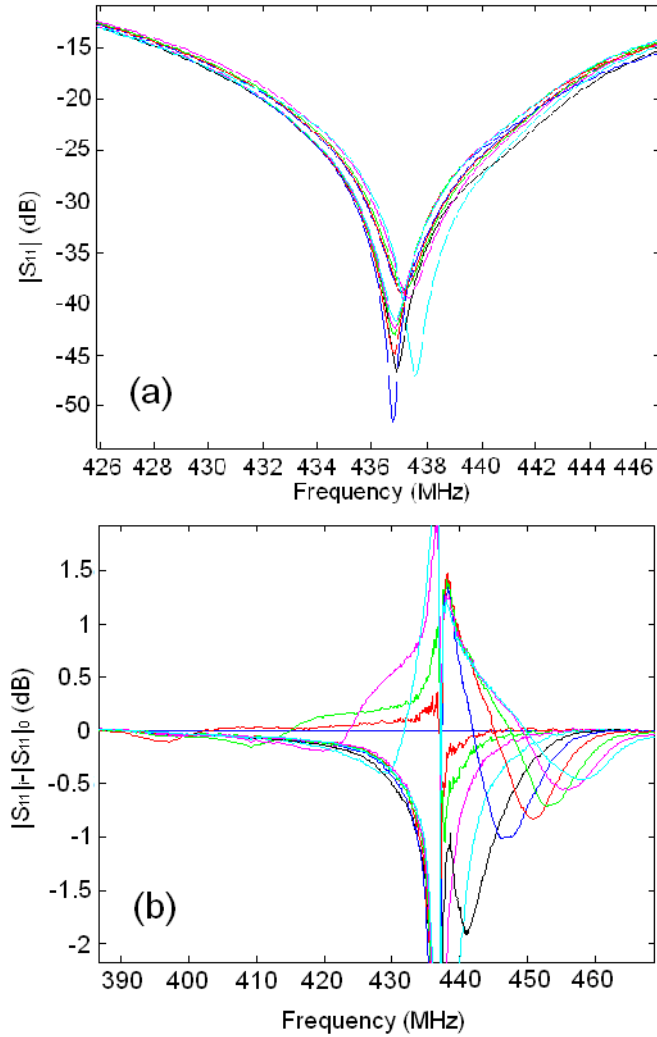


Figure 2.14: Experiment at $D_m = 30$ cm: a) $|S_{11}|$ curves obtained from an experiment where d is changed from 0 to 10 mm in 10 steps, b) $|S_{11}|$ curves from which $|S_{11}|_0$ is subtracted.

proposed subtraction (or division) methods can be employed for decreasing the effect of the clutter, which results in an increased D_m . As mentioned previously, at the operation frequency, $\lambda = 75$ cm. This is a theoretical limit which is difficult to attain via near-field coupling, but it can be approached by utilizing the proposed subtraction techniques.

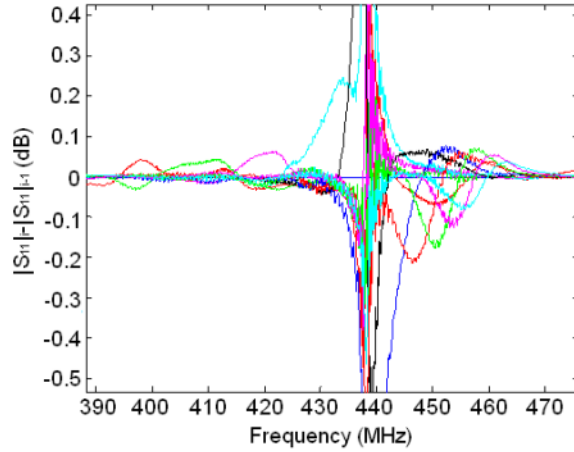


Figure 2.15: Experiment at $D_m = 50$ cm: Consecutive subtraction of $|S_{11}|_{i-1}$ curves from $|S_{11}|_i$ curves. In the experiment, d is changed from 0 to 10 mm in 10 steps.

2.3.6 The coupling frequency pattern

The one-to-one relationship between a displacement level and the corresponding frequency is not completely free of the relative positions of the sensor elements. Although a variation in the NSRR probe position (with respect to the antenna) creates small changes in the resonance frequency of the probe observed in the antenna reflection coefficient through electromagnetic coupling, these changes have to be characterized for the application of SHM, where very small values on the order of a few 10's of μm or microstrains are of interest. The experiment setup employed to obtain the coupling strength pattern can also be used to extract the 2-D map of the change of the resonance frequency. For this purpose, again 320 points are taken in a $20\text{ cm} \times 38\text{ cm}$ wide area. At each point, $|S_{11}|$ for the case where there is no NSRR present is subtracted from each $|S_{11}|$ curve. The resulting

curve is checked for the frequency of the local peak. These frequencies are shown as a 2-D color map, in a fashion similar to the coupling strength pattern, in Figure 2.16. The values in the color bar are in MHz. The resulting coupling frequency pattern again shows a distribution similar to the antenna illumination. The highest frequency is observed at the point where the electromagnetic coupling between the two sensing system elements is the strongest, which is a point in the radiating slot. It can be observed that there is still coupling when the NSRR probe is located 10 mm above the antenna in y -axis, but the reverse is not true; i.e., there is no coupling below the slot. Also, the resonance frequency decreases rapidly along both sides of the x -axis, unlike the case for y -axis. The conclusion that should be derived from this experiment is the following: The relative positions of the antenna and the NSRR probe should be kept as stationary as possible, in particular for experiments that require a high degree of resolution. Especially, a slight shift in the x -axis leads to a big change in the resonance frequency, disturbing the one-to-one relationship between d and resonance frequency that is characterized by a translation stage experiment similar to the one shown in Figure 2.7.

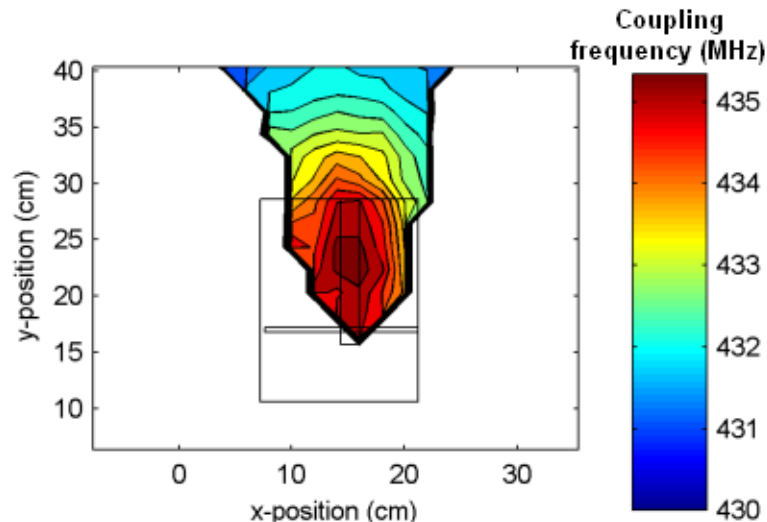


Figure 2.16: Color map demonstrating the coupling frequency, that is, the resonance frequency of the NSRR probe observed in the antenna reflection coefficient through electromagnetic coupling in a 2-D pattern. The antenna position is also shown on the plot. The values in the color bar are in MHz.

As mentioned before, d is fixed in this experiment. However, it has to be changing for the sensing to take place. Therefore, the change of the resonance frequency with a varying d should also be investigated. For this purpose, the position of the NSRR probe was again changed along the x - and y -axes. The origin was taken as the point where the feedline meets the slot, and the NSRR probe was located at the points changing from $y = -4$ cm to $y = 16$ cm in 4 cm steps along y -axis; and at the points changing from $x = -12$ cm to $x = 4$ cm in 4 cm steps along x -axis. Due to symmetry, measurements were not performed at additional points in the positive x -axis. At each point, d was changed from 1.4 to 3.4 mm in 0.2 mm steps. The frequency shifts are plotted in Figure 2.17 for all measurement points.

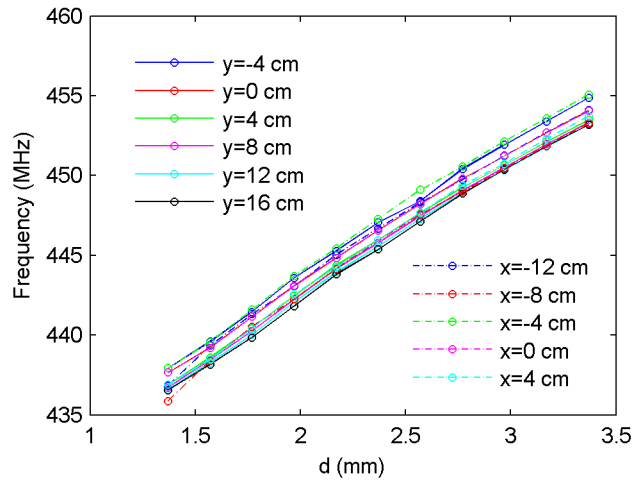


Figure 2.17: The change of the NSRR probe resonance frequency observed from the antenna reflection coefficient for different positions of the probe in x - and y -axes. d is changed from 1.4 mm to 3.4 mm in 0.2 mm steps at all points.

Figure 2.17 shows that the change of the NSRR probe position affects the resonance frequency observed from the antenna reflection coefficient, just as shown in Figure 2.16. This change is observed to be around 2.5 MHz at maximum. However, the slope of the change of the resonance frequency with respect to d is not affected, which determines the amount of change in the tracked parameter value, e.g., displacement or strain. In a real-life application, an original measurement which serves as a calibration for the other measurements is always necessary. Once the result of this measurement is known, it is not a problem to find the

change of displacement or strain from the frequency shift even when the position of the antenna and the NSRR probe is different than the $d - f_{res}$ curve obtained in laboratory conditions, since the slope stays the same for all cases in Figure 2.17.

2.3.7 Misalignments of the NSRR probe

Especially during the real-life applications (tensile tests, simply supported beam experiments, etc.), it is possible that the NSRR probe may experience misalignments in its position on the rebar. In theory, the direction of the line between two attachment points should be the same as that of the rebar; however, deflections may occur on the sensor due to the inhomogeneity of the external force. A possible misalignment where two NSRR probe parts on a rebar are rotated on the same plane towards each other is shown in Figure 2.18.



Figure 2.18: A possible misalignment where two NSRR probe parts on a rebar are rotated on the same plane.

The resilience of the sensing system to these misalignments was also characterized by translation stage experiments. The aim of the experiments was to identify to what extent several different types of possible misalignment scenarios could affect the readings. Among these misalignments are the bending of the faces of the

two NSRR parts with metal strips towards each other (called the inward bending, see Figure 2.19 inset) and away from each other (called the outward bending, see Figure 2.20 inset). Yet another possible type of misalignment is the twisting of the rebar, which causes the two NSRR parts to rotate in opposite directions around the rebar (see Figure 2.21 inset).

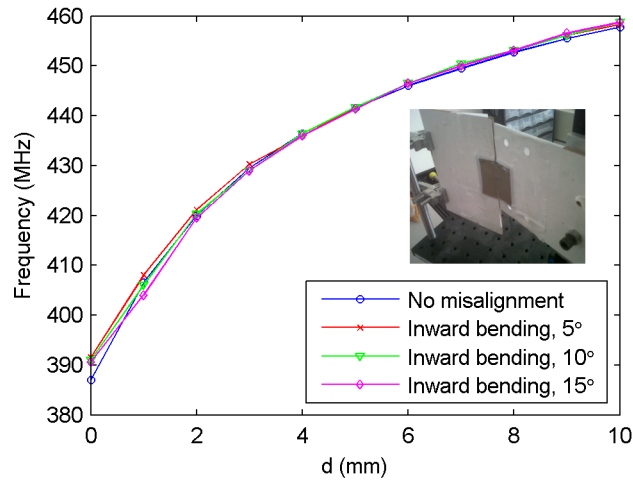


Figure 2.19: Inward bending of the NSRR probe parts characterized by recording the shift of sensing system frequency with d , given for three different angles: 5° , 10° and 15° . (Reprinted, with permission, from “Wireless Measurement of Elastic and Plastic Deformation by a Metamaterial-Based Sensor” by B. Ozbey, H. V. Demir, O. Kurc, V. B. Erturk and A. Altintas, *Sensors*, under the Creative Commons Attribution License (<http://creativecommons.org/licenses/by/4.0/>).)

In Figure 2.19, the sensing system frequency versus d is presented for the case when there is no misalignment and when there is an inward bending with the angles of 5° , 10° and 15° . The same characterization is shown for several angles in the case of outward bending in Figure 2.20 and in the case of twisting in Figure 2.21. The first two figures show that the bending of the NSRR parts does not have a major effect on the operation of the sensing system, since the curves obtained for these misalignments are no different than that without misalignment. The only possible discrepancy is experienced when $d = 0$ mm for the outward bending, since the resonance frequency difference between the case of no misalignment and the case of 15° bending is observed to be over 10 MHz. For twisting, the resulting deviation from the case of no misalignment is higher for smaller displacements, but as d is increased, this deviation is reduced. On the other hand, it should be

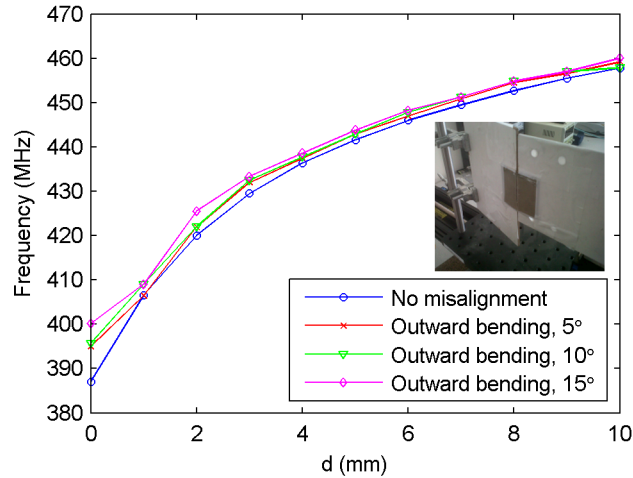


Figure 2.20: Outward bending of the NSRR probe parts characterized by recording the shift of sensing system frequency with d , given for three different angles: 5° , 10° and 15° . (Reprinted, with permission, from “Wireless Measurement of Elastic and Plastic Deformation by a Metamaterial-Based Sensor” by B. Ozbey, H. V. Demir, O. Kurc, V. B. Erturk and A. Altintas, *Sensors*, under the Creative Commons Attribution License (<http://creativecommons.org/licenses/by/4.0/>).)

emphasized that the angles of 5° , 10° and 15° are actually fairly extreme angles for such a twisting in practice, and they were selected to test the worst possible cases. Nevertheless, especially for $d = 0$ mm, the resonance frequency difference between the cases of no misalignment and twisting is quite high. This problem can be addressed by allowing an initial separation d between the two NSRR parts, e.g., 1 mm, and choosing this as the starting displacement value. Although this comes at the cost of reduced sensitivity of the sensor (which is still quite high), it increases the resilience of the sensing system to possible misalignment scenarios.

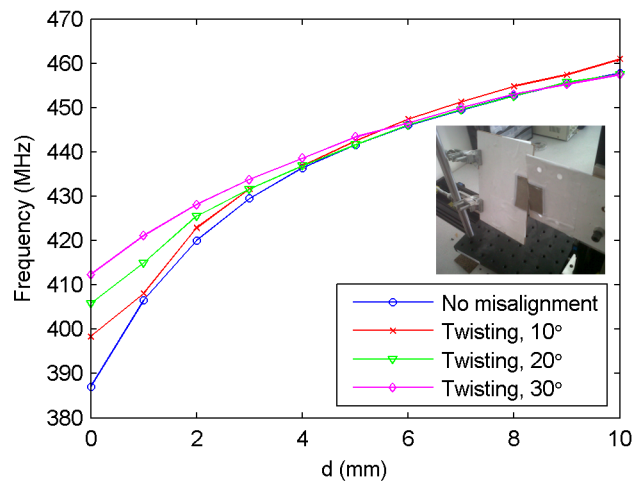


Figure 2.21: Twisting of the NSRR probe parts characterized by recording the shift of sensing system frequency with d , given for three different angles: 10° , 20° and 30° . (Reprinted, with permission, from “Wireless Measurement of Elastic and Plastic Deformation by a Metamaterial-Based Sensor” by B. Ozbey, H. V. Demir, O. Kurc, V. B. Erturk and A. Altintas, Sensors, under the Creative Commons Attribution License (<http://creativecommons.org/licenses/by/4.0/>).)

Chapter 3

Tensile Testing of the Sensing System

The main application of the sensing system is in SHM, where it can be exploited for the measurement of average strain and displacement between two points on a rebar used in reinforced concrete members such as beams or columns. Therefore, the performance of the sensing system on a steel rebar should be tested by tensile loading tests. These tests were carried out at the Structural Engineering Laboratory of the Civil Engineering Department at Middle East Technical University. In the tensile tests, an 8-mm diameter standard steel rebar is clamped between the two jaw faces in the vertical position, and the NSRR probe parts are fastened on the rebar, as shown in the photograph of the tensile test setup in Figure 3.1. The tests are carried out for both the elastic and plastic deformation regions of steel. Three strain gages are utilized for both calibration and comparison purposes in the elastic deformation region, while one extensometer is used for comparison in the plastic deformation region. The details of these experiments are covered in the following sections.

Some paragraphs in this chapter are reprinted, with permission, from “Wireless Measurement of Elastic and Plastic Deformation by a Metamaterial-Based Sensor” by B. Ozbey, H. V. Demir, O. Kurc, V. B. Erturk and A. Altintas, *Sensors*, vol. 14, pp 19609-19621 (2014).

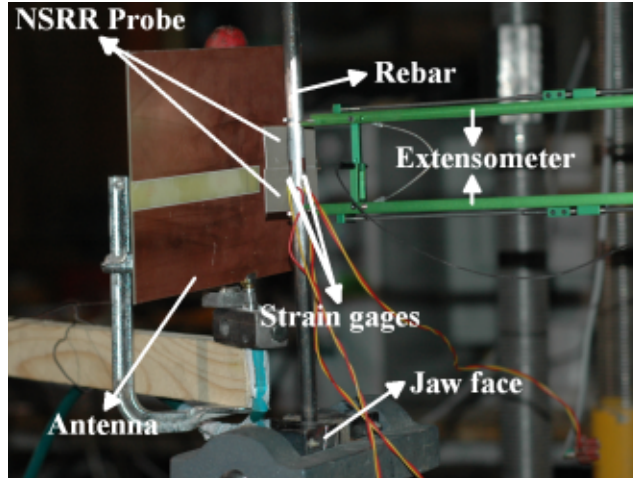


Figure 3.1: The tensile test setup shown with the sensing system elements antenna and the NSRR probe on a standard 8-mm diameter rebar. (Reprinted, with permission, from “Wireless Measurement of Elastic and Plastic Deformation by a Metamaterial-Based Sensor” by B. Ozbey, H. V. Demir, O. Kurc, V. B. Erturk and A. Altintas, *Sensors*, under the Creative Commons Attribution License (<http://creativecommons.org/licenses/by/4.0/>).)

3.1 Elastic deformation region

The first of the tensile tests was carried out in the elastic deformation region of the steel rebar. In the elastic region, the deformation occurring in the form of either elongation or contraction, is reversible, and not permanent. Although varying with respect to the type of the used steel material, the maximum level of strain observed in this region is generally below 1000 μ strains. In the first experiment, the rebar was pulled and elongated in the elastic range, where the force was linearly increased from 0 up to 800 kgF. During this operation, the NSRR probe was fixed on the rebar in a position where the gap between the two parts of the probe could extend with the development of displacement along the vertical direction, as shown in Figure 3.1. Each part of the probe was fixed using a strain gage adhesive on the rebar in the form of a point attachment (over a small area of several mm^2 s) for each part. As pointed out before, the purpose of the point attachment is to avoid the strain propagation through the hard epoxy onto the probe parts. This way, the probe detachment problem at high levels of strain is eliminated and possible misalignments are prevented.

These point attachments were located at the central points of the two NSRR parts and the contact points were carefully pre-cleaned off rust. For the average strain calculations, the starting separation between the point attachments was thus taken as the half of the NSRR chip edge length, which is 2.35 cm. The monitoring distance was 12 cm. The experiment was performed dynamically, i.e., in real time, where the network analyzer recorded the data at every 2 seconds. Simultaneously, the data corresponding to three strain gages connected to the acquisition system with wires are also collected at exactly the same instants with the same 2 seconds time step. The antenna and the strain gages can be seen in Figure 3.1. The positioning of the strain gages was arranged such that one of them was located directly across the probe and the other two were placed at two sides of the probe. The average of strains obtained from the gages placed at either side of the rebar gives the axial strain. This is independent of the possible skewness and bending of the rebar which are usually observed due to the imperfections of the tensile test setup. Thus, the average of strains obtained from the two strain gages facing each other were compared with the average strain calculated from the sensor reading and the strain gage across the sensor. A diagram showing the installment of the strain gages and the NSRR probe on the cross section of the rebar is presented in Figure 3.2. The force that was applied during the experiment and monitored from the load cell is plotted in Figure 3.3-a.

With the applied force, the local peak (or dip) in the antenna reflection coefficient corresponding to the NSRR probe becomes subject to a shift. Either the peak or the dip can be monitored in case it is characterized properly with an accurate calibration. For this experiment, the shift of the frequency of a dip point was monitored. This shift is shown in Figure 3.3-c. A calibration is needed to convert the frequency shift information of the sensing system into the strain. For this purpose, data obtained from the first experiment was utilized. Average strain values from the gages at each time instant were used for transformation of the frequency shift into strain in a linear fashion, and this transformation acted as a calibration for the other measurements. The tensile stress calculated from the applied force (by dividing the force by the initial cross-sectional area of the rebar) can be presented as a function of the microstrain forming in the vertical

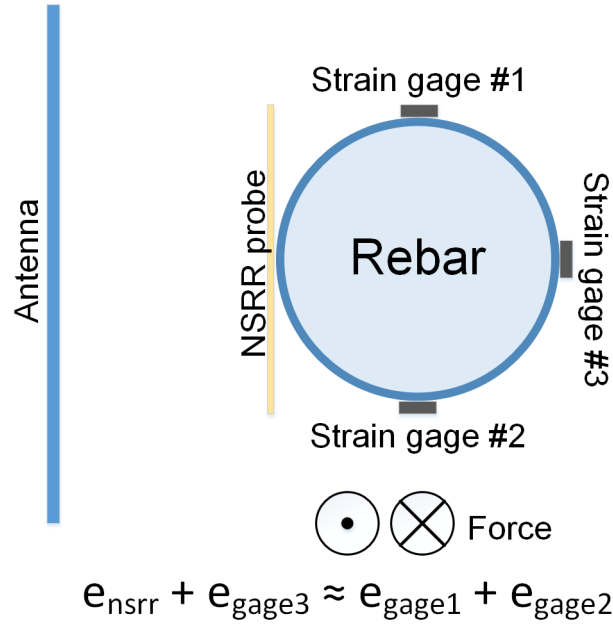


Figure 3.2: The installment of the strain gages and the NSRR probe shown on a cross section of the rebar. The sums of the strains read from the elements across each other are assumed to be the same.

direction on the rebar, as shown in Figure 3.3-b. For the elastic region, this curve is expected to be linear, and in fact, this is what is observed in the plot from the strain gage measurements. The sensing system readings are also observed to be closely following this line, demonstrating that the system can also function efficiently in the presence of a rebar touching the probe under high axial forces.

In another experiment, the force was applied in a cyclic regime, where it was increased from 0 to 1350 kgF and again decreased to zero linearly in a repetitive fashion for three cycles, as shown in Figure 3.4-a. Strain information obtained from the sensor and the average of the strains by the strain gages are plotted versus time in Figure 3.4-b. The frequency shift utilized to obtain this graph is again found by tracking the minimum points of the shifting dips in the frequency domain after applying a polynomial fit to each peak in order to minimize the effect of the system noise. In both experiments, due to a large additional capacitance introduced by the rebar, the NSRR resonance frequency drops from the original frequency of 400 MHz to a lower value. This value is around 299 MHz for the first experiment and it is around 289 MHz for the second experiment. The difference

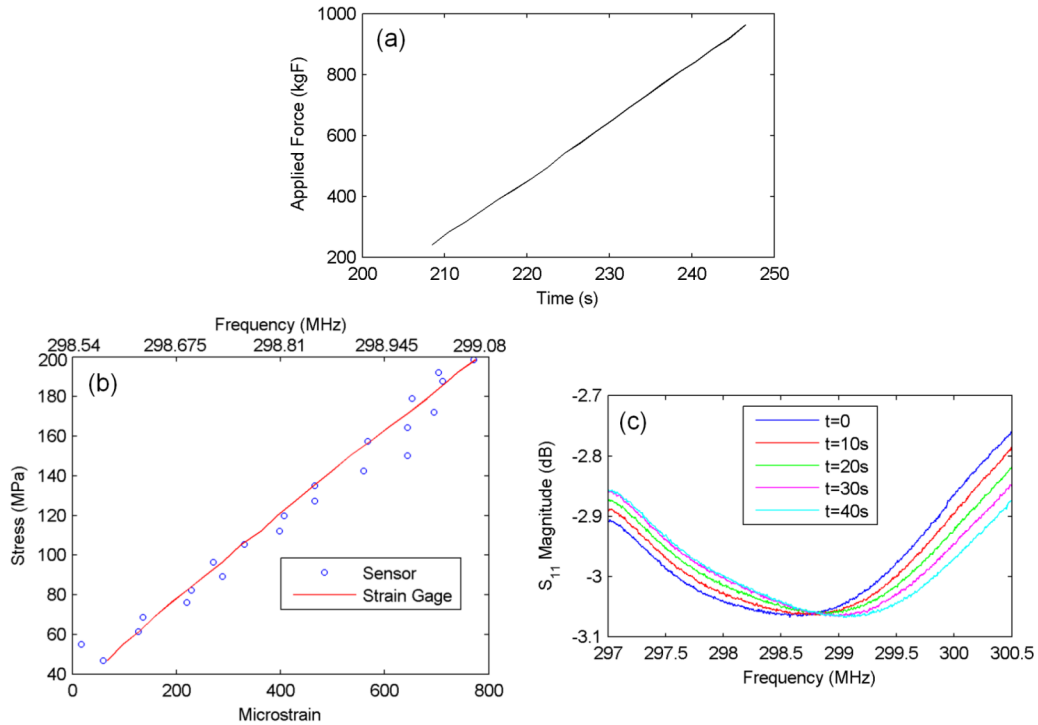


Figure 3.3: Elastic region experiment: a) The applied force versus time, b) Stress versus microstrain measured by the sensor, compared to the average of the strain gage readings. Corresponding resonance frequencies are also displayed on the upper horizontal-axis, c) Shift of the frequency minima over time as the force is linearly increased, which is used to plot (b). (Reprinted, with permission, from “Wireless Displacement Sensing Enabled by Metamaterial Probes for Remote Structural Health Monitoring,” by B. Ozbey, E. Unal, H. Ertugrul, O. Kurc, C. M. Puttlitz, V. B. Erturk, H. V. Demir and A. Altintas, *Sensors*, *Sensors*, under the Creative Commons Attribution License (<http://creativecommons.org/licenses/by/4.0/>).)

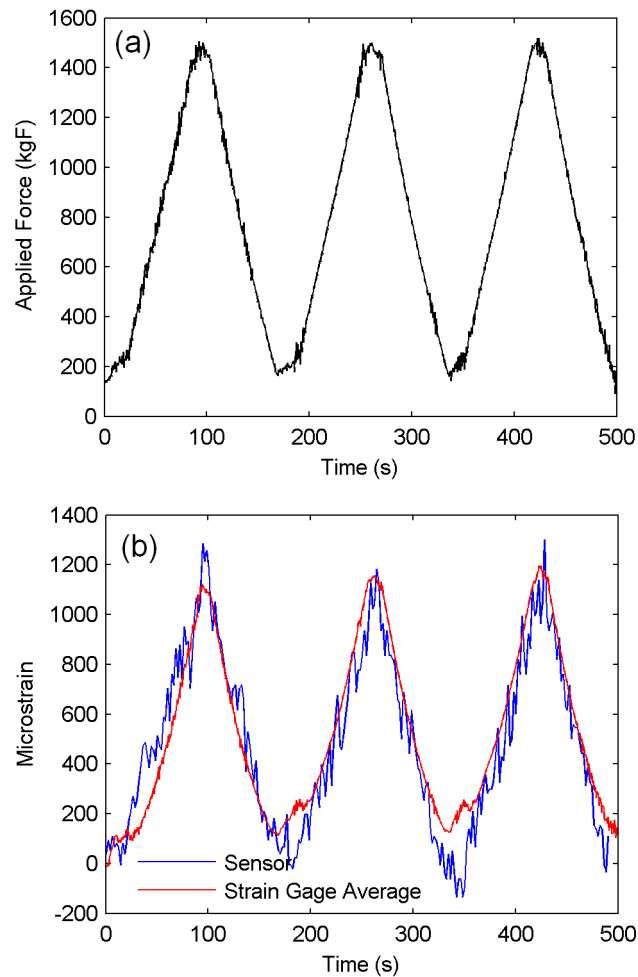


Figure 3.4: Elastic region experiment: a) Applied periodic force regime versus time, b) Strain measured in time by the sensing system compared to the average strain gage data. (Reprinted, with permission, from “Wireless Measurement of Elastic and Plastic Deformation by a Metamaterial-Based Sensor” by B. Ozbey, H. V. Demir, O. Kurc, V. B. Erturk and A. Altintas, *Sensors*, under the Creative Commons Attribution License (<http://creativecommons.org/licenses/by/4.0/>).)

is due to a slight change in the initial d values. For the second experiment, the minima of the shifting dips are observed to be varying from 288.5 to 289.1 MHz at each cycle. This is a very small change, corresponding to a frequency variation of 0.208% compared to the operation frequency of 289 MHz. The frequency shift information is converted to microstrain by using the calibration method described above. It is observed in Figure 3.4-b that both the sensing system and the strain gage data agree very well for the whole measurement range, i.e., part of the linear region that extends up to about 1200 microstrains. Loading the rebar with a periodic force regime is important in demonstrating that the sensing system shows no hysteresis-type behavior, and a specific frequency peak always corresponds to the same strain level, regardless of the applied force regime. This is especially significant since the result of this experiment shows a one-to-one mapping from the resonance frequency to strain or displacement (or vice versa) is possible.

Resolution of the sensing system in translation stage measurements was demonstrated as better than $1 \mu\text{m}$ in Chapter 2. For the elastic region experiments, strain measured by the sensing system is theoretically the additional displacement due to applied force divided by the original length between the attachment points of the NSRR probe, which is the midpoints of the two sensor parts and is equal to 2.35 cm. Therefore, the displacement resolution of $1 \mu\text{m}$ achieved in translation stage measurements corresponds to a strain resolution of $1 \mu\text{m}/2.35 \text{ cm}$, that is 42.5 microstrain. When Figure 3.4-b is examined closely, the minimum sensing system measurement steps are observed to vary between 100 and 200 microstrains. This shows that the sensor resolution degrades as a result of the noise introduced by the environmental effects and the effect of the rebar placed behind the NSRR probe in the setup.

3.1.1 Effect of the concrete cover

In a real-life scenario, it is frequently the case that a concrete cover is present between the antenna and the sensing structure located on the rebar, which is

the NSRR probe in this study. It has previously been shown in literature that concrete attenuates the RF signals due to its loss factor [101, 102]. The effects of the complex electromagnetic medium on sensing system will be covered in detail in Chapter 4. However, it can be predicted that the effect of concrete will be more significant in the elastic region, where the sensing is in the order of microstrains (based on slight frequency changes) and the results are much more prone to the effect of noise unlike the plastic deformation region, where a large range of displacement change is observed. To have an idea about how the sensing characteristics are affected in the presence of concrete, a concrete block of 4 cm in thickness was placed between the antenna and the rebar on which the NSRR probe was attached (see Figure 3.5-a). The concrete block represents the typical clear cover of a reinforced concrete member. The dynamic elastic region strain measurement was repeated with the concrete cover between the probe and the antenna. The rebar was loaded linearly from 0 force to 900 kgF and to zero again in one cycle. The results of this experiment are shown in Figure 3.5-b. It is observed in this figure that the sensing system can still track the strain in the presence of the concrete throughout the whole range despite the degradation of sensor resolution due to the increased level of noise. The data used for plotting Figure 3.5-b is the raw data from the measurements, where no post-processing is applied to exhibit the worst case scenario due to noise. Fluctuating components can be eliminated by several methods, e.g., simply by averaging or employing a low-pass filter. The calibration method used for transformation of the frequency shift to strain is the same as the one employed for the case without the concrete. A successful transformation using the same calibration for the no-concrete case also proves that a typical concrete cover does not constitute a significant attenuation on the near-field interaction between the antenna and the NSRR probe. This is a promising result, especially when it is considered that this scenario includes the effects of both the rebar and the concrete block on the sensing system. In a real-life scenario, the effect of the concrete cover and the reinforced concrete behind the NSRR on the sensor will be in the form of decreasing the resonance frequency of the coupled system even further by the large capacitance brought in by this medium, which is an amplified version of the case of introducing a single rebar. This effect can be dealt with by employing different calibrations for each

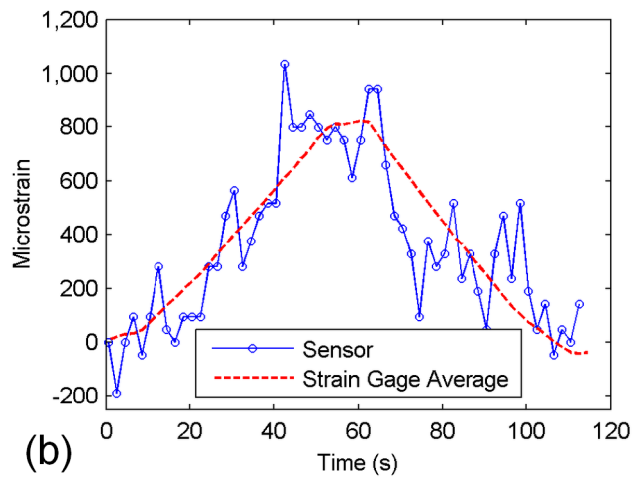


Figure 3.5: Elastic region experiment with concrete cover: a) The measurement setup with the concrete block serving as the clear cover, b) Strain measured in time by the sensing system compared to the average strain gage data. (Reprinted, with permission, from “Wireless Measurement of Elastic and Plastic Deformation by a Metamaterial-Based Sensor” by B. Ozbey, H. V. Demir, O. Kurc, V. B. Erturk and A. Altintas, *Sensors*, under the Creative Commons Attribution License (<http://creativecommons.org/licenses/by/4.0/>).)

medium. This way, a different strain-frequency shift mapping has to be obtained for each case.

3.2 Plastic deformation region

The plastic deformation region of steel is experienced when the level of strain induced on the rebar exceeds the elastic region limit of strain, called the yield point. The measurement of the deformation in plastic region also produces important information for understanding the level of damage during an overloading or an earthquake in which higher levels of relative displacement and strain are observed. It has been shown in Chapter 2 that the sensor can track displacements as large as 20 mm. This value is more than enough to be able to detect the displacement and strain levels that can be experienced in a reinforced concrete member prior to strength degradation. In such a plastic deformation experiment, the level of the applied force is increased to the degree that the strain forming on the steel rebar exceeds the elastic region limit. The force continues to be increased past the yield stress (observed at the point of yield strain), which signals the initiation of irreversible plastic deformation. Around this point, yielding is observed, where the stress level stays more or less the same, while the strain is increasing. Following this, strain hardening is initiated, where the stress-strain relationship becomes nonlinear and the ultimate tensile stress, which is the maximum stress level that can occur on the rebar, is measured. If the force continues to be applied to the rebar, necking occurs, and the rebar is fractured and torn into two pieces. Important stress points, such as yield and ultimate tensile stress and the corresponding strains are known for standard steel rebars used in structures. Therefore, the ability to measure strain provides valuable information about the possible physical damage in a structural member. A typical stress-strain curve for steel is shown in Figure 3.6.

An experiment was performed in the plastic region where the force was increased to 3750 kgF (see Figure 3.7-a), which lead the steel rebar to reach to its tensile strength point at about 500 MPa (see Figure 3.7-c). Although strain gages

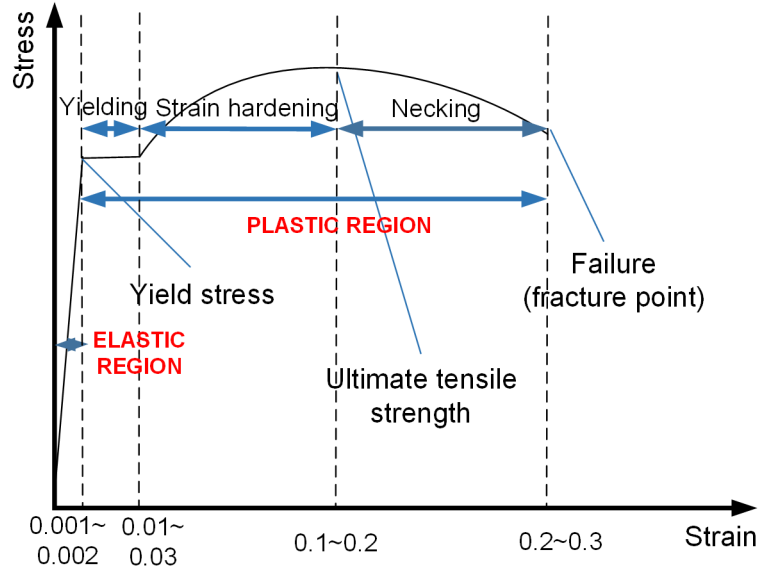


Figure 3.6: Typical stress-strain curve of steel.

function quite efficiently and without any significant noise in the elastic region, they cannot be used in the plastic region measurements, typically starting to break and to come off after a certain strain level (about a few thousand microstrains). Along with being wired, this is one of the two major drawbacks of the strain gages that prevent them being used extensively in real-life SHM. For this reason, for the plastic region measurements, extensometers are commonly used for measurement of relative displacement in laboratory setups. The extensometer used in these experiments can be seen in Figure 3.1.

The applied force reading obtained from the load cell through the data acquisition system is presented as a function of time in Figure 3.7-a, while the displacement readings from the sensing system and the extensometer are plotted in Figure 3.7-b. The displacement values used in this plot are the additional displacements to the distance fixed between the midpoints (attachment points to the rebar) of the two parts of the NSRR, which is 2.35 cm. Finally, the stress-strain curves obtained from the data acquired by the sensing system and the extensometer are presented in Figure 3.7-c. The elastic region ($t = 0 - 600$ s in Figure 4a), yielding region ($t = 600 - 660$ s) and the strain hardening region ($t > 660$ s) can all be distinguished in Figure 3.7-b. A fast increase in the displacement from a

small elastic yield strain value to around 0.9 mm is observed during yielding (see Figure 3.7-b). In the yielding region, the rebar cannot carry the applied load, and thus, this fast deformation continues until it restores its load carrying capacity due to strain hardening. After that point ($t = 660$ s), the displacement starts to increase up to 2 mm in a linear fashion.

Figure 3.7-b and 3.7-c reveal that the agreement between the sensing system and the extensometer data is quite well. The wireless sensing system readings follow the displacement data of the wired extensometer very closely. Here, it should also be noted that in Figure 3.7-b and 3.7-c, the noise present on the sensing system data is observed to be much weaker compared to that of the extensometer in the elastic region; and in the plastic region, their noise levels are more or less the same. In Figure 3.7-b, at the right vertical axis, measured resonance frequencies of the sensing system are also shown. As previously mentioned, there exists a one-to-one mapping between the displacement and the corresponding resonance frequency. To relate the resonance frequency shift to the displacement, we use a numerical fit derived from the extensometer displacement values read in the experiment that serves as a calibration. The numerical fit is chosen as an exponential-type of function, so that it reflects the nonlinear characteristics of the sensor that come into play for large displacements. This numerical fit will be discussed in detail in Chapter 4. Strain is calculated by dividing the sensing system displacement readings by the original length of 2.35 cm, which is the initial distance between the two attachment points of the NSRR parts. The strain corresponding to the extensometer readings is also calculated similarly, where the displacement values are divided by the original separation between the extensometer arms, which is 4.7 cm in our case. It should be pointed out that this value is twice the original sensor attachment point distance of 2.35 cm, since the extensometer is placed such that its arms touch the sensor from both sides, as shown in Figure 3.1. As before, stress is calculated by dividing the applied force to the circular cross-sectional area of the rebar. As previously discussed, the effect of the concrete cover in terms of the increased system noise is less evident in the plastic region measurements since the shifting range is much higher and the peaks can more easily be distinguished. Therefore, the sensing system is more resilient

to noise in the plastic deformation region. For this reason, as a representative case, only the elastic region measurements with the concrete cover are given.

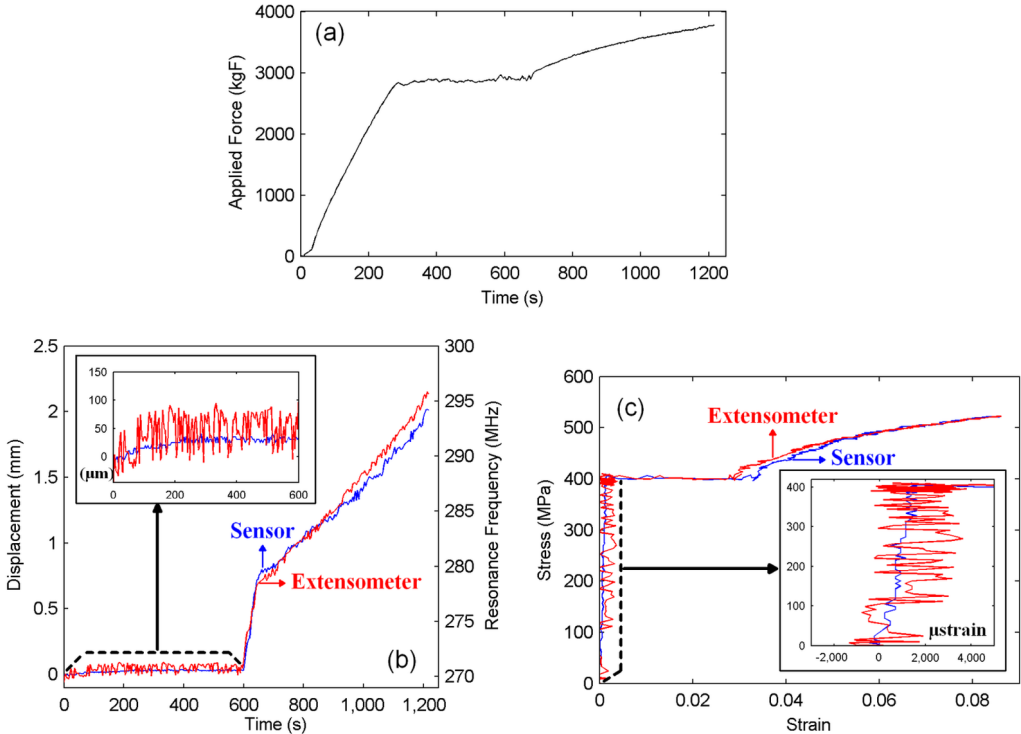


Figure 3.7: Plastic region strain and displacement measurements: a) The applied force, b) Displacement data from the sensing system compared to the extensometer data. Corresponding resonance frequencies of the sensor are also given on the right vertical axis. Top left: Zoomed elastic region (inset), c) Stress versus strain acquired from the sensor and from the extensometer. Bottom right: Zoomed elastic region (inset). (Reprinted, with permission, from “Wireless Measurement of Elastic and Plastic Deformation by a Metamaterial-Based Sensor” by B. Ozbey, H. V. Demir, O. Kurc, V. B. Erturk and A. Altintas, *Sensors*, under the Creative Commons Attribution License (<http://creativecommons.org/licenses/by/4.0/>).)

Chapter 4

Effects of the Complex Electromagnetic Medium on Sensing

In real-life SHM applications, the medium surrounding a wireless sensing system is a combination of concrete and rebar grid. The sensing NSRR probe is attached to the object on which the axial displacement between two points are to be measured. This object is generally a steel rebar employed in reinforced concrete structures, as discussed in previous chapters. In addition to the reinforced concrete wall at the backside of the probe, there is also a concrete cover present between the antenna and the probe. Configuration of the sensing system elements in a real-life measurement is shown in Figure 4.1. This electromagnetically complex medium generally has a detrimental effect on RF wireless sensors that interrogate backscattered fields. In order for a sensor to qualify for use in a real-life application, first the question of whether it can function well in the presence of such a medium should be addressed. Among the wireless passive strain

Some paragraphs in this chapter are reprinted, with permission, from “Wireless Sensing in Complex Electromagnetic Media: Construction Materials and Structural Monitoring” by B. Ozbey, H. V. Demir, O. Kurc, V. B. Erturk and A. Altintas, *IEEE Sensors Journal*, vol. 15, pp. 5545-5554 (2015).

and displacement sensors previously reported, this effect has not been systematically considered. Although the electromagnetic properties (relative dielectric constant, loss factor, loss tangent, conductivity, etc.), as well as the transmission and reflection properties of rebar grid, concrete and reinforced concrete in RF and microwave frequencies have been studied extensively in the literature [101–107], wireless sensing in their medium has not been demonstrated. In this chapter, the transmission and reflection characteristics of the complex medium elements and their effects on the sensing system will be covered.

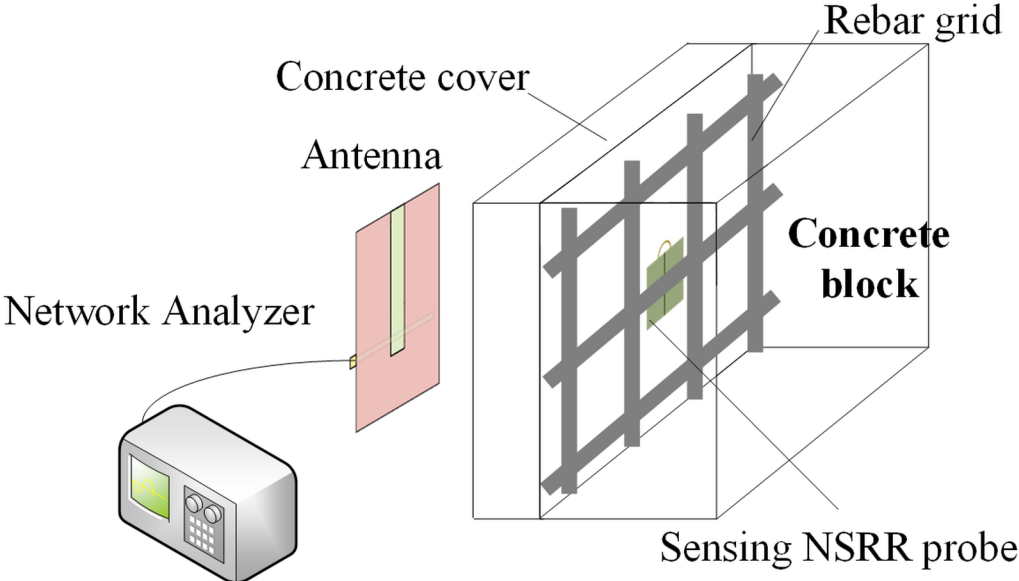


Figure 4.1: Configuration of the sensing system elements in a real-life application. (Reprinted, with permission, from “Wireless Sensing in Complex Electromagnetic Media: Construction Materials and Structural Monitoring” by B. Ozbey, H. V. Demir, O. Kurc, V. B. Erturk and A. Altintas, IEEE Sensors Journal © 2015 IEEE.)

4.1 Transmission through and reflection from the reinforced concrete

The transmission and reflection characteristics of the reinforced concrete were studied by Dalke et al. in [102]. In this study, it was shown that transmission through or reflection from a rebar grid is closely related with the unit cell length or period of the grid [102]. It was also demonstrated that above a certain free space wavelength approximately equal to this period, a metal rebar grid almost completely reflects the incident wave, acting as a perfect electric conductor [102]. The transmission-reflection characteristics of a rebar grid lattice with the dimensions of $P = 7.62$ cm and $D = 1.91$ cm, as shown in Figure 4.2-a, was also simulated in CST Microwave Studio. In the simulation, the rebar grid fragment was excited with a plane wave in a normal incidence. The results were observed to be the same for both the horizontal and vertical polarization. Here, P denotes the distance between two centers of the cylindrical rebars, and D is the diameter of the rebar. The rebar grid lattice simulated is shown in Figure 4.2-a, while the transmission and reflection characteristics are shown in Figure 4.2-b. In the figure, the first dip in reflection (also the first peak in transmission) is experienced at 3.36 GHz, corresponding to a wavelength of 8.93 cm. This brings the aforementioned conclusion: At frequencies below the first resonance point, which occurs at around $\lambda \approx P$, the rebar grid reflects the incident wave almost completely.

Dalke et al., also derived that a conducting concrete block produces periodic transmission maxima when the guided wavelength inside the concrete (λ_c) is equal to $2W$, W , $W/2$, $W/4$, \dots , where W is the thickness of the concrete. As an example, a concrete block with the following properties was simulated: $\epsilon_r = 6$, $\sigma = 1.95$ mS/m, $W = 20.3$ cm. Although the conductivity and the dielectric constant of concrete change with factors such as the age and the inner water content percentage, the above mentioned values are representative average values. The results are shown in Figure 4.3. The transmission curve oscillates between -0.4 dB and -3.2 dB, meaning that a total of approximately 6.4 dB can

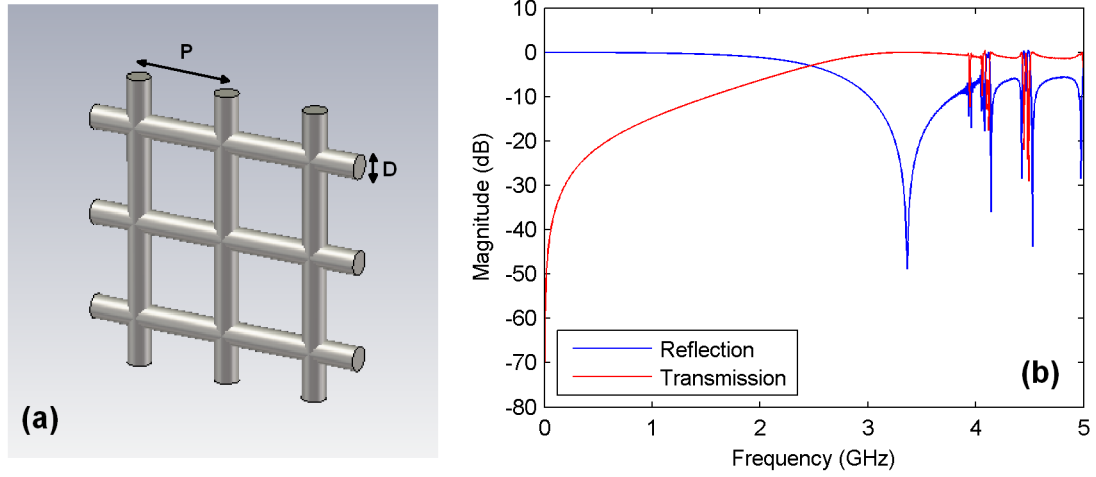


Figure 4.2: a) The simulated rebar grid lattice, b) Transmission through and reflection from a rebar grid lattice with the dimensions $P = 7.62$ cm and $D = 1.91$ cm.

be lost in a round trip of a transmitted signal for the worst case.

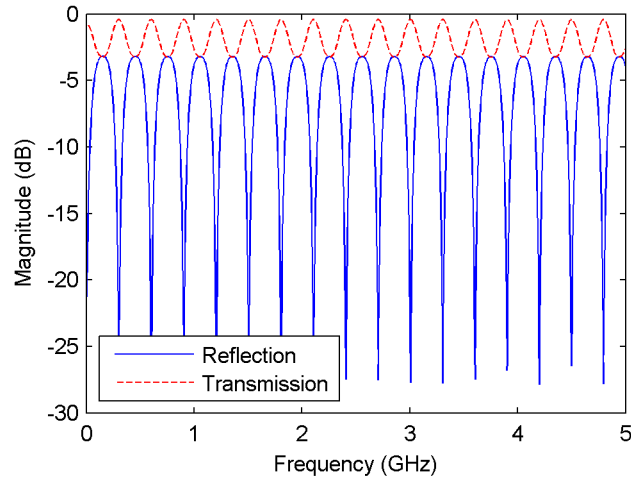


Figure 4.3: Transmission through and reflection from a concrete wall with the following properties: $\epsilon_r = 6$, $\sigma = 1.95$ mS/m, $W = 20.3$ cm.

In the case of a periodically reinforced concrete, these two elements are combined and their characteristics are superimposed. The resulting behavior is a more complicated function of both W and the rebar grid period [102]. The simulation results of such a reinforced concrete sample, where $P = 7.62$ cm, $D = 1.91$ cm and $W = 15.2$ cm, are shown in Figure 4.4.

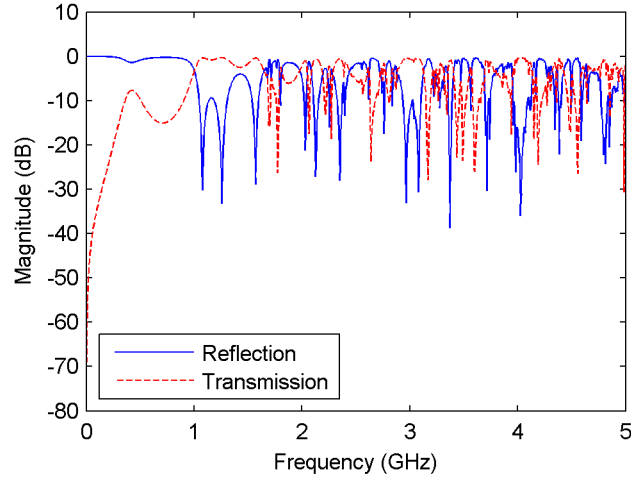


Figure 4.4: Transmission through and reflection from a reinforced concrete wall with the following properties: $P = 7.62$ cm, $D = 1.91$ cm and $W = 15.2$ cm.

As discussed in Chapter 3, in practice, there exists a clear cover at the outer wall of the reinforced concrete. Hence, it is inevitable that this relatively thin clear cover will be present between the antenna and the NSRR probe in a real-life application. In Chapter 3, the effect of this concrete cover was shown in the tensile tests for a 4-cm thick specimen. In reality, this thickness can be even smaller. For a thinner clear cover, the oscillation frequency of transmission through the concrete shown in Figure 4.3 is even lower. The relative permittivity of concrete is around 6, and at the operation frequency (400 MHz for Design A), the guided wavelength (λ_c) is around 30 cm. This λ_c is found to be appropriate for RF communication since a thin clear cover has a higher transmission coefficient [102]. Moreover, when Figure 4.4 is examined, it is seen that the concrete reinforced with the rebar grid on which the probe is attached, has a very high reflection coefficient at 400 MHz [102], which reflects all the electromagnetic signal back almost like a PEC. This means that there may be a contribution of reflections from the reinforced concrete in the signal retrieved by the antenna. In overall, at 400 MHz, the sensing system can be predicted to experience a relatively small amount of transmission loss.

4.2 Numerical fit to the calibration curve

As already mentioned in previous chapters, the method used to extract the displacement or strain information from the monitored frequency shift is essential, since this serves as a calibration for other measurements. A numerical fit should be used for characterizing the variation of the frequency shift with the displacement, or, d . However, the parameters of this numerical fit become subject to a change when the environment of the measurements changes from air to a complex electromagnetic medium constituted from concrete and rebar grid. Therefore, the modification of the fit parameters due to the effects of the complex medium have to be studied experimentally.

It was discussed in Chapter 2 that there are two controllable variables that determine the resonance frequency of the modified NSRR structure: 1) The end-to-end separation between the two electrically connected NSRR parts (d), and 2) the length of the jumper wire used to short the uppermost tooth (l) (see Figure 2.1). C_0 and L_0 are the effective capacitance and effective inductance of the unmodified comb-like NSRR (which is not divided into two moving parts with a jumper wire connecting them but instead is rigid and has a continuous metal line absent of the jumper wire). In essence, d is responsible for determining most of the structure capacitance, while l is important in determining most of the inductance. The changes of these parameters set a new f_0 for the whole structure, where f_0 is the effective resonance frequency of the NSRR without a jumper wire, i.e., when $l = 0$ and $d = 0$. As expected, an increase in d decreases the capacitance and thus increases the resonance frequency. Also, an increase in l increases the inductance and decreases the resonance frequency. The measured change of frequency with displacement for a range of 0-10 mm (except a 5 mm range for the sensor whose l is 1 cm), which is obtained on the xyz translation stage with no concrete or rebar included in the scenario, is shown for different jumper wire lengths in Figure 4.5.

It should be reminded that the medium is air for this translation stage measurement. It can be observed in Figure 4.5 that increasing the jumper wire length

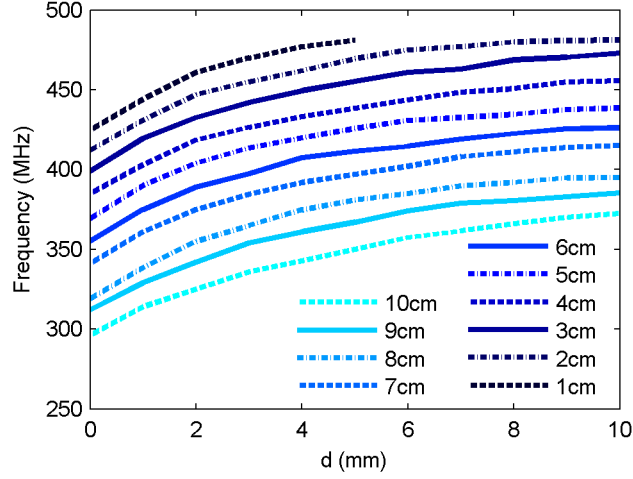


Figure 4.5: Measured sensor resonance frequency as a function of displacement (d), shown for different jumper wire lengths (l). Measurement performed on an xyz translation stage, where no rebar or concrete is present around the sensor elements.

is effective in decreasing the resonance frequency for any d value more or less by the same ratio. This becomes clear when all curves are plotted on top of each other by subtracting from each curve their corresponding $f(d = 0)$ values as shown in Figure 4.6. This figure also shows that the dependence of the change of frequency with d on l is somehow negligible, meaning that the capacitance is independent of l and is only altered by d .

As mentioned before, the calibration method is essential to extracting the displacement and strain information from the measured frequency shift. Although the relationship between the frequency and d was shown to be highly linear ($R^2 > 0.99$ over 5 mm) for specific regions in the displacement range in Chapter 2, for the entire range that can be detected by the sensor, it resembles a $(1 - e^{-x})$ type of curve as can be observed in Figure 4.5 and 4.6. For the purpose of calibration, a numerical fit can thus be applied to these curves as follows:

$$f_{fit} = \frac{k_1}{B}(1 - e^{-Bd}) + k_2 \quad (4.1)$$

In Equation (4.1), the parameters k_1 and B are constants, and remain the same for each l value and for the whole d range. k_2 , however, is the offset frequency

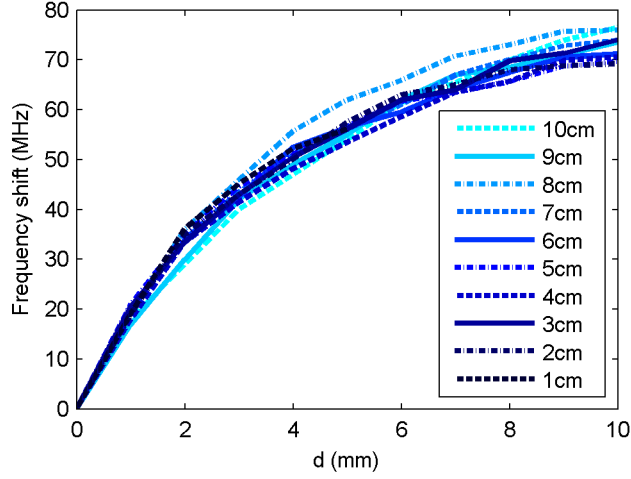


Figure 4.6: Measured change of sensor resonance frequency with displacement (d) for different jumper wire lengths (l), where $f(d = 0)$ is subtracted from each curve. Measurement performed on a translation stage, where no rebar or concrete is present around the sensor elements.

value which is experimentally shown to be linearly related to l and to f_0 as:

$$k_2 = f_0 - ml \quad (4.2)$$

where m is the slope of the k_2 versus l linear relation shown in (4.2). Note that, it is thus experimentally revealed that the relationship between f and l is also linear. For the translation stage measurements in free space, the values that yield the most convenient fit are found as $k_1 = 22.5$ MHz/mm, $B = 0.3$ mm⁻¹, and $m = 14$ MHz/cm, for a measured f_0 of 437 MHz. The fits with these values are plotted for each l in Figure 4.7.

It has been experimentally demonstrated by Figure 4.6 that the additional capacitance is independent of l and only depends on d . It is also clear that the inductance is largely independent of d and only depends on l (although this is not exactly true, it is a valid assumption for the sake of this argument. The dependence of L on d will be discussed in detail via the equivalent circuit model of the NSRR in Chapter 7). Therefore, d and l are two independent design parameters that set the resonance frequency by changing the overall C and L , respectively. On the other hand, the presence of a complex electromagnetic medium is also effective in changing the overall C , which results in an altered resonance frequency.

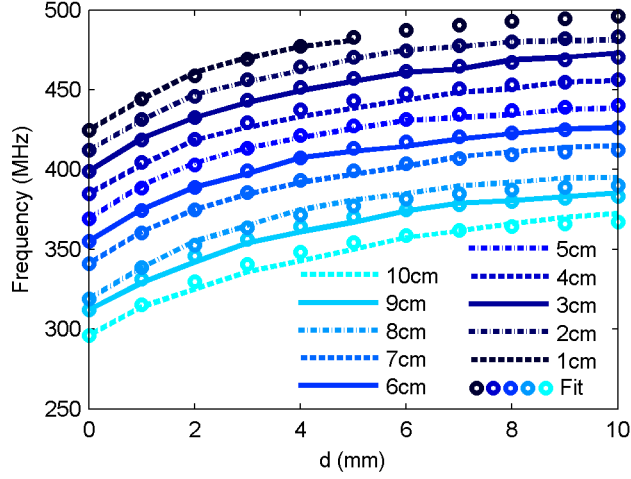


Figure 4.7: Change of the NSRR probe resonance frequency from measurement and numerical fit, for varying d , parametrized with respect to l . The numerical fit is exponential, which is plotted for each l . Measurement performed on a translation stage, where no rebar or concrete is present around the sensor elements.

In the next section, measured impacts of several combinations of the rebar grid and concrete block on the sensing system are shown, and their effects on the fit parameters are discussed.

4.3 Measurements in complex media

In the previous section, the measurement medium was free space and no element that could disrupt the sensing performance like a rebar grid or a concrete wall was present in the vicinity of neither the antenna nor the NSRR probe. In a real-life scenario, such a sensing structure should either be embedded inside the concrete or attached to the rebar just at the edge of the concrete wall. The NSRR probe is designed for use in the latter case, where its backside, which does not contain a ground plane or metal strips, is fastened on the rebar. Since the rebar is just at the edge of the concrete, its backside also makes contact with concrete, as shown in Figure 4.1. In addition, as a typical real-life application, there exists a relatively thin concrete clear cover between the antenna and the NSRR probe. This in turn leaves the NSRR probe completely confined within the concrete. The

cover and the reinforced concrete constitute a complex electromagnetic medium, and this medium affects the characteristics of the sensing system, including the shifting regime of frequency with displacement. In this section, results of various experiments are presented for several scenarios that involve combinations of these elements.

4.3.1 Effect of the rebar grid

For the given geometry and the dimensions used, the operation frequency of the sensing system is 400 MHz when the NSRR probe is in free space. Considering that the maximum standard rebar grid period is around 10 to 20 cm, it can be concluded that the rebar grid behaves as a perfect electric conductor at that wavelength. On the other hand, the size of the NSRR probe (4.7 cm \times 4.7 cm) is relatively small compared to the standard rebar grid period, and the NSRR probe only sees the effect of the part of the grid on which it is attached. Since the displacement or strain along one direction is measured, the NSRR probe is placed on the rebar such that the rebar is parallel to the tooth pairs. Therefore, the effect of the rebar grid on the sensing system is the same as that of a single rebar electromagnetically. The cylindrical rebar introduces an additional capacitance in parallel to the effective NSRR capacitance, and thus the resonance frequency is decreased. As expected, this decrease is related with the diameter of the rebar; a larger diameter implies more additional capacitance and a further reduced frequency. In Chapter 3, it was shown that the sensor is able to measure the displacement and strain successfully when attached on a rebar, which is pulled by a tensile loading setup. However, in that case, the 8-mm-diameter steel rebar touching the backside of the NSRR probe also resulted in a frequency drop of about 100 MHz. But this decrease did not hinder the operation of the sensor; only the numerical fit parameters used for the calibration should be changed.

For the first set of experiments in complex media, a rebar grid was placed behind the NSRR probe at a 1 cm distance. The antenna illuminated the NSRR from its front side as in the previous measurements. Behind the NSRR probe, a

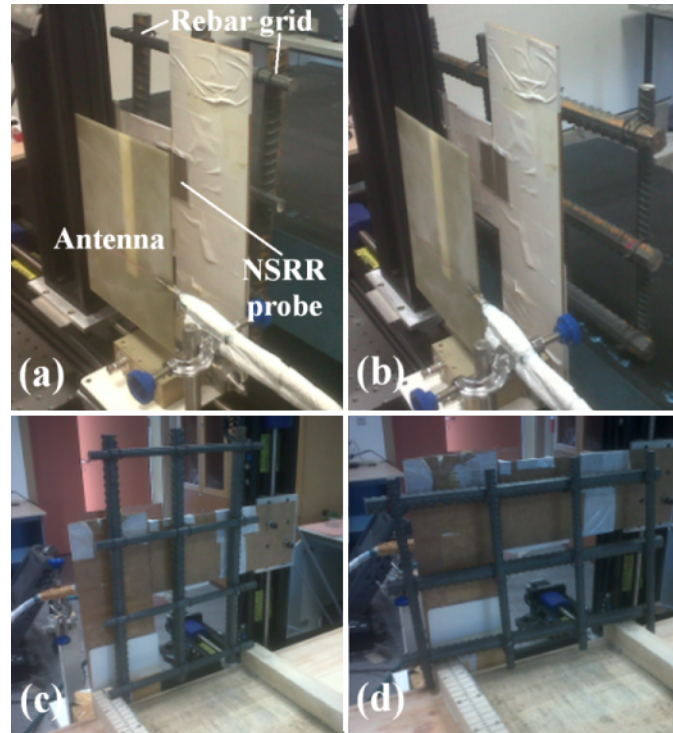


Figure 4.8: A fragment of the rebar grid placed behind the NSRR probe in a) vertical and b) horizontal positions. The backside images are shown in (c) and (d). (Reprinted, with permission, from “Wireless Sensing in Complex Electromagnetic Media: Construction Materials and Structural Monitoring” by B. Ozbey, H. V. Demir, O. Kurc, V. B. Erturk and A. Altintas, IEEE Sensors Journal © 2015 IEEE.)

2-D fragment of the 3-dimensional rebar grid was placed (see Figure 4.8), as normally would appear in a real-life scenario, only without concrete. This fragment of the rebar grid consisted of three parallel 16-mm-diameter rebars separated by a gap of 9 cm and four perpendicularly placed 10-mm-diameter rebars separated by a gap of 10 cm. The fragment of the rebar grid can be placed either in a position such that the thicker rebars are in vertical (Figure 4.8-a and Figure 4.8-c) or in horizontal position (Figure 4.8-b and Figure 4.8-d). The former and latter positions are denoted as vertical and horizontal placements, respectively. The difference between these two positions is the following: In the vertical position, the 10-mm-diameter rebars lie along the direction of the NSRR strip pairs, i.e., along the direction of displacement; while in the horizontal position, the 16-mm-diameter rebars lie along the direction of displacement. As pointed out,

the electromagnetic effects of these two positions are naturally different. The horizontal placement is expected to introduce more additional capacitance to the structure due to larger metal presence at the back of the NSRR, thus leading to a lower resonance frequency compared to both the no-rebar case and the vertical placement case.

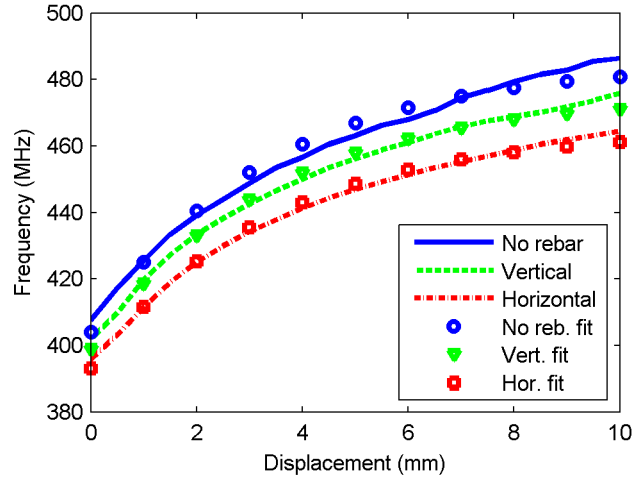


Figure 4.9: Translation stage measurements of the change of the sensor resonance frequency with d at the no-rebar case and for the cases of vertical and horizontal placement of the rebar grid fragment behind the NSRR probe, shown along with the exponential fits for each case. $l = 2$ cm in all cases.

The frequency shift versus displacement is shown for the no-rebar case as well as for the vertical and horizontal placements of the rebar grid in Figure 4.9. The jumper length is 2 cm for the measurements. The exponential fit explained before is also applied to each case in Figure 4.9. In each fit, different values for k_1 and k_2 are used, while other parameters remain unchanged. The set of the fit parameters used for each case is shown in Table 4.1. Figure 4.9 shows that the placement of a rebar grid 1 cm away decreases the resonance frequency approximately by 10 and 20 MHz in the vertical and horizontal positions, respectively. As mentioned before, the worst case occurs when the sensor is attached on the rebar in a touching position, leading to a decrease up to 100 MHz for a 8-mm-diameter rebar, as demonstrated in Chapter 3. However, even in that case, the sensing is not hindered, and frequency shift can be detected.

Table 4.1: Modification of fit parameters when a rebar grid is placed behind the NSRR probe in vertical and horizontal positions.

	k_1 (MHz/mm)	k_2 (MHz)
No rebar	24.3	404
Vertical	22.8	399
Horizontal	21.5	303

4.3.2 Effect of the concrete cover

For the second of the experiments in the complex medium, a 4-cm-thick concrete plate with surface dimensions of 70 cm \times 35 cm (see Figure 4.10) was placed between the NSRR probe and the antenna. As discussed before, this concrete plate represents the clear cover at the surface of the reinforced concrete. Since it is known that concrete is not a perfectly homogeneous material, the translation stage experiment was repeated for several different positions of the plate to check the effect of each case on the sensor operation. These positions include translation along the horizontal position to left and right with respect to a predetermined origin (center), elevation in the upwards direction, and 180° reverting of the concrete plate around its axis. Each scenario can be predicted to create minor changes on the variation of the sensor frequency with displacement. These changes are presented in Figure 4.11, where $l = 4$ cm for all measurements. This set of experiments shows that the effect of the concrete as a cover placed between the sensor elements is not very significant, creating a frequency decrease of at most 15 MHz at any d value while the slope remains almost the same. This also demonstrates that the concrete block can be considered as a homogeneous medium for our measurements, and the detection of frequency change behind the cover does not depend on the antenna position for a large range of d . The effect of the position of the antenna in real-life elastic deformation region measurements is discussed in detail in Chapter 5.

The resolution of the sensing system was shown to be at μm -level for measurements in free space, in Chapter 2. As the next characterization, the effect of the presence of a concrete cover between the antenna and the NSRR probe

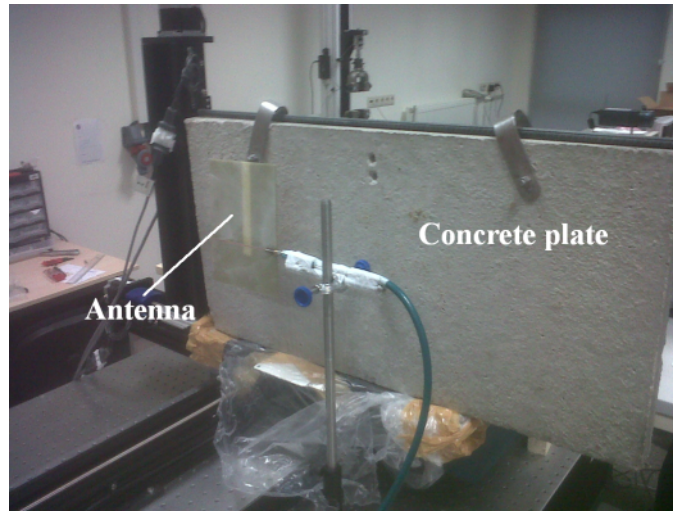


Figure 4.10: Experimental setup of the scenario in which a 4 cm thick concrete plate is present between the antenna and the NSRR probe. (Reprinted, with permission, from “Wireless Sensing in Complex Electromagnetic Media: Construction Materials and Structural Monitoring” by B. Ozbey, H. V. Demir, O. Kurc, V. B. Erturk and A. Altintas, IEEE Sensors Journal © 2015 IEEE.)

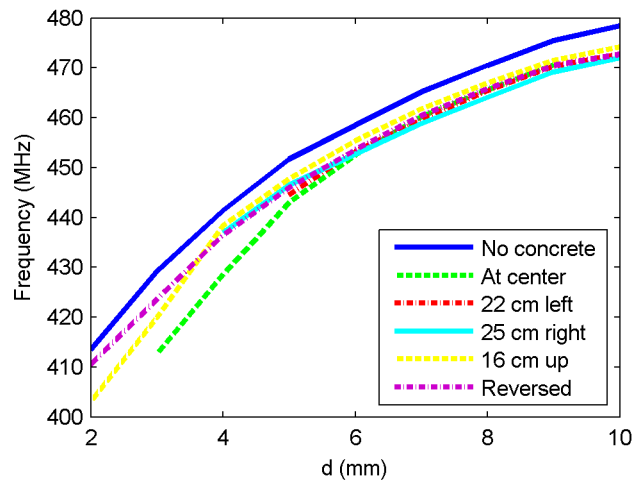


Figure 4.11: Measured change of the sensing system frequency with varying displacement for different placements of the 4 cm thick concrete plate between the antenna and the NSRR probe. (Reprinted, with permission, from “Wireless Sensing in Complex Electromagnetic Media: Construction Materials and Structural Monitoring” by B. Ozbey, H. V. Demir, O. Kurc, V. B. Erturk and A. Altintas, IEEE Sensors Journal © 2015 IEEE.)

on the resolution was investigated. The step size was selected as $1 \mu\text{m}$ for a d range of $30 \mu\text{m}$. l is 4 cm for the NSRR probe in the experiment. The frequency change with d is shown in Figure 4.12. It is observed that the resolution is still at μm level. The concrete plate experiments related with the drop of the resonance frequency and the resolution hold significance because the front cover is the only element whose effect on the sensor cannot be avoided. The problems introduced by complex medium elements like rebar and concrete core that stay behind the NSRR probe are easier to deal with; on the other hand, the cover always stands between the antenna and the sensing probe and its effect is inevitable. Since the performance of the sensing system is not affected significantly by the concrete cover, it is demonstrated that the proposed sensing system is highly favorable for structural health monitoring. The dynamic range is also shown to be large, which is basically limited by l , and can extend up to over 20 mm as shown in Chapter 2. Sensitivity also remains slightly affected and is still very good, with an average of around 7.5 MHz/mm in the worst case over the whole measured range.

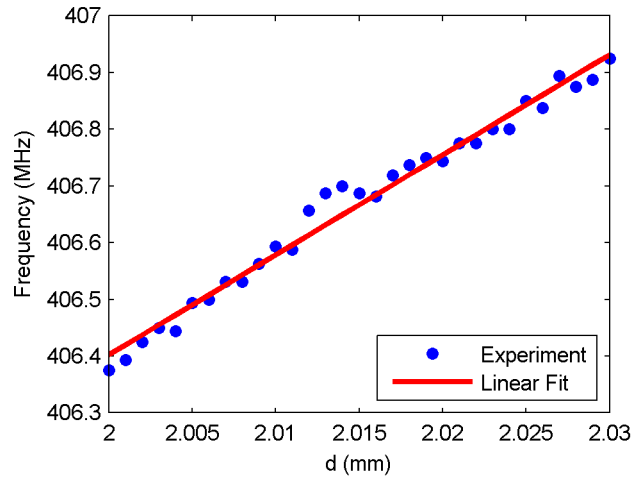


Figure 4.12: Measured resolution of the sensing system in the presence of a 4-cm-thick concrete plate: Sensing system frequency versus d for a $30 \mu\text{m}$ range with $1 \mu\text{m}$ steps, where $l = 4 \text{ cm}$.

4.3.3 Effect of the backside reinforced concrete

With the experiments whose results have been demonstrated until now, the placement of a rebar grid behind the NSRR probe, or that of a concrete plate between the antenna and the NSRR probe were demonstrated to affect the sensing system performance at a minimal level. However, placing a concrete block behind the NSRR probe can be expected to change the sensor characteristics due to the lossy nature of concrete. To understand these effects, a concrete block with the dimensions 20 cm \times 20 cm \times 30 cm was brought closer to the NSRR probe from behind on the translation stage. The experimental setup and the measured change of resonance frequency with d are shown in Figure 4.13 and Figure 4.14, respectively. The jumper wire length l is 4 cm for all measurements. In Figure 4.14, the numerical fits applied to the experimental data are also shown for each distance.

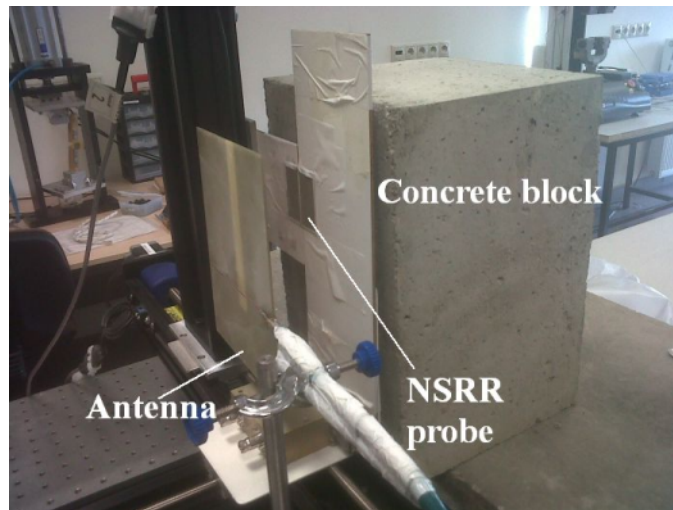


Figure 4.13: Experimental setup for the measurement of frequency change versus displacement when a concrete block is present behind the NSRR probe. (Reprinted, with permission, from “Wireless Sensing in Complex Electromagnetic Media: Construction Materials and Structural Monitoring” by B. Ozbey, H. V. Demir, O. Kurc, V. B. Erturk and A. Altintas, IEEE Sensors Journal © 2015 IEEE.)

This experiment demonstrates that the presence of a concrete block behind the NSRR starts to disrupt the signal at a distance between 3-5 cm, and for the

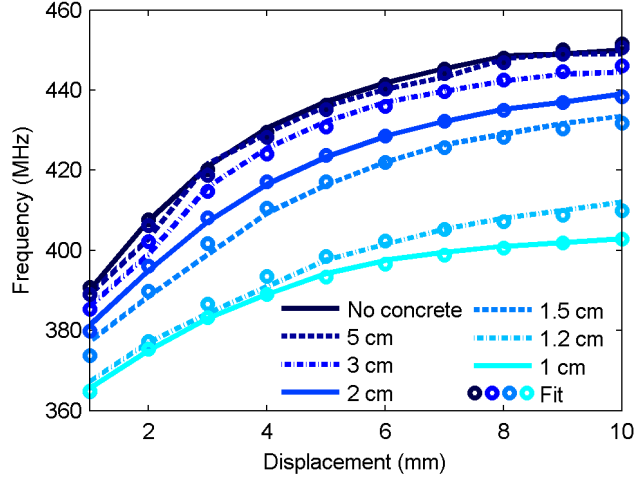


Figure 4.14: Measured change of sensing system frequency when the concrete block is behind the NSRR probe, shown for several concrete block distances. The exponential fits are also shown.

distances below this value, the frequency continues to decrease further. Consequently, below a specific distance, it dominates the sensing system response and the frequency shift cannot be tracked. In Figure 4.14, it is observed that the total frequency change, that is, the frequency difference between $d = 10$ mm and $d = 0$ mm, also decreases as the concrete block is brought closer to the NSRR probe. This is different than the effect of changing l , which is shown to introduce only a frequency offset at all d values in Figure 4.5. This impact can be described in the best way by observing the change of fit parameters k_1 and k_2 again, while other parameters remain the same. Table 4.2 gives the fit parameters for every concrete block distance, and Figure 4.15 shows the variation of these parameters graphically. We can understand that both the slope and the average of the frequency shift curves are subject to an exponential decrease as concrete block is brought closer, accelerating even further for distances below approximately 1.5 cm. Since the sensitivity of the system is defined as the change of frequency over a range of d , the placement of the concrete block behind the NSRR probe causes a severe loss of sensitivity. For distances shorter than 1 cm, the concrete block starts to disrupt the coupling of the system even more gravely, basically to the point that the frequency shifts start to be overwhelmed with the effect of the concrete background. This can be attributed to the finite conductivity of concrete, which

Table 4.2: Modification of fit parameters when a concrete block is placed behind the NSRR probe at several distances.

	k_1 (MHz/mm)	k_2 (MHz)
No concrete block	26.4	368
Concrete at 5 cm	26.7	366
Concrete at 3 cm	26.4	363
Concrete at 2 cm	25.4	358
Concrete at 1.5 cm	25.2	352
Concrete at 1.2 cm	19.7	348
Concrete at 1 cm	16.5	351

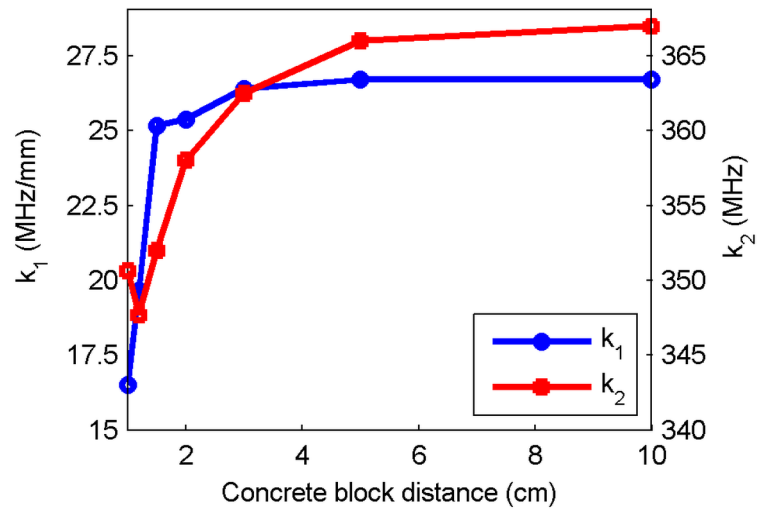


Figure 4.15: Graphical representation of the change of the fit parameters k_1 and k_2 with concrete block distance to the NSRR probe.

in turn causes the coupling between the antenna and the NSRR probe to be lost below a certain gap. Therefore, it can be deduced that a minimum distance of 1 cm should be kept between the existing NSRR probe geometry and the reinforced or unreinforced concrete. With the effect of the inevitable concrete cover already shown to be minimal, a thorough sensing system operation can be anticipated provided that this distance is preserved. The easiest way to maintain such a separation is to back the NSRR probe with an air-like dielectric material, that is, to fill the gap between the concrete core and the NSRR with a material whose electromagnetic properties are close to those of free space. A 1 cm thick separator fabricated from such a material can be split into two halves and can be fastened to the NSRR probe parts and to the rebar without difficulty. The idea is to use the separator in the same shape with the NSRR geometry and to have it freely moving with forming displacements so that the strain is directly transferred to the probe. The best choice of material for the separator is the polystyrene foam, since it is cheap and commonly used, and it is composed of 98% air which makes its electrical properties very close to free-space. Other dielectric materials (such as cardboard or wood) were observed to have the effect of increasing the overall capacitance of the NSRR probe and resulting in a decrease in the resonance frequency; hence, they are not favorable.

4.3.3.1 Effects of the age of the concrete and the presence of rebar grid inside the concrete block

In a real life scenario, the rebar grid is generally embedded inside the concrete behind the NSRR probe and it may be expected to change the electromagnetic behavior of the complex medium. Yet another factor that can affect this behavior is the age of the concrete. It is known that the electromagnetic properties of the concrete become subject to change with time, as it dries slowly. In order to test these effects, four concrete blocks with the same dimensions as the one shown in Figure 4.13 were prepared. The first block incorporated a 3-dimensional rebar grid. The second block, which was prepared one month later, did not contain any rebar grid inside. The third and fourth blocks were prepared at the same day and

two months after the second block, and one of them contained a rebar grid while the other did not. In the experiment, these concrete samples were placed at a 2 cm distance behind the NSRR probe with a jumper length of 4 cm. The comparison of the results for the last two blocks is useful in understanding the difference between a reinforced concrete sample and an unreinforced one which are prepared on the same day. On the other hand, comparison of the first and second cases with the last two cases gives an idea on the effect of the concrete age on the sensor performance. Therefore, the effects created due to both the age and the rebar grid content of the concrete blocks can be comprehended by these experiments. The change of frequency for all these samples are shown in Figure 4.16. Figure 4.16 shows that even though there is a variation of frequency shifting regime among different combinations of reinforced and unreinforced concrete blocks with varying ages, this variation is only around 6 MHz at maximum for any d value. The deviation of this beam of curves from the no-concrete case is due to the disruptive nature of the concrete block itself. Hence, the age factor, and whether the concrete is reinforced or unreinforced makes a little change in terms of the sensing system performance.

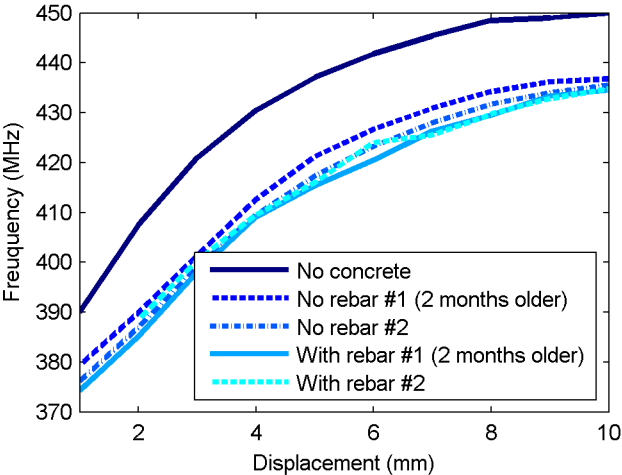


Figure 4.16: Change of frequency with displacement for three different concrete samples with varying ages and rebar grid presence. The blocks are placed at a distance of 2 cm behind the NSRR probe.

Chapter 5

Simply Supported Beam Experiments

A real-life-compatible testing is the final step for the operation of the sensing system. In this chapter, the results of a simply supported beam experiment, which was carried out with this purpose, are reported. In the simply supported beam experiment, an actual scale beam sample is put under the test where it bends due to the point load applied to the center of the beam. In this setup, the NSRR probes were installed on the bottom longitudinal steel bars to detect the axial deformation of the bar as the vertical force was applied. The experiments were carried out at the Structural Engineering Laboratory of the Civil Engineering Department at Middle East Technical University. These experiments constitute the last step for finalizing the sensing system for real-life use. It is, to the best of our knowledge, also the first account of a real-life experiment with a wireless and passive sensor utilized for SHM. A completely functioning RF displacement/strain sensing system that is resistant to the disrupting effects of the complex electromagnetic medium constituted by the concrete and rebar grid holds a significant value. Such a real-life experiment also brings in several practical challenges. The

Some paragraphs in this chapter are reprinted, with permission, from “A Wireless Passive Sensing System for Displacement/Strain Measurement in Reinforced Concrete Members” by B. Ozbey, V.B. Erturk, H.V. Demir, A. Altintas and O. Kurc, *Sensors*, vol. 16, p. 496 (2016).

solutions to these challenges are discussed throughout this chapter.

5.1 Experiment setup

In the simply supported beam experiments, the NSRR probes were integrated into a beam sample, completely surrounded by concrete (see Figure 5.1 for step-by-step preparation of the experiment setup). The experiments were conducted on this beam with the dimensions of 300 mm \times 400 mm \times 2950 mm (width, depth, length). The beam was placed horizontally on two fulcrums at each side along the length of the beam and a vertical force was applied by hydraulic pistons from the middle section downwards so as to bend the reinforced concrete beam and to create an axial strain on the bottom longitudinal bars (see Figure 5.1-e). The rebar grid inside the beam sample incorporated five 16-mm diameter deformed bars as well as 8-mm rectangular stirrups placed with 20 cm separation. For the integration of the sensing probes, an 8-cm wide and 5-cm deep cavity was created at the bottom of the beam by using a polystyrene block as a formwork before the concrete was poured. The polystyrene formwork and concrete were rasped to reach the surface of the rebar, followed by the attachment of the NSRR probes on the rebars. As suggested in Chapter 4 by the results of the experiment where a reinforced concrete block was placed immediately behind the NSRR probe, a 1-cm thick polystyrene spacer was used as a separator for eliminating the disruptive effect of the reinforced concrete behind the NSRR probe on the electromagnetic coupling. The final form of the NSRR probes including the polystyrene separators are shown in Figure 5.2. Each of the two parts of the separator was fixed on the rebar using a silicone paste through small cylindrical plastic pieces in order to have a point attachment. This way, the effect of strain propagation from rebar to the NSRR is minimized. With the addition of polystyrene layer, plastic pieces and rasping of the periphery of the rebars, the distance between the back of the NSRR probe and the concrete surrounding the rebar was measured to be around 1.2 cm.

A set of four NSRR probes were employed in the experiment. They were

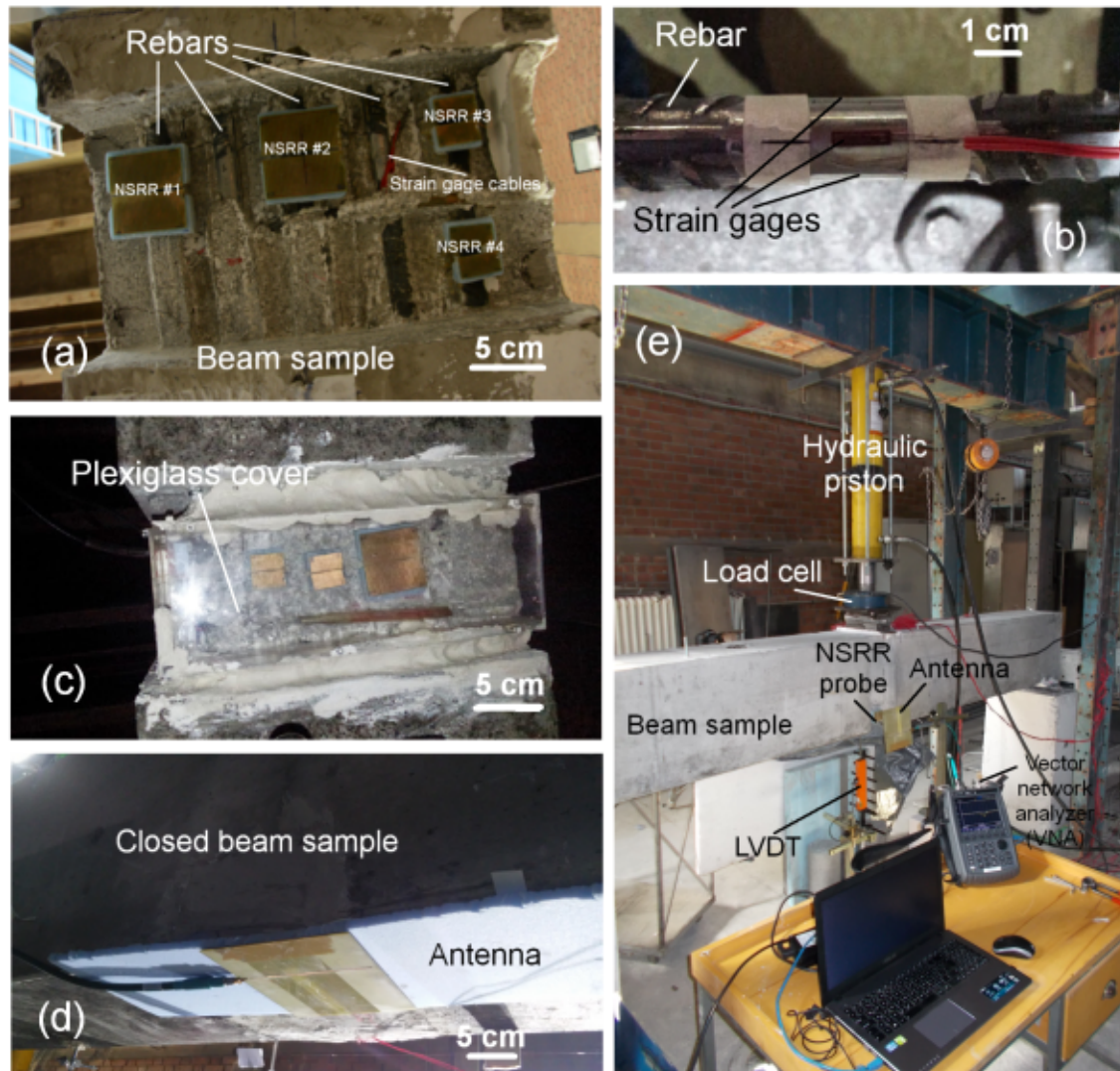


Figure 5.1: a) The arrangement of the NSRR probes actually used in the experiment at the bottom of the beam, b) Close-up of a strain gage attached on a rebar before the concrete beam is produced, c) Placement of the protective plexiglass cover in front of the NSRR sensors (not the actual setup used in the experiment, but from a beam sample used for the preliminary tests before the actual experiment), d) Placement of the antenna at the bottom of the beam, which is closed with a plaster layer after the placement of the sensors and the plexiglass cover, e) Simply supported beam experiment setup, where the slot antenna and a representative NSRR probe are shown at one side of the beam (the preliminary test setup). (Reprinted, with permission, from “A Wireless Passive Sensing System for Displacement/Strain Measurement in Reinforced Concrete Members” by B. Ozbey, V.B. Erturk, H.V. Demir, A. Altintas and O. Kurc, *Sensors*, under the Creative Commons Attribution License (<http://creativecommons.org/licenses/by/4.0/>).)

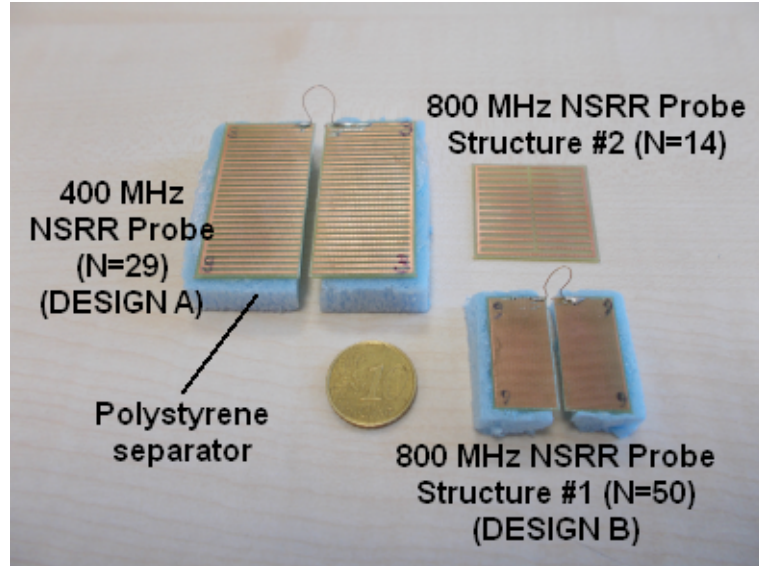


Figure 5.2: The 1-cm thick polystyrene foam separators fastened to the back-sides of the NSRR probes. (Reprinted, with permission, from “A Wireless Passive Sensing System for Displacement/Strain Measurement in Reinforced Concrete Members” by B. Ozbey, V.B. Erturk, H.V. Demir, A. Altintas and O. Kurc, *Sensors*, under the Creative Commons Attribution License (<http://creativecommons.org/licenses/by/4.0/>).)

fabricated in one of the following two geometries mentioned in Chapter 2, namely, Design A and Design B (see Figure 5.2). As previously described, Design A has an original resonance frequency of around 400 MHz, has a bigger footprint (4.7 cm \times 4.7 cm), and incorporates 29 metal ring lines each of which has a thickness of 0.8 mm. On the other hand, Design B has an original resonance frequency at 800 MHz, has a smaller footprint (2.5 cm \times 2.5 cm) and incorporates 50 metal rings with a thickness of 0.2 mm. As again pointed out in Chapter 2, the original frequency of an NSRR sensor, which occurs when there is no strain on the rebar, can be fine-tuned by the initial edge-to-edge distance d set between the two NSRR parts. In the experiments, on the first and the third of the five rebars at the bottom of the beam, NSRR #1 and NSRR #2, (in Design A) were attached, respectively. Two small-size sensors in Design B were located side by side on the fifth rebar, denoted as NSRR #3 and NSRR #4. No sensor was connected to the second and fourth rebars in order to prevent the intercoupling between the sensors. The arrangement of the sensors at the bottom of the beam

is shown in Figure 5.1-a. After the attachment of the NSRR probes, a concrete-gypsum mix based plaster layer was placed to close the gap of the beam. To protect the probes from this plaster, a plexiglass cover was used in front of the probes as seen in Figure 5.1-c. The final form of the beam is presented in Figure 5.1-d. For the comparison of the data measured by the sensing system with an accurate reference, Kyowa KFG-5-120-C1-11L5M2R strain gages were employed (see Figure 5.1-b). At each rebar, three gages were placed with 90° separation. The strain on a rebar was measured by an NSRR probe at one face, two strain gages at each side, and another opposing one, which was across the rebar. Vishay 5100B Scanner was used as the data logger.

As in all previous characterization and tensile tests, the microstrip single slot antenna was employed for interrogating the NSRR probes. For this purpose, a new antenna operating at 800 MHz was designed. As expected, the bandwidth of the 800 MHz system is larger compared to 400 MHz system, while the latter has an interrogation distance advantage over the former. Since the antenna acts as the transceiver in the single channel communication between the antenna and the NSRR probe, only one of these systems can be employed for monitoring strain at the same time with one network analyzer. On the other hand, the systems do not affect each other and undisturbed responses can be obtained from each probe at different measurements. Since the antenna acts as the transceiver in the single channel communication between the antenna and the NSRR probe, only one of these systems can be employed for monitoring strain at the same time with one network analyzer. A very important feature of the sensing system is that it can read data from both NSRR #1 and NSRR #2 at the same time by a single antenna. This way, information corresponding to different rebars can be acquired in a single frequency sweep. For this multi-point sensing capability, the resonance frequency of the sensors have to be close to each other. This unique wireless multi-point sensing property of the system will be discussed in detail in Chapter 6.

During the preliminary tests, two criteria have been identified as being very critical in terms of the success of the experiment and the accuracy of the results. These points are given as follows:

1. The concrete has to be rasped until the rebars are visible and the sensors have to be attached directly on the rebars instead of on the concrete. This is vital since the propagation of strain from the rebars onto the concrete is experimentally observed to be hindered by formation of cracks on the concrete. This results in a failure to correctly capture the elongation or contraction. When the sensors are placed directly on the rebars, sensing becomes possible.
2. The antenna has to be kept at a constant distance from the sensors (normal to the sensor surface), with respect to the moving beam sample. The reason is that the disruptive effect of the relative positions of the antenna and the NSRR probes on the electromagnetic coupling is amplified by the presence of the concrete. The effect of the relative positions of the antenna and the NSRR probes is observed to be minimal at a large dynamic range (such as thousands of microstrains or a few millimeters of displacement), but becomes very critical in the elastic deformation region of steel where the maximum displacement is in the order of a few tens of micrometers. Thus, the correct location of the antenna should be determined, which can be done by moving the antenna in the plane parallel to the sensor surface until the same resonance frequency peaks, obtained in laboratory conditions, are observed again on the beam setup. When the location of the antenna is determined, the transformation curve produced by laboratory experiments can be applied directly to convert the frequency shift into displacement and strain. In our experiments, steady positioning of the antenna is achieved by fastening it on the beam through a polystyrene layer as shown in Figure 2-d. These two criteria have been taken into account at all experiments on the actual beam sample for obtaining the results given in the next section.

5.2 Elastic deformation region

On the beam sample, several load-and-release experiments were performed within the elastic deformation region of the steel rebars. The variation of the vertical

force applied to the beam and monitored via the load cell in one of the elastic-region experiments is given in Figure 5.3-a. As seen in the figure, the force was first increased slowly to 3 tons with the manual hydraulic piston; and then, the piston was released so that the system had a net force equal to 0 in the first 45 s. It was then increased to 5 tons and again decreased to 0. Finally, it was increased to 7 tons and decreased to 0 once again. As in the tensile tests, the reasoning behind the incremental loading to different force levels is to see how well the sensing system can follow the force-deformation regime, and to observe its response to different force levels. As a result of the loading and releasing, the separation between the NSRR probe parts is increased and decreased, respectively, leading to first a reduction and then an increment in the overall capacitance of the sensor. As before, we expect the frequency shift with time to follow the strain gage results, and to more or less follow the force regime in the elastic range. It is also expected that the movement of this peak should be matching the behavior measured from the strain gages. The shift of the frequency peak of NSRR #1 can be observed in the system reflection coefficient plots recorded at every second during the experiment, as shown in Figure 5.3-b.

When the NSRR #1 peak frequencies of the raw data corresponding to every time instant are plotted, the blue curve shown in Figure 5.3-c is obtained. Although the level of noise is high for the blue curve obtained from the raw data, it can still be noticed that the shape of the frequency shift is quite similar to the one obtained from the strain gages. Several numerical methods can be implemented to eliminate the noise and obtain a better curve. Among these, two have been given special attention. First method is to design and apply a low-pass filter to discard the high frequency components in the waveform. With this goal, the Fast Fourier Transform (FFT) of each curve was taken and a proper cut-off frequency of the filter was determined by inspection of the spectrum. Then, a 100th order FIR filter was designed and was applied to the signals. Maxima of each curve were used to plot the frequency shift. The resulting waveform is plotted with red in Figure 5.3-c. The second method is based on curve-fitting. A 5th degree polynomial fit was applied to a selected region around the peak of each reflection coefficient curve, and the maxima of each fit were found afterwards. The

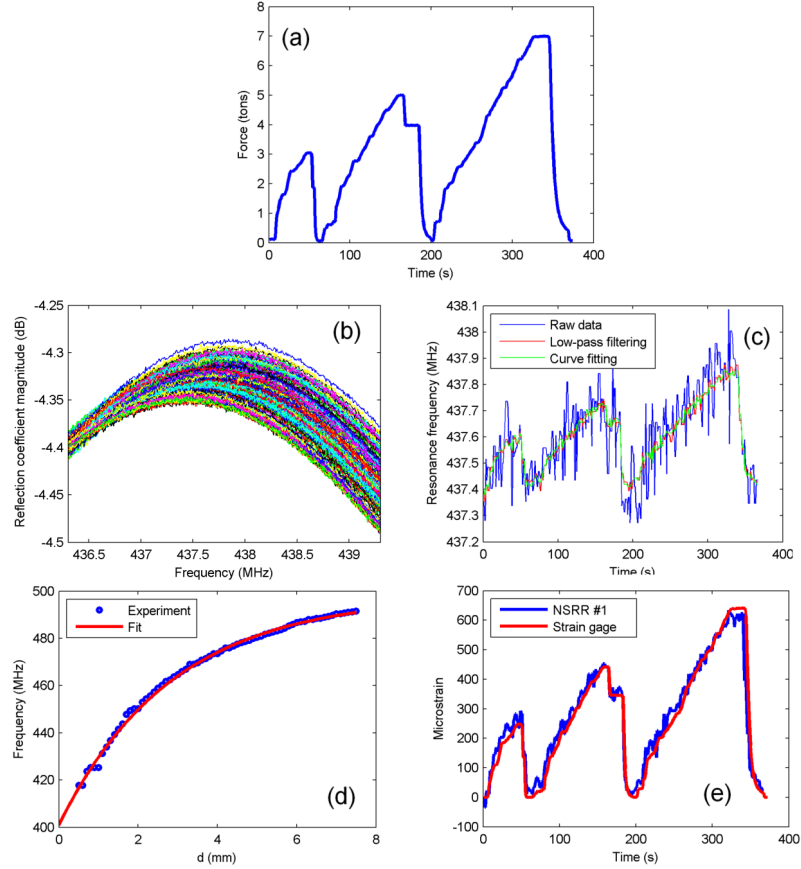


Figure 5.3: Elastic deformation region experiment results of NSRR #1: a) Applied vertical force read from the load cell, b) Shifting of the NSRR #1 resonance frequency peaks with strain forming due to applied load, c) NSRR #1 peak frequency plotted by using the raw reflection coefficient data (blue), after a low-pass filter is applied to the raw data (red), and after 5th degree polynomial fitting is applied to the raw data (green), d) The transformation curve obtained in laboratory before the beam experiments by a controlled translational stage, which is used for converting the frequency shift into displacement and strain, e) Strain obtained by the NSRR #1 plotted versus time, and compared to the data from the strain gages. (Reprinted, with permission, from “A Wireless Passive Sensing System for Displacement/Strain Measurement in Reinforced Concrete Members” by B. Ozbey, V.B. Erturk, H.V. Demir, A. Altintas and O. Kurc, *Sensors*, under the Creative Commons Attribution License (<http://creativecommons.org/licenses/by/4.0/>).)

polynomial degree, the number of data points and the width of the region were all selected heuristically. The result is plotted with green in Figure 5.3-c. When all three curves are compared, it is clear that both methods help to dispose of the noise significantly, but neither the curve resulting from the low-pass filtering nor the curve fitting has a distinct advantage over the other. This implies that both methods can be utilized for post-processing the frequency shift data. For the sake of maintaining consistency, we proceed with filtering for all the plots in this chapter.

As shown in Chapter 4, the transformation (or calibration) curve which is used to convert the measured frequency shift data into displacement and strain, strongly depends on the properties of the complex electromagnetic medium formed by the concrete and metal rebar grid. Therefore, two different calibrations can be defined for two limiting cases: 1) When the surrounding medium is air, i.e., it is assumed that the sensing system is completely free of the disrupting effect of the concrete and the rebar grid, 2) When the 1-cm-thick polystyrene foam is placed between a reinforced concrete block and the NSRR probe. In practice, it is neither of these two cases but something in between, since the distance of the back of the NSRR probe to the reinforced concrete is actually more than 1 cm due to the rasping and the presence of cylindrical plastic pieces. An experimental curve obtained by a controlled translation stage when the medium is air is given in Figure 5.3-d along with the exponential fit. The slope of this curve is decreased due to the effect of the concrete, as shown in Chapter 4. Here, the curve utilized for the transformation of the resonance frequency shift into the displacement change takes into account the effect of the reinforced concrete and is described as $f(d) = 410 + 75(1 - e^{-0.35d})$. For this fit, the distance between the NSRR probe and the concrete is taken as 1.2 cm. As before, the inverse of this fitted curve is used to convert the measured frequency shift into the displacement. In order to calculate strain, the displacement is divided to the distance between the attachment points of the two parts of the NSRR, which is 26 mm for NSRR #1.

Strain data obtained from NSRR #1 and from the strain gages are plotted versus time in Figure 5.3-e. As mentioned before, at each rebar, three strain

gages were placed at the same location with the midpoint of the NSRR probe such that each element makes a 90° spacing with its neighbor. As the beam bends due to the applied vertical force, the bottom longitudinal rebars not only elongate but also bend. Bending of the rebar causes the displacements at the top and the bottom of the rebar to be different from each other. In order to cancel the effect of the bending of the rebar and to calculate the axial deformation of the bar only, the sum of the strains of the opposing elements (i.e., the elements across each other) are assumed to be the same. The data for the strain gages which is compared to the data from the NSRR sensor is actually the result of the subtraction of the strain of the gage across the NSRR probe from the sum of the strains from the two neighboring gages. The strong matching shows that the system can correctly track the elongation and the contraction of the rebar with a micrometer-level sensitivity, and employing the translation stage calibration yields accurate results.

Elastic deformation experiments were repeated and data from other NSRR probes were also recorded. The data for NSRR #2 and NSRR #3 are shown in Figure 5.4 and Figure 5.5, respectively. The distance between the attachment points of NSRR #2 is 30 mm. For NSRR #3, which has a smaller footprint geometry, this value is 10 mm. The strain obtained by NSRR #2 is observed to agree with the strain gage data closely. On the other hand, for NSRR #3, the data is much noisier compared to the data of the bigger footprint probes. This can be attributed to poor coupling between the probe and the antenna and more dominating effect of the clutter in higher frequency.

In Chapter 3, the sensing system was shown to acquire accurate data at tensile tests where a single rebar with a diameter of 8 mm was elongated under the effect of a vertical force. In the simply supported beam experiments, the beam undergoes bending deformation where the transverse loading causes compressive strains at the top and tensile strains on rebars at the bottom. Despite the presence of concrete surrounding the rebar, both experiments are observed to yield similar results. In the elastic region, where the induced deformation is reversible, the maximum level of strain is around 2000 microstrains. Thus, this value set a maximum limit for the experiments, where the maximum strain level attained was

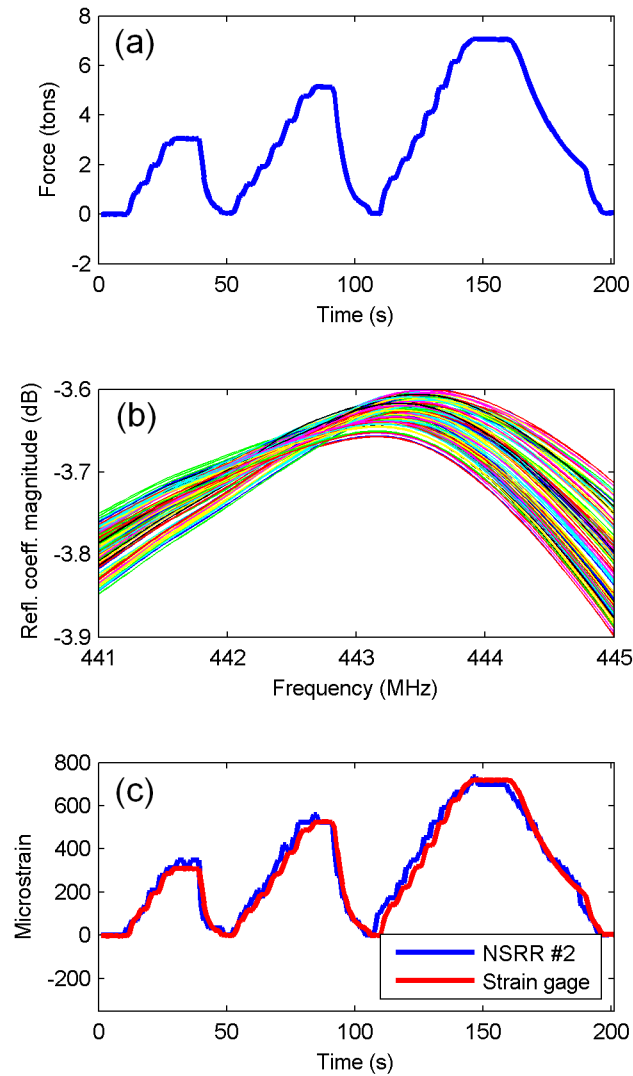


Figure 5.4: Elastic deformation region experiment results of NSRR #2: a) Applied vertical force read from the load cell, b) Shifting of the NSRR #2 resonance frequency peaks with strain forming due to applied load, c) Strain obtained from NSRR #2 plotted versus time, and compared to the data from the strain gages. (Reprinted, with permission, from “A Wireless Passive Sensing System for Displacement/Strain Measurement in Reinforced Concrete Members” by B. Ozbey, V.B. Erturk, H.V. Demir, A. Altintas and O. Kurc, *Sensors*, under the Creative Commons Attribution License (<http://creativecommons.org/licenses/by/4.0/>).)

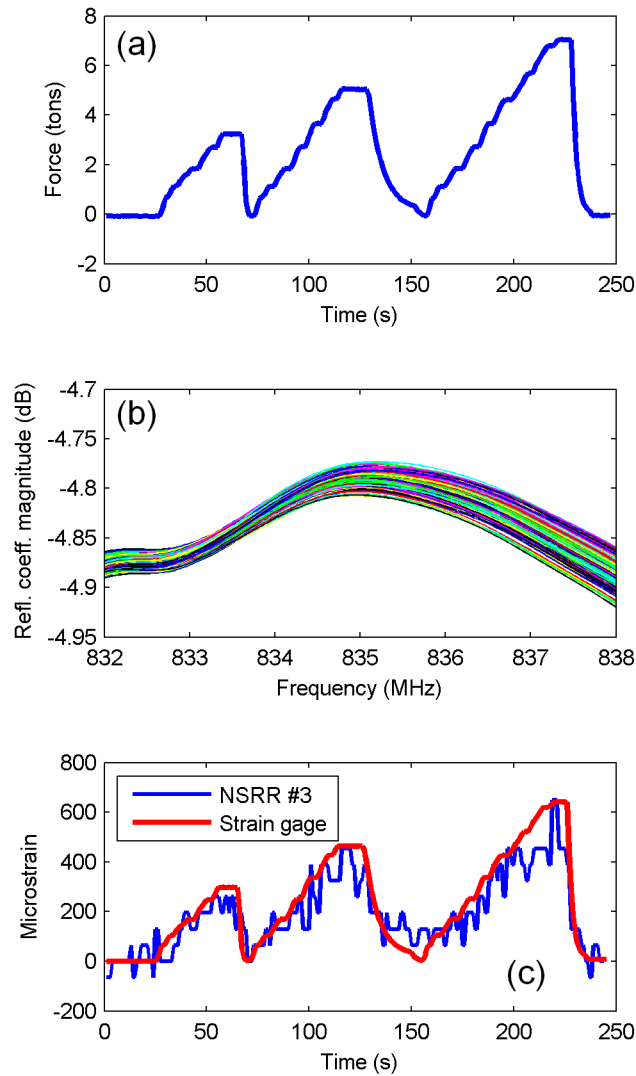


Figure 5.5: Elastic deformation region experiment results of NSRR #3: a) Applied vertical force read from the load cell, b) Shifting of the NSRR #3 resonance frequency peaks with strain forming due to applied load, c) Strain obtained from NSRR #3 plotted versus time, and compared to the data from the strain gages. (Reprinted, with permission, from “A Wireless Passive Sensing System for Displacement/Strain Measurement in Reinforced Concrete Members” by B. Ozbey, V.B. Erturk, H.V. Demir, A. Altintas and O. Kurc, *Sensors*, under the Creative Commons Attribution License (<http://creativecommons.org/licenses/by/4.0/>).)

around 800-900 microstrains. In the elastic measurements, it is important that the proposed sensing system can record accurate data at such small strain levels, especially when the following challenges are considered: 1) The fact that the sensor moves up and down with the vertical force applied on the beam (mechanical changes generally result in deviations in the data, especially in elastic region), and, 2) The environment measurement is a complex electromagnetic medium. The elastic deformation behavior of the beam is observed through application of a cyclic force regime. Within the elastic deformation range, the relationships between every parameter (force, stress, strain, relative displacement, etc.) are linear. These linear relationships can clearly be seen in Figure 5.3, Figure 5.4 and Figure 5.5, where it is observed that the ratio of the force to the strain stays more or less the same during the whole experiment.

5.3 Discrete-time measurements

In addition to dynamic measurements where the sensing system collects data continuously for a period of time, another real-life application is to take measurements at different time instants, e.g. for periodic inspection. Experiments were also carried out for testing the discrete time measurement performance of the sensing system. For this purpose, 8 different levels of force were applied on the beam, the first and the last of which being 0 tons, as shown in Figure 5.6-a. The sensing system recorded measurements for a period of time at each force level. The values of strain forming at each force level are shown in Figure 5.6-b for both NSRR #2 and the strain gage. In Figure 5.6-c, the random force and strain values are sorted and average microstrain value is plotted versus applied force. It can be observed in the figure that the agreement between the strain gage and sensing system data is once again quite well. Averaging of the data is important in reducing the system noise level that can be increased due to any electrical or mechanical change in the surrounding environment. In the discrete-time sensing experiment, the frequency shift from 0-strain case to the maximum (690 microstrains) strain case is measured as 460 kHz. Since the distance between the attachment points of NSRR #2 is 30 mm, the relative displacement between

the two points is $20 \mu\text{m}$, which yields a sensitivity of 22 MHz/mm . Distinguishing kHz-level peak shifts is possible via the network analyzer, and hence, we can obtain a resolution in microstrains level. These values can be considered as fairly sufficient for SHM of reinforced concrete members.

5.4 Plastic deformation region

An important capability of the sensing system is to monitor displacement and strain at the plastic deformation region of steel, where traditionally used devices such as strain gages fail to capture due to their limited dynamic range. The measurement limit of the strain gages is closely related with the way they are installed on rebars. Generally, strong adhesives are used for this purpose, but such an installation approach only enables elastic region measurements (strains up to 0.2 - 0.3%), after which the strain gages tear down since the strain forming on the rebar causes the adhesives to rip off. Special measures must be taken for high elongation measurement (fracture strain of rebar, i.e., in the order of 20 - 30%) but they require practical challenges such as curing at elevated temperatures for several hours, special protective coating, and special surface preparation procedures. These severe installation demands are very difficult to apply at a real-life application. On the other hand, it was demonstrated that the sensing system could successfully measure strains until the fracture of the rebar at a steel rebar in the tensile tests.

Data was recorded for both NSRR #1 and NSRR #2 during the plastic deformation experiment in the tensile tests. The loading regime during the experiment is shown in Figure 5.7-a. The loading was first increased to 25 tons from $t = 0$ to $t = 2287$ s. At $t = 2287$ s, the force on the beam was decreased to the point of no loading, and it was again increased to 25 tons in a shorter period of time. Then, at $t = 2900$ s, loading was stopped before the beam failed. The absolute value of the displacement of the bottom midpoint of the beam sample was monitored by a Linear Variable Differential Transformer (LVDT), and the result is plotted in Figure 5.7-b. It can be observed that the beam became subject to a maximum of

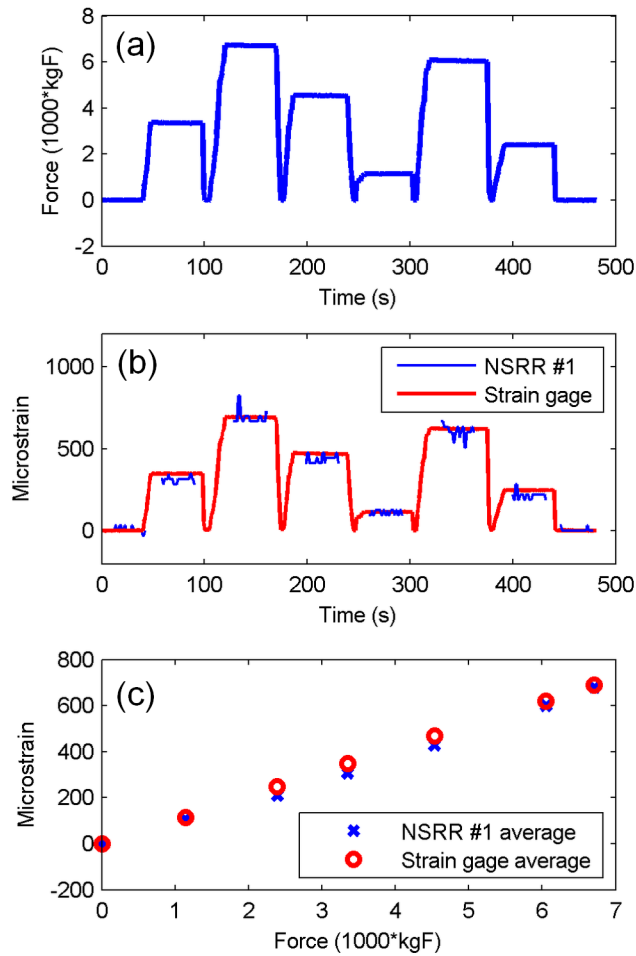


Figure 5.6: Discrete-time measurements: a) Applied force levels, b) Strain read by the sensing system with NSRR #2 and by strain gages, plotted versus time, c) Average of the strain values for each force level plotted versus the force. (Reprinted, with permission, from “A Wireless Passive Sensing System for Displacement/Strain Measurement in Reinforced Concrete Members” by B. Ozbey, V.B. Erturk, H.V. Demir, A. Altintas and O. Kurc, *Sensors*, under the Creative Commons Attribution License (<http://creativecommons.org/licenses/by/4.0/>).)

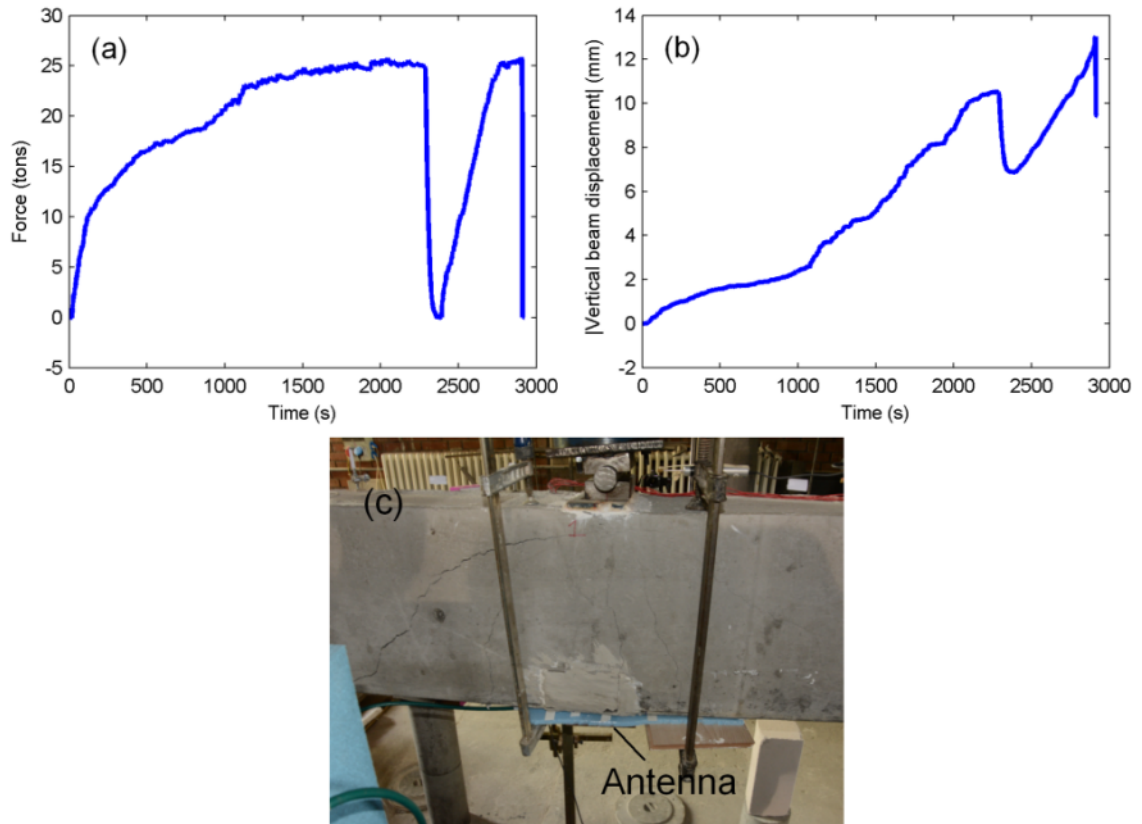


Figure 5.7: Plastic deformation region measurements: a) Applied vertical force read from the load cell, b) Absolute vertical displacement of the midpoint at the bottom of the beam (LVDT reading), c) The beam sample with visible cracks after the experiments. (Reprinted, with permission, from “A Wireless Passive Sensing System for Displacement/Strain Measurement in Reinforced Concrete Members” by B. Ozbey, V.B. Erturk, H.V. Demir, A. Altintas and O. Kurc, *Sensors*, under the Creative Commons Attribution License (<http://creativecommons.org/licenses/by/4.0/>).)

13 mm vertical displacement at the end of the experiment, whereas the beam deflected only around 0.4 mm in the elastic range experiments when 7 tons of force was applied. The post-experiment crack formation is also shown in Figure 5.7-c. The sensing system recorded data at every 3 seconds during the experiment. The shift of the filtered frequency peaks corresponding to NSRR #1 is shown in Figure 5.8-a. The strain data obtained from NSRR #1 is plotted in Figure 5.8-b, and compared to the strain gage data. At $t = 1128$ s, corresponding to 2450 microstrains, an immense increase is observed in strain due to yielding of the rebar and flexural cracks in the concrete at the middle of the beam, which forced the strain gages beyond their limit, eventually causing them to break down. Therefore, after that instant, the only information source left regarding the strain forming on the rebars was our wireless sensing system. Based on the very good agreement between the two results in the elastic deformation region and rebar tensile test performance of the sensing system, it can be assumed that the measurement of the NSRR sensor after the breakdown of the strain gages is also acceptable. Furthermore, the force-strain curve shown in Figure 5.8-c is consistent with the expectations, thus we can deduce that the readings are accurate. A maximum strain of 0.023 is measured at the instant of the highest force, corresponding to a 0.6 mm displacement on the rebar between the two attachment points. The dynamic range of the system was previously shown to be over 20 mm in Chapter 2, meaning that the system practically does not possess any limits regarding the maximum measurable strain or displacement. Hence, it is demonstrated that the system is sufficient for monitoring the reinforced concrete members until failure.

Due to the presence of concrete holding the rebar grid, the curve obtained in Figure 5.8-c is slightly different looking than a classic stress-strain curve of a steel rebar (see Figure 3.6). The reason for this is that the concrete hinders reaching higher levels of force and strain where the beam fails. In Figure 5.8-c, the elastic and plastic regions are clearly separated. However, since the level of the applied force cannot be increased to even higher values (unlike the tensile loading experiment) due to failure of the beam, a maximum of 23000 microstrains is measured on the rebar where NSRR #1 is attached. This prevents the initiation of the strain hardening region, which was observed to start when the applied

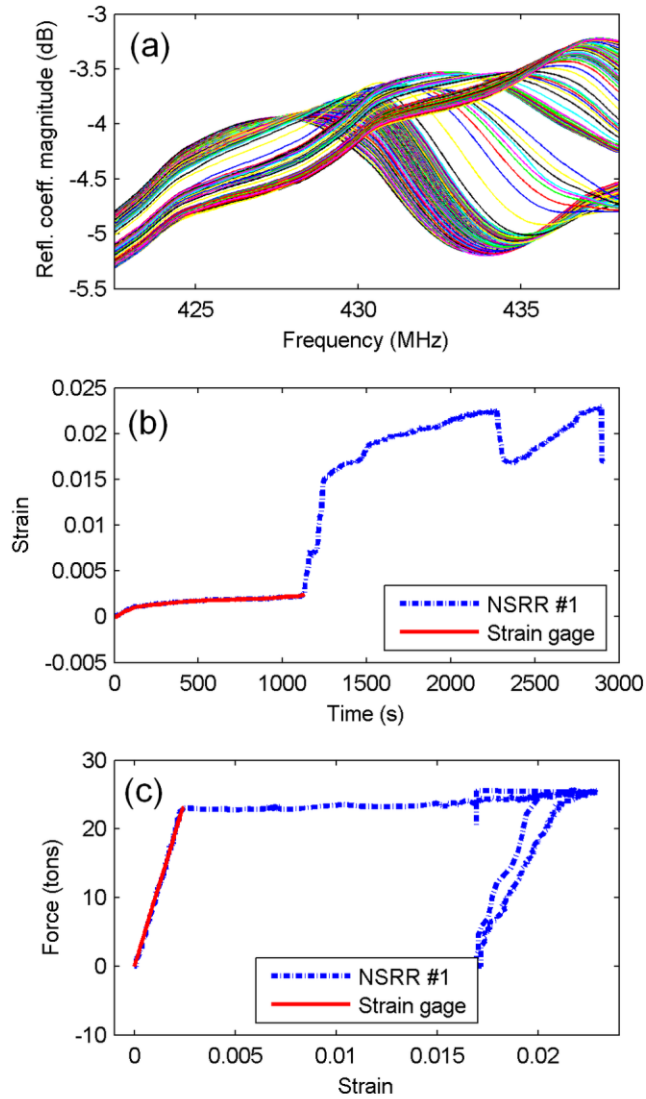


Figure 5.8: Plastic deformation region measurements: a) Shifting of NSRR #1 resonance peaks, b) Strain obtained by NSRR #1 plotted versus time, and compared to the data from the strain gages until the strain gages break down, c) The force-strain curve plotted with both NSRR #1 and strain gage data. (Reprinted, with permission, from “A Wireless Passive Sensing System for Displacement/Strain Measurement in Reinforced Concrete Members” by B. Ozbey, V.B. Erturk, H.V. Demir, A. Altintas and O. Kurc, *Sensors*, under the Creative Commons Attribution License (<http://creativecommons.org/licenses/by/4.0/>).)

force was increased past over 30000 microstrains in the previous tensile tests. Therefore, at the point where the plastic deformation experiment was terminated, the rebars were at the yielding phase, where the level of the applied force stays more or less the same while the strain induced on the rebars is increased. This can also be observed in Figure 5.7-a, where the force does not vary very much; and also in Figure 5.8-c, where the change of force is minimal while the strain increases from 2000 microstrains to over 20000 microstrains.

The results of NSRR #2 were also recorded during the experiment via the multi-point sensing property. However, due to a physical effect, an artificial resonance frequency change was observed during the yielding. Therefore, only the data for the first 1128 seconds are shown for NSRR #1 in Figure 5.9. When the plaster layer and the plexiglass protection cover were removed after the experiment, it was observed that a piece of concrete had come off and had been stuck between the two NSRR parts, leading to a big change in the capacitance, as shown in Figure 5.9-d. It can be observed in Figure 5.9 that the system operated thoroughly until this incident. Strong agreement between the NSRR probe and strain gage results prove that the laboratory calibration is also successful in transforming the frequency shift into strain.

Simply supported beam experiments constitute the final step for the sensing system to qualify as a device that is compatible with real-life applications. Therefore, the success of the experiments described throughout this chapter holds great importance. Through these experiments, important conclusions have been drawn regarding the sensing system. These conclusions are listed as follows:

- Data was recorded continuously in both elastic and plastic regions in a real-life scenario, and the readings of the sensing system were shown to match with those of the strain gages.
- Sensitivity is very critical in terms of SHM, especially in the elastic region. It was demonstrated that the sensing system has a sensitivity on microstrain-level, which is adequately sufficient for this purpose.
- For the plastic range, dynamic range of the system is also important. The

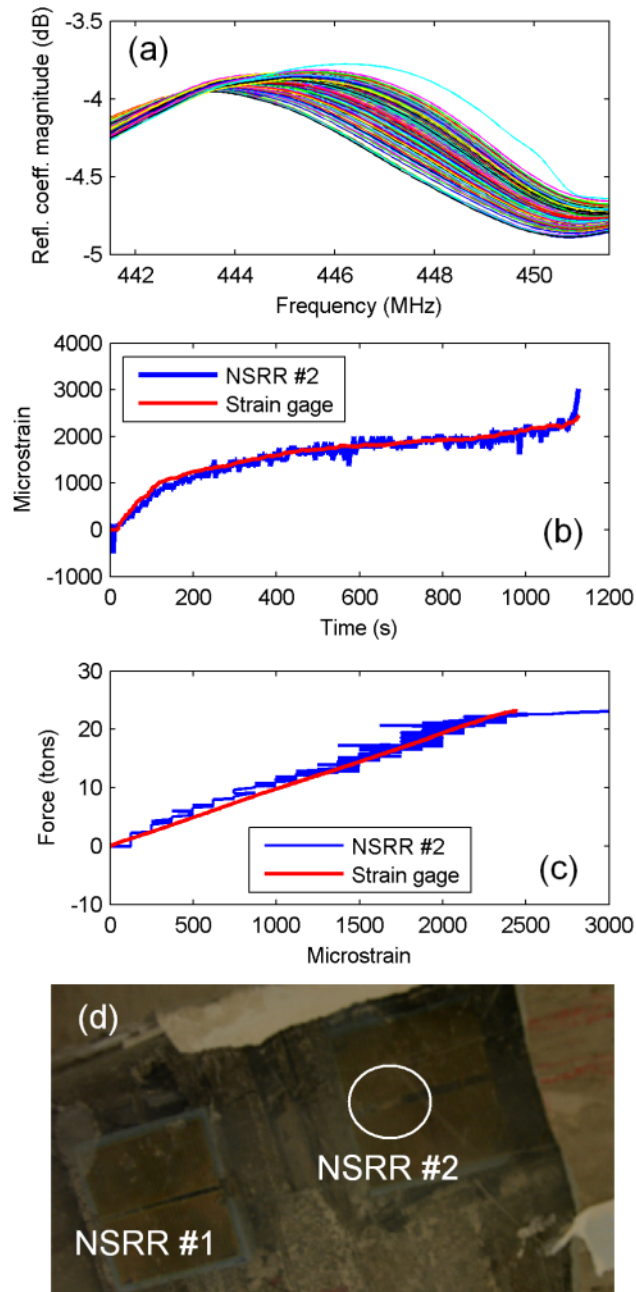


Figure 5.9: Plastic deformation region measurements: a) Shifting of NSRR #1 resonance peaks, b) Strain obtained by NSRR #1 plotted versus time, and compared to the data from the strain gages until the strain gages break down, c) The force-strain curve plotted with both NSRR #1 and strain gage data, d) The piece of concrete stuck in NSRR #2 during the experiment. (Reprinted, with permission, from “A Wireless Passive Sensing System for Displacement/Strain Measurement in Reinforced Concrete Members” by B. Ozbey, V.B. Erturk, H.V. Demir, A. Altintas and O. Kurc, Sensors, under the Creative Commons Attribution License (<http://creativecommons.org/licenses/by/4.0/>).)

system was shown to continue taking accurate measurements until the end of the experiment, much after the levels where strain gages broke and came off during yielding.

- The location of the antenna outside the beam is critical in order to have the laboratory calibration agree with the actual experiment setup results. The correct positioning of the antenna is obtained when a reflection coefficient behavior as close as possible to the one in laboratory measurements is observed. Therefore, before the measurements, one needs to make sure that this correct location of the antenna is determined and designated carefully for accuracy.
- The system has the capability of multi-point sensing, which means that it can acquire data simultaneously from multiple probes whose resonances are within the bandwidth of the antenna. This capability is utilized in the plastic deformation experiments, and data from two probes are recorded simultaneously.
- Although data can be acquired from both NSRR probe geometries, Design B, which is the smaller footprint sensor geometry, has a higher system noise. This can be attributed to the poor coupling between the antenna and the probe, and probably to the increasing effect of the clutter at that frequency.
- It was also shown that the sensing system can be used to record data at discrete times instead of continuous monitoring, and that the same calibration is also valid for this case.

Chapter 6

Multi-point Sensing by Multiple Probes

In Chapter 5, the multi-point sensing property of the sensing system was utilized for monitoring more than one NSRR probe at the same time by a single antenna. This is possible by assigning each probe in the sensor array to a different range of operating frequency through modification of their initial separation distances (d) and/or jumper lengths l . In this configuration, the bandwidth allocated for each probe determines the number of array elements as well as the dynamic range of the system while the illumination pattern of the antenna is effective in the coupling strength. In this chapter, the details of this property are explored through experiments.

The main idea behind multi-point sensing by a single antenna is to generate a coupling between the antenna and each of the NSRR probes in the array at the same time. As for the single-probe case, the antenna illuminates the array elements and also collects the scattered waves. Each NSRR probe is assigned a specific resonance frequency (f_{res}) and a frequency interval (Δf). Through these parameters, an electromagnetic channel is created between the antenna and each NSRR probe. Since these parameters are set in such a way that there are no intended spectral overlaps, a multi-point system is formed using only

a single antenna, where the antenna can acquire information from each sensor simultaneously in a single frequency sweep of the network analyzer. A conceptual diagram summarizing the working principle of the sensing system is illustrated in Figure 6.1.

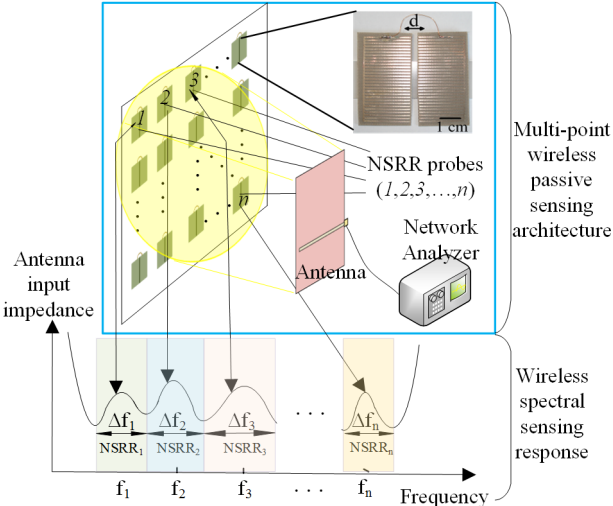


Figure 6.1: Concept of the proposed multi-point wireless passive architecture consisting of n nested split ring resonator (NSRR) probes and wireless spectral sensing response of each sensor shown on the frequency-antenna input impedance characteristics.

The response of each NSRR probe can directly be observed at the input impedance of the antenna due to the coupling created by the array elements and the antenna (as in the single-NSRR probe case). The strength and quality of this coupling are directly related with how well the antenna illuminates the NSRR probes. As previously shown multiple times in this dissertation, once an NSRR probe is electromagnetically in the sight of the antenna, it manifests itself as a local peak in the reflection coefficient of the antenna at the resonance frequency of that specific NSRR probe. As the sensed quantity is subject to a change, the frequency of this peak shifts due to the capacitance change at the NSRR probe.

6.1 Experimental validation

In order to demonstrate the simultaneous multi-point 2-D sensing, experiments were carried out. The setup for an experiment, where the number of array elements (n) is 3, is given as an inset in Figure 6.2. In the experiments, an array of modified NSRR probes was illuminated via the antenna. For separation of the frequency intervals corresponding to each sensor, the modification of initial edge-to-edge distances (d) between the two parts of each probe in the array was used. Each sensor incorporated a 0.1 mm-diameter jumper with a specific length (l), which was selected exactly as 3.5 cm for all probes. Three local frequency peaks corresponding to each NSRR probe can be observed at the reflection coefficient of the antenna due to coupling, as shown in Figure 6.2. Although each of the three NSRR probes is clearly distinguished in the form of a peak, the coupling strengths are observed to be different for each resonance. As explained in Chapter 2, this is a result of the variation of the coupling strength with the antenna illumination (see Figure 2.13). The probes that are positioned at the edges with respect to the antenna are relatively less well-illuminated, leading to worse distinguishability. The resonances which are closer to the limits of the antenna bandwidth may also have poorer coupling strength. On the other hand, once an NSRR-probe is seen by the antenna, it is also possible to track the shift of that peak which makes the sensing possible. Here, d is increased from specific starting points ($d_{0,1} = 1.5$ mm, $d_{0,2} = 2.5$ mm, $d_{0,3} = 3.8$ mm) to $d_{0,i} + 1$ mm ($i = 1, 2, 3$) via a controlled displacement setup by taking 10 measurement points. This results in a shift of approximately 8 MHz, 6 MHz and 6 MHz in the resonance frequency of the first, second and third peaks, respectively. The frequency shift versus the change in d (denoted as Δd) is shown in Figure 6.2-b. For the experiment, $D_m = 10$ cm.

As mentioned earlier, the separation of the resonance frequencies for the same NSRR geometry can be implemented by either assigning each sensor a different starting d , or a different jumper length, l . The experiment result showing the multi-point sensing by two NSRR probes having the jumper lengths of 4 cm and 5 cm is presented in Figure 6.3-a and the frequency shifts versus d are shown in Figure 6.3-b. Here, d_0 is 2.5 cm and the same for both NSRR probes, while

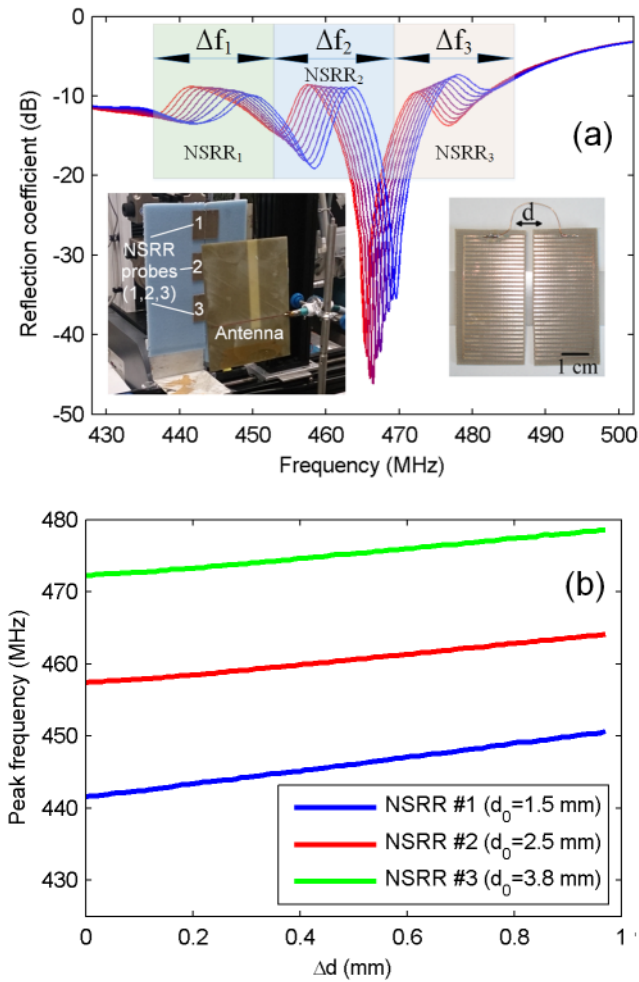


Figure 6.2: a) The shift of resonance frequency for each NSRR probe in the sensor array ($n = 3$) when d is increased from d_0 to $d_0 + 1$ mm. $D_m = 10$ cm. The resonance frequencies of the probes are determined by modification of d_0 . Left (inset): Experiment setup. Right (inset): Photograph of the NSRR probe employed in the experiment, b) The change of the resonance frequency versus the change in d for each probe.

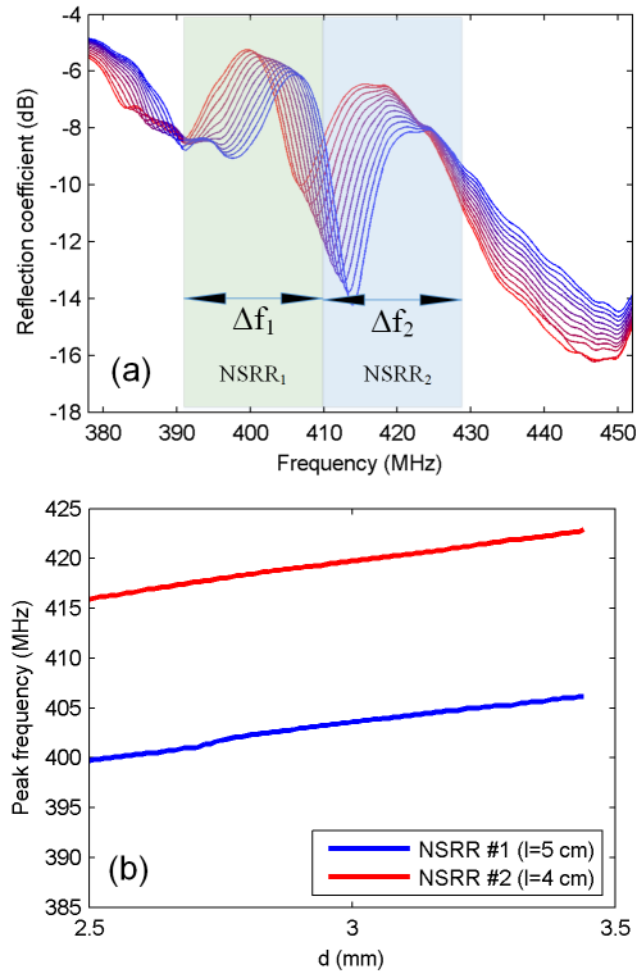


Figure 6.3: a) The shift of resonance frequency for each NSRR probe in the sensor array ($n = 2$) when d is increased from 2.5 to 3.5 mm. $D_m = 10$ cm. The resonance frequencies of the probes are determined by modification of l , where $l_1 = 5$ cm and $l_2 = 4$ cm, b) The change of the resonance frequency versus the change in d for each probe.

the modification of l by 1 cm is observed to shift the resonance frequency by around 15 MHz. Either of these two methods can be utilized for determining the resonance frequencies and the frequency shift intervals.

The idea of multi-point single-antenna sensing depends on allocating a pre-defined f_{res} and a Δf for each sensor. Along with the antenna bandwidth (BW), Δf is the factor that determines the dynamic range of each sensor and the number of sensors in the array. A theoretical limit on the maximum number of array elements n is then $n = \frac{BW}{\Delta f}$. An experiment result where n is 6 is shown in Figure 6.4-a. In this experiment, the NSRR sensors, whose frequencies are set by either modification of d or l , make their appearance as peaks, resulting in 6 different peaks at corresponding frequencies. The initial case is given in Figure 6.4-a (blue curve). Then, d of NSRR # 6 is increased slightly while other NSRR sensors remain untouched, causing the peak at the highest resonance frequency to shift right (red curve). Finally, d of NSRR # 1 is increased slightly while it remains the same for all other sensors (see the green curve). Here, the critical point is that d of the NSRR # 6 is not returned back to its original position shown in the blue curve, but instead, it remains in the position shown in the red curve where its d had slightly been increased. Therefore, in order to see the effect of changing d of NSRR # 1, the red and the green curves should be compared. This experiment shows that it is possible to apply multi-point sensing technique to an array where $n = 6$. Even higher number of sensors are also theoretically feasible. The limits of the system are tested with a full-wave simulation in CST Microwave Studio, where $n = 16$ and each sensor is assigned a d from 1 to 4 mm with 0.2 mm steps. In the simulations, the sensors are illuminated by a plane wave. The resulting peaks in the antenna reflection coefficient are shown in Figure 6.4-b. Then, d is increased by 100 μm at every sensor, resulting in a frequency shift, which can also be observed in Figure 6.4-b. Both the experiment result where $n = 6$ and the simulation result of a 4×4 array show that the multi-point sensing is applicable to higher number of sensors.

The main compromise of the system is between its spatial and spectral capacities. In order to have a higher resolution of the sensed quantity, one has to locate as many sensors as possible over the area to increase the spatial capacity,

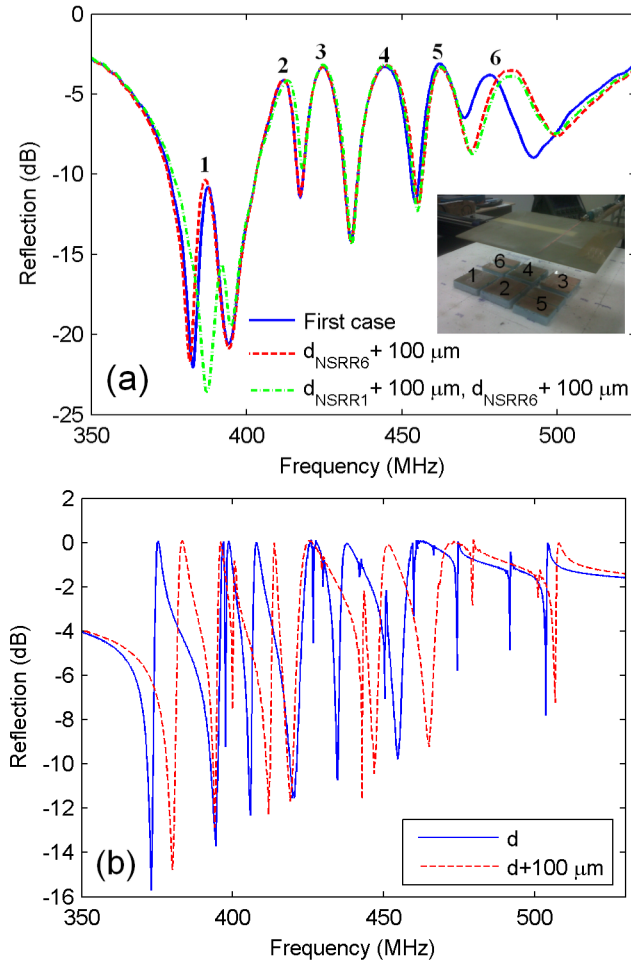


Figure 6.4: a) The result of an experiment where $n = 6$: Initial case is shown in blue, the case where d is slightly increased for NSRR # 6 is shown in red, and the case where d is slightly increased for NSRR # 1 is shown in green. All other d 's remain the same. The experiment setup is shown in the right bottom corner. b) Simulation results of a 4×4 array ($n = 16$) with d varying between 1 to 4 mm in 0.2 mm steps, and when d is increased by $100 \mu\text{m}$.

e.g. for determining the 2-D strain forming on the surface of a material. However, division of the available bandwidth to many intervals implies a narrow Δf for each sensor, which in essence determines the dynamic range of the system, or, the difference between the minimum and maximum strain values measurable by the system. Similarly, to increase the dynamic range, one has to give away from the resolution, which is determined by the number of sensors in the system. Apart from this trade-off, a point that needs to be improved in the system is D_m , which is the monitoring distance (distance between the sensors and the antenna), since until now, the proposed wireless sensing scheme has only been limited to the near-field of the antenna, which ensures a distance of a few tens of centimeters for the selected frequency range. This distance is proportional to the operating wavelength and is even lower for higher frequencies. However, an interesting configuration of the wireless multi-point sensing system is to employ sensors assigned to exactly the same frequency and to keep them close to each other at a distance with higher inter-coupling. Since it is known that increasing the monitoring distance (D_m) decreases the depth of the notch (or the coupling strength of the resonance) [71], the superposed responses from multiple sensors tuned to the same resonance frequency can be used to increase the distance between the antenna and the NSRR probes. This is enabled by a deeper notch due to the superimposed responses. In the experiments, it was observed that the placement of two NSRR probes tuned to the same frequency increased the coupling strength by around 1 dB.

6.2 Inter-coupling between the probes

A critical point regarding the array structures is the inter-coupling, which is the interaction between the array elements. This leads to a change in the total capacitance of the coupled system which in turn creates a shift of resonance frequency, adversely affecting the sensing characteristics described above. This inter-coupling, which is more dominant when the array elements are closer to each other, was also characterized by experiments. In these experiments, an NSRR probe was placed at a fixed position just across the point of the antenna

where the feedline and the slot of the antenna meet (the antenna was also kept stationary at a distance of 10 cm) while another probe was located at several changing positions along the left, right, bottom and top axes of the fixed probe. The edge-to-edge distances (D_c) between the stationary and moving probes were changed from 0 to 40 mm in four directions (upwards, downwards, rightwards and leftwards as shown in Figure 6.5-a).

The diagonal variation was skipped since it was observed that the diagonal placement of the NSRR probes with respect to each other has negligible impact on the coupled system resonance frequency. In this experimental procedure, the inter-coupling was identified by tracking the variation of the fixed NSRR probe resonance frequency due to the placement of the second NSRR probe in the vicinity of the fixed one. The experiment setup is shown in Figure 6.5-a. The absolute fractional change of fixed NSRR resonance frequency is shown in Figure 6.5-b and Figure 6.5-c for two different experiments, respectively. In the first experiment, the resonance frequencies of the two probes are set by changing the jumper length: The fixed NSRR probe has an l of 4 cm (corresponding to $f_{res} = 405$ MHz) and the NSRR probe which is moved along the top, bottom, right and left axes of the fixed probe, has an l of 8 cm. For both probes, $d = 0$. As for the second experiment, the resonance frequencies are set by changing the initial edge-to-edge distances: The fixed probe has a d_0 of 2 mm (corresponding to $f_{res} = 450$ MHz) while the moving probe has a d_0 of 0. For both probes, $l = 3.5$ cm. As expected, for both cases, the inter-coupling is observed as diminishing as the distance between the two NSRR probes is increased. In the worst case scenario of placing the two probes in a touching position, the maximum deviation from the standard resonance frequency is exhibited for the case when the moving probe is placed at the bottom of the stationary probe. This experiment is useful in the characterization of the effect of the position of the sensors on each other's resonance frequency. There are two options available to the designer: 1) To eliminate the inter-coupling as much as possible by keeping the array elements at a safe distance, e.g. a minimum distance of 20 mm can be selected as D_c , where the change of the resonance frequency due to the inter-coupling is as low as 0.1%, 2) To keep the array elements at a distance where the inter-coupling is still high,

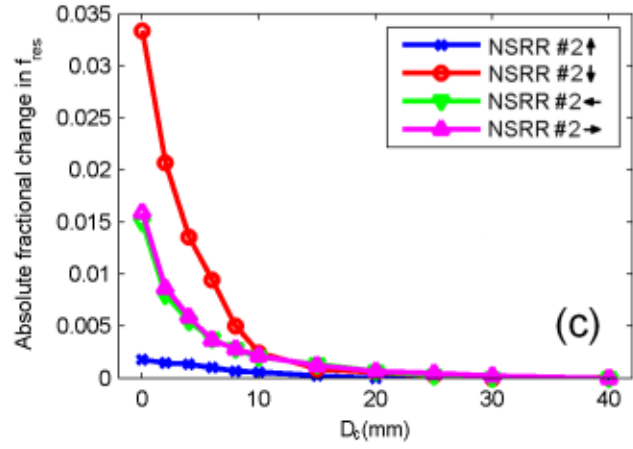
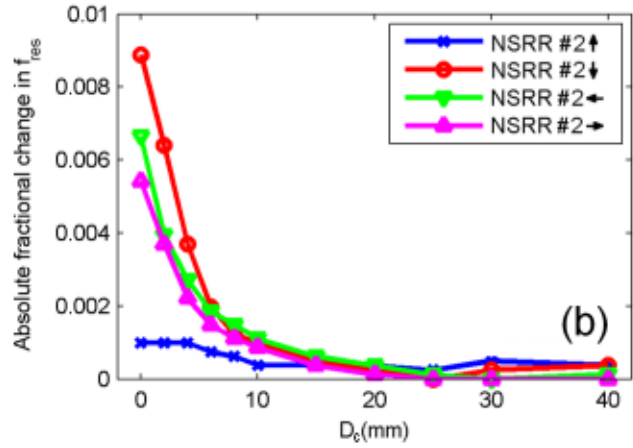
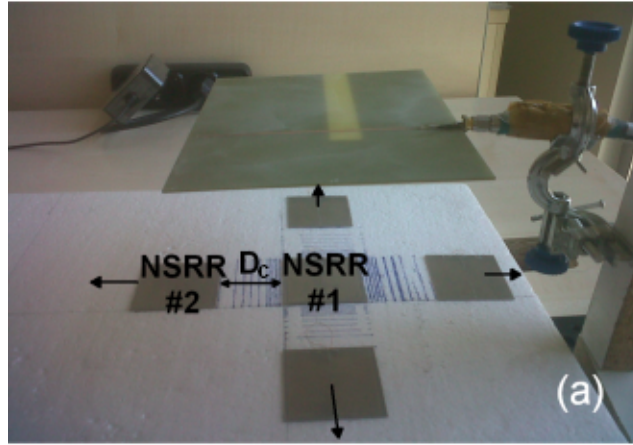


Figure 6.5: Experiments related to the inter-coupling in the sensing system where $n = 2$: a) Fractional variation in the resonance frequency of an NSRR probe ($l_1 = 4$ cm) when another probe ($l_2 = 8$ cm) is located at edge-to-edge distances (D_c) varying from 0 to 40 mm along top, bottom, right and left axes. $d = 0$ for both probes, b) Same experiment except the resonance frequencies are set by assigning the probes different d_0 's instead of different l 's. $d_1 = 2$ mm, $d_2 = 0$, and $l=3.5$ mm for both cases.

but to characterize the system accordingly, i.e., using the variation of the resonance frequency with the sensed quantity under conditions where inter-coupling is dominant. Both are valid options since it is observed by the experiments that the sensitivity of sensing is not affected by the inter-coupling.

A future application of the multi-point single-antenna sensing can be the extraction of the surface strain map of different types of industrial materials. These include composite materials such as airplane wings, helicopter blades or wind turbine blades. It is also a necessity in modern structural engineering for construction materials including concrete. This requires the use of many sensing probes in order to obtain a higher resolution. As discussed in the Introduction, most of the present technologies that monitor strain are only able to provide information about strain forming in one direction except very few which can only predict strain in two directions in addition to being wired and/or active. Large scale technologies such as wireless sensor networks which collect data from sensors located on several points, or fiber optical sensors which are embedded inside the composite materials, come with many problems that retain them from being widely used as standard methods for measuring the strain surface distribution. Therefore, such a passive sensing system where μm - and microstrain-level data from all of the sensors can be acquired wirelessly at a single measurement without any active transmitters, can be very beneficial for the aforementioned industrial areas.

Chapter 7

Equivalent Circuit Model of the NSRR

The nested split ring resonator structure has been exploited in many areas since it was first proposed by Melik et al. in [62], as discussed in the Introduction. Despite having superiority over the conventional SRR geometry in terms of sensitivity and compactness and being increasingly utilized in different application areas, an equivalent circuit model which can explain the operation of the NSRR has not been covered in literature. In this chapter, an equivalent circuit-based model is proposed for this structure. The proposed equivalent circuit model is adaptable to both the classical and the modified NSRR structures. The formulas of the model parameters are originated from known capacitance and inductance values of simple shapes such as a piece of planar transmission line or two parallel wires, which are combined here to come up with the working principle of the whole NSRR. The approach employed here is to treat the structure as a combination of strips and gaps between them rather than handling it as a combination of nested split-rings. The proposed model is able to adapt to the variation of different design parameters, with which the resonance frequency of the structure can be modified.

The physical parameters of the modified NSRR geometry are shown in Figure

7.1. As discussed at different sections throughout the dissertation, d and l represent the edge-to-edge distance between two mechanically independent parts of the structure, and the length of the thin wire used to electrically short the uppermost strip, respectively. Therefore, d and l are the two parameters which are used for changing the resonance frequency f_{res} of the whole NSRR structure even after its fabrication. N , D , w and l_s , denote the number of the parallel strip pairs (including the uppermost continuous strip), the gap between the adjacent strips, and the width and length of a strip, respectively. Especially N is important for determining f_{res} before the fabrication of the structure, while other parameters play roles in determination of the structure capacitances and inductances.

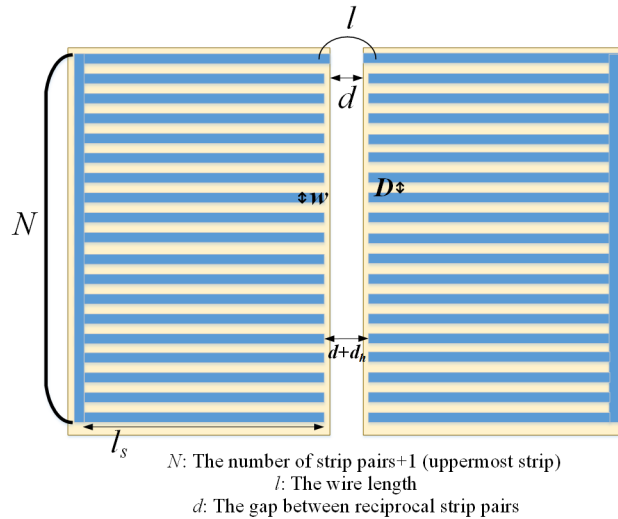


Figure 7.1: Nested split-ring resonator geometry modified for displacement sensing with design parameters.

7.1 Parameters of the model

The proposed equivalent circuit model for NSRR comprises N stages, each of which represents a opposing strip pair. It also comprises four different parameters, denoted as C_s , L_s , C_{gap} and L_{wire} . The circuit diagram of the model is shown in Figure 7.2. The details regarding the parameters of the model are given in the subsequent sections.

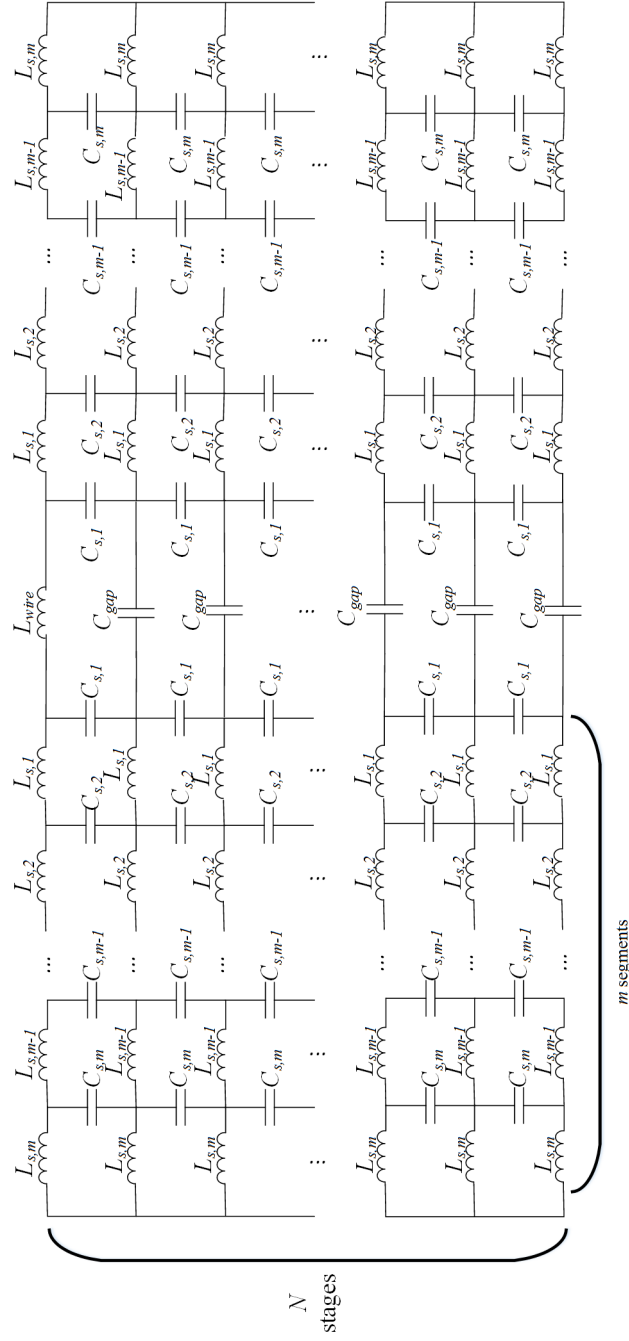


Figure 7.2: Parameters of the proposed equivalent model geometry for NSRRs.

7.1.1 Capacitance between two coplanar strips (C_s)

C_s is the capacitance between two coplanar parallel strips. Therefore, the number of C_s is $N - 1$ for each of the two mechanically separated NSRR parts. C_s , along with the inductance of each strip L_s , are divided into m segments as shown in Figure 7.2. The reason for this is the following: When C_s and L_s are considered as the parameters of a planar transmission line (such as a coplanar waveguide or coplanar stripline), it yields more accurate results to express them as distributed parameters instead of single lumped elements. The value of the capacitance of each segment from $C_{s,1}$ to $C_{s,m}$ is simply assumed to be equal, and is given by:

$$C_{s,1} = C_{s,2} = \dots = C_{s,m} = \frac{C_s}{m}.$$

Several approaches can be considered for the calculation of C_s . In this study, we will consider two of them. The first approach is to treat each parallel strip pair as a coplanar stripline, and then to find the line capacitance as C_s . The parallel strips are shorted from one side but this does not constitute a problem since a shorted coplanar waveguide or stripline can still be modeled as transmission line without a discontinuity [108]. A single-layer coplanar stripline illustration is shown in Figure 7.3.

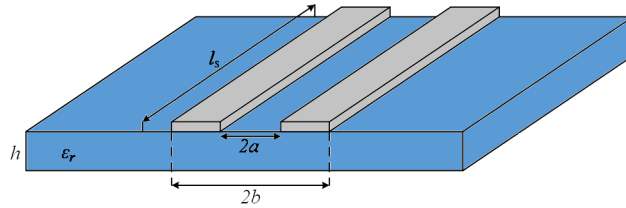


Figure 7.3: Parameters of a single-layer coplanar stripline shown on a schematic.

The per-unit-length capacitance of such a transmission line, $C_{s,cps}$, is given as [109, 110]

$$C_{s,cps} = \epsilon_{r,eff}^{cps} \epsilon_0 \frac{K(k)}{K(k')} \quad (7.1)$$

where $\epsilon_{r,eff}^{cps}$ is the effective relative permittivity of the coplanar stripline, ϵ_0 is the free-space permittivity, and K denotes the complete elliptical integral of the first

kind. The arguments k and k' are functions of the physical parameters of the line and are given as [109, 110]

$$k = \sqrt{1 - \left(\frac{a}{b}\right)^2} \quad (7.2)$$

and

$$k' = \sqrt{1 - k^2} = \frac{a}{b} \quad (7.3)$$

where a and b are the half of the inner and outer edge-to-edge distances of the two plate conductors of the coplanar stripline geometry, as shown in Figure 7.3. The effective relative permittivity of the coplanar stripline, $\epsilon_{r,eff}^{cps}$, is found as [109, 110]

$$\epsilon_{r,eff}^{cps} = 1 + \frac{1}{2} (\epsilon_r - 1) \frac{K(k)K(k'_1)}{K(k'_1)K(k_1)} \quad (7.4)$$

where ϵ_r is the relative permittivity of the substrate, and k_1 and k'_1 are defined as [109, 110]

$$k_1 = \sqrt{1 - \frac{\sinh^2(\pi a/2h)}{\sinh^2(\pi b/2h)}} \quad (7.5)$$

and

$$k'_1 = \sqrt{1 - k_1^2} \quad (7.6)$$

where h is the thickness of the substrate as shown in Figure 7.3. By comparing Figure 7.3 with Figure 7.1, one can deduce that in the formulas, $a = D/2$ and $b = (2w + D)/2$. For an NSRR design with parameters $w = 0.800$ mm, $D = 0.800$ mm, $h = 0.508$ mm, $l_s = 21.6$ mm and $\epsilon_r = 3.2$, $\epsilon_{r,eff}^{cps}$ is calculated as 1.67. Then the capacitance C_s is found as

$$C_s = C_{s,cps} l_s = 0.524 \text{ pF}. \quad (7.7)$$

The second approach for the calculation of C_s is using the capacitance formula of coplanar plates of finite width and length and infinitesimal thickness. The formula is given in [111] for the free-space as

$$C_s = l_s \epsilon_0 \frac{K(k'_2)}{K(k_2)} \quad (7.8)$$

where the arguments k_2 and k'_2 are defined as

$$k_2 = \frac{1}{1 + 2w/D} \quad (7.9)$$

and

$$k_2' = \sqrt{1 - k_2^2} \quad (7.10)$$

where w and D are the strip width and the edge-to-edge gap between two coplanar strips, respectively, as shown in Figure 7.1. When we use (7.8), for our case, it is assumed that $l_s \gg w$. In addition, ϵ_0 is replaced with an effective relative permittivity due to the presence of the substrate. Thus, for the effective relative permittivity, $\epsilon_{r,eff}^{cps}$ for coplanar stripline can be used. In this situation, for the aforementioned design parameters, by taking $\epsilon_{r,eff}^{cps} = 1.67$, C_s is also calculated as 0.524 pF. Therefore, both approaches are found to be reliable for the calculation of the capacitance between two coplanar strips, C_s .

7.1.2 Average inductance of a strip (L_s)

L_s is the total average inductance of each one of the strips. Similar to C_s , L_s is also divided into m segments as shown in Figure 7.2 in order to make the model more distributed and hence, more accurate. The inductance of each segment from $L_{s,1}$ to $L_{s,m}$ is also assumed to be equal, and is given by:

$$L_{s,1} = L_{s,2} = \dots = L_{s,m} = \frac{L_s}{m}. \quad (7.11)$$

Unlike C_s , L_s is expressed as the addition of these components. One of them is the self inductance of each strip, $L_{s,self}$. The effect of the average mutual inductances coming from the strips parallel to a particular strip is considered as the second component, and denoted as M . Finally, the strips opposing to a particular strip is the third one, and is denoted as M_r . L_s as M and M_r , respectively. The calculation methods of each for these components are described below.

$L_{s,self}$ is the self inductance of a strip. For finding $L_{s,self}$, the flat wire or ribbon inductance formula can be utilized, and is given in [108, 112] as

$$L_{s,self} = 2l_s \left[\ln \left(\frac{2l_s}{w+t} \right) + 0.5 + 0.2235 \left(\frac{w}{l_s} \right) \right] \text{ (nH)} \quad (7.12)$$

where t is the metal thickness and can be ignored in our study due to the fact that the operation frequency is too low to include its effect. The other two parameters l_s and w are shown on Figure 7.1.

For each strip, the total mutual inductance of the strips parallel to it should also be reflected on L_s . One way to do it is to use the formula of mutual inductance between two parallel wires given by [112]

$$M(g) = 2l_s \left[\ln \left(\frac{2l_s}{g} \right) - 1 + \frac{g}{l_s} \right] \text{ (nH)}. \quad (7.13)$$

In Equation (7.13), g is the inner edge-to-edge distance between the wires. In order to calculate M for a strip, the mutual inductances coming from each parallel strip should be added by setting $g = D, 3D, 5D, \dots$. The reason for this can be explained as follows: The inner edge-to-edge distance between two adjacent parallel strips is given by D whereas the inner edge-to-edge distance between second adjacent strips is given by $D + w + D$. However, in the NSRR design, w is generally set equal to D . Thus, $D + w + D = 3D$, $D + w + D + w + D = 5D$, and so on. Therefore, the total mutual inductance can be calculated by using the formula given in (7.13) with a changing g for the contribution of each strip. On the other hand, one should also consider the magnetic fields that cancel each other on the NSRR structure. In Figure 7.4, the calculation of the total M is shown for $N = 4, 5, 6$. If a current of I is assumed to be induced at every strip excluding the uppermost continuous strip, the magnetic fields due to I 's from symmetric up and down strips cancel each other for a specific strip. For instance, in Figure 7.4, for $N = 3$, M_2 , the mutual inductance at the center strip, is zero due to cancellation of fields. However, for M_1 and M_3 , contributions from the strips which are D and $3D$ away are included. The total mutual inductance, M_{total} is then the sum of M_1 , M_2 and M_3 divided by 2, to avoid including the same mutual inductance twice. This reasoning is valid for any N , but for odd N , zero M is not produced for any strip. The formulation of M for even and odd N

is as follows:

$$\begin{aligned} \text{Odd } N : M_{total} &= \sum_{k=3}^{\frac{N+3}{2}} (k-2)M[(2k-5)D] \\ &+ \sum_{k=\frac{N+5}{2}}^N (N-k+1)M[(2k-5)D] \end{aligned} \quad (7.14)$$

$$\begin{aligned} \text{Even } N : M_{total} &= \sum_{k=3}^{\frac{N}{2}+1} (k-2)M[(2k-5)D] \\ &+ \sum_{k=\frac{N}{2}+2}^N (N-k+1)M[(2k-5)D] \end{aligned} \quad (7.15)$$

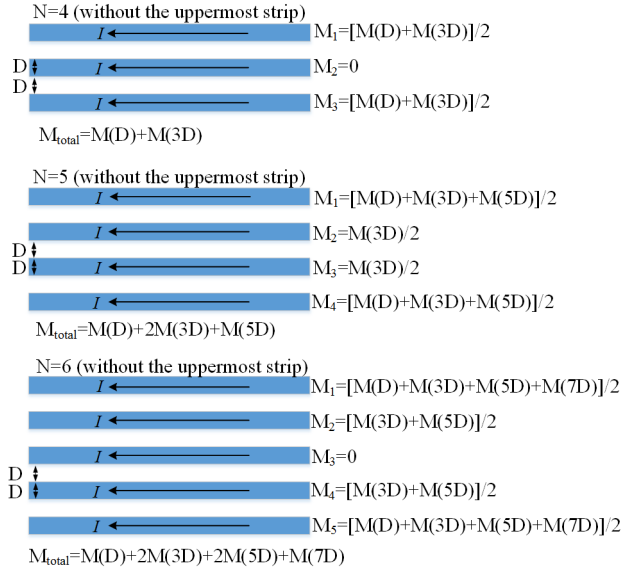


Figure 7.4: Calculation of the mutual inductance M_{total} between parallel strips for $N = 4, 5, 6$.

In this formulation, the contribution of the uppermost strip on mutual inductance is excluded. Since it is a continuous structure, the current at the uppermost strip flows at an opposite direction to the other strips, and its magnitude is different. Hence, it distorts the homogeneity of the overall structure. Since the contribution from a single strip is not very much effective on the total mutual inductance, in order to keep the homogeneity, the effect of the uppermost strip

on mutual inductance is ignored. In the formulation, M_{total} gives the sum of all mutual inductances from all strips. However, the effect of M_{total} has to be squeezed inside a single strip via L_s in the equivalent circuit model. In order to reflect it on L_s as an average value, it is assumed that M_{total} is distributed to every strip equally, and thus should be divided by N :

$$M = \frac{M_{total}}{N}. \quad (7.16)$$

M_r is the mutual inductance of each strip with all opposing strips, i.e., the strips which stay on the other mechanically separated NSRR part. M_r should also be reflected on L_s as M . For the calculation of M_r , the formula for the mutual inductance between two parallel wires that do not overlap, whose geometry is shown in Figure 7.5, can be used.

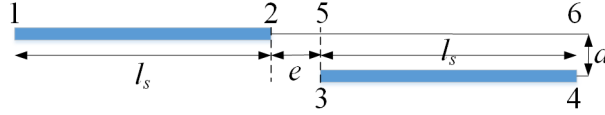


Figure 7.5: Geometry for calculating the mutual inductance between two parallel wire segments.

Adaptation of the parallel wire system to the NSRR requires one to set $e = d + d_h$, and $a = w + D$ for a coplanar opposite strip pair shown in Figure 7.5. The reason why e is not exactly equal to d is the following: For the original NSRR structure, where the wire length l is 0, only the uppermost strip is continuous while there is a slight gap between each opposing coplanar strip. If we call this gap as d_h , it is seen that $e = d + d_h$ (see Figure 7.1). Additionally, when the contributions from all the opposing strips are considered, it can be understood that a takes the values of $2D$, $4D$, $6D$, \dots , again considering $w = D$ by design. The mutual inductance for the system shown in Figure 7.5 is given as [112]

$$M_r = 0.503 \left[l_s \ln \left(\frac{R_{1,46}}{R_{1,35}} \right) + l_s \ln \left(\frac{R_{1,46}}{R_{2,35}} \right) + e \ln \left(\frac{R_{1,46} R_{2,35}}{R_{1,36} R_{2,46}} \right) \right] - (r_{14} - r_{13} + r_{23} - r_{24}) \quad (7.17)$$

where

$$R_{k,nm} = \frac{r_{kn} + r_{km}}{r_{kn} - r_{km}}$$

where

$$\begin{aligned}
r_{13} &= \sqrt{a^2 + (l_s + e)^2} \\
r_{14} &= \sqrt{a^2 + (2l_s + e)^2} \\
r_{15} &= l_s + e \\
r_{16} &= 2l_s + e \\
r_{23} &= \sqrt{a^2 + e^2} \\
r_{24} &= \sqrt{a^2 + (l_s + e)^2} \\
r_{25} &= e \\
r_{26} &= l_s + e.
\end{aligned}$$

For the calculation of $M_{r,total}$, the mutual inductance of a strip with all opposing strips should be added in a similar fashion to the calculation of M_{total} . For every strip pair, Equation (7.17) should be used with the proper a . The calculation of $M_{r,total}$ is described in Figure 7.6 for $N = 3, 4, 5$. The contribution from the uppermost strip is not included since it is continuous and does not have a gap with the opposing strips. Also, the mutual inductance of a strip with the directly opposing one is zero since the magnetic field is zero along the axis of the strip. The cancellation of fields again takes place for even N for the middle strip excluding the uppermost strip. The formulation of M_r for odd and even N is given by

$$\begin{aligned}
\text{Odd } N : M_{r,total} &= \sum_{k=3}^{\frac{N+3}{2}} (k-2)M_r[(2k-4)D] \\
&+ \sum_{k=\frac{N+5}{2}}^N (N-k+1)M_r[(2k-4)D] \quad (7.18)
\end{aligned}$$

$$\begin{aligned}
\text{Even } N : M_{r,total} &= \sum_{k=3}^{\frac{N}{2}+1} (k-2)M_r[(2k-4)D] \\
&+ \sum_{k=\frac{N}{2}+2}^N (N-k+1)M_r[(2k-4)D] \quad (7.19)
\end{aligned}$$

$M_{r,total}$ gives the sum of all mutual inductances from the opposing strips. By the same reasoning for M_{total} , in order to reflect $M_{r,total}$ on L_s , which is the

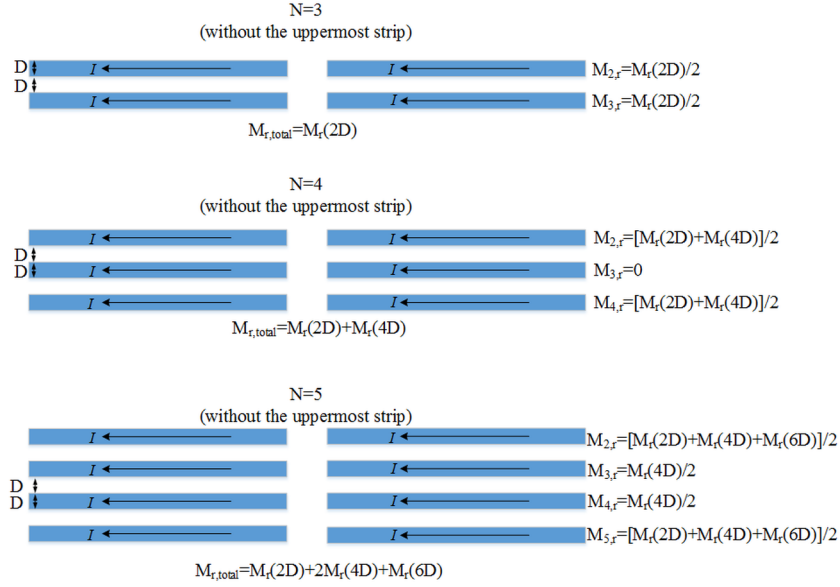


Figure 7.6: Calculation of the mutual inductance $M_{r,total}$ between opposing strips for several N values.

inductance of a single strip, $M_{r,total}$ should be divided by N :

$$M_r = \frac{M_{r,total}}{N}. \quad (7.20)$$

After calculation of the self inductance of each strip and the mutual inductances coming from the parallel and opposing strips, the average inductance reflected on L_s can be written as:

$$L_s = L_{s,self} + M + M_r. \quad (7.21)$$

For the application of displacement sensing, e changes with a mechanical effect causing a relative displacement in that direction, hence M_r and L_s become dependent on d .

7.1.3 Capacitance between a coplanar opposing strip pair (C_{gap})

C_{gap} is the capacitance between a coplanar opposing strip pair. Hence, the number of C_{gap} in the model is $N - 1$. Again, different approaches can be taken for finding C_{gap} . The best one seems to be modeling the opposing strip pair as a very short

piece of thick coplanar stripline, where w is the length of the line, $2a = d + d_h$ and $2b = 2l_s + d + d_h$ when the notation in Figure 7.3 is employed. Then, C_{gap} is given by

$$C_{gap} = \epsilon_{r,eff}^{cps} \epsilon_0 \frac{K(k)}{K(k')} w \quad (7.22)$$

where

$$k = \sqrt{1 - \left(\frac{d + d_h}{2l_s + d + d_h} \right)^2} \quad (7.23)$$

and

$$k' = \sqrt{1 - k^2} = \frac{d + d_h}{2l_s + d + d_h}. \quad (7.24)$$

The effective relative permittivity of the coplanar stripline, $\epsilon_{r,eff}^{cps}$, is again taken as 1.67 for the set of physical parameters mentioned before. Similar to M_r , C_{gap} is also a function of d . For the application of displacement sensing, the effect of the decrease of C_{gap} becomes dominant and leads to an increase in f_{res} .

7.1.4 Inductance of the thin jumper wire (L_{wire})

The uppermost strip is continuous in NSRR geometry, and this can be achieved via a thin jumper wire when the whole structure is symmetrically split into two halves. As previously mentioned, another function of this shorting wire is to help tuning f_{res} by assigning different values for l , the wire length. L_{wire} does not exist when the structure is not split into two parts, and it can be replaced by just a short. In literature, there are several variations of the formula for the self inductance of a thin wire, but all these formulas yield approximately the same result. Here, the wire inductance is found as [113]

$$L_{wire} = 2l \left[\ln \left(\frac{2l}{r_w} \right) - \frac{3}{4} \right] \text{ (nH)} \quad (7.25)$$

where r_w is the radius of the wire. L_{wire} is shown for several values of l in Table 7.1 for $r_w = 0.100$ mm.

The equivalent model parameter values for Design A are given in Table 7.2. The physical dimensions of Design A are as follows: $w = 0.800$ mm, $D = 0.800$

Table 7.1: The change of L_{wire} with l ($r_w = 0.1$ mm)

l (cm)	1.00	3.00	5.00	7.00	9.00
L_{wire} (nH)	9.10	33.9	61.6	90.9	121

mm, $l_s = 21.6$ mm, $h = 0.508$ mm and $\epsilon_r = 3.2$ (Design A). These dimensions are also given in Table 7.2. The model parameters presented in Table 7.2 are for six different N values from 5 to 29, as well as for $d = 0$ and $d = 5$ mm. It should be noted that C_s , C_{gap} and L_{self} are independent of N , whereas the mutual inductances M and M_r change with N . C_{gap} and M_r are the only two parameters that are functions of d . Only L_{wire} is a function of l , but it is not included in Table 7.2 since l is taken as 0. In addition, the change of L_s with N , calculated for the same set of physical dimensions, is shown in Figure 7.7. It can be observed in the figure that the change of L_s takes a linear fashion after a certain N value.

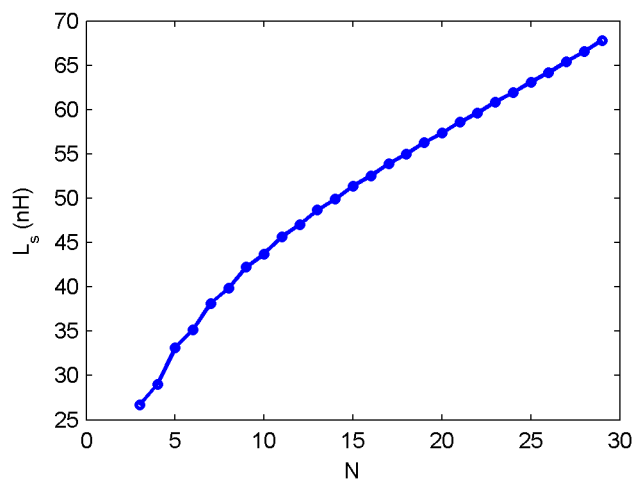


Figure 7.7: The change of average strip inductance L_s with the number of strips N .

Table 7.2: Equivalent model parameter values for different N and d computed for Design A, where $w = 0.800$ mm, $D = 0.800$ mm, $l_s = 21.6$ mm, $h = 0.508$ mm, and $\epsilon_r = 3.2$ (all capacitances are in pF; all inductances are in nH; d in mm).

N	C_s	$C_{gap}(d=0)$	$C_{gap}(d=5)$	$L_{s,self}$	M	$M_r(d=0)$	$M_r(d=5)$	$L_s(d=0)$	$L_s(d=5)$
5	0.524	0.0431	0.0283	19.3	9.90	6.41	5.18	35.7	34.4
10	0.524	0.0431	0.0283	19.3	13.7	12.7	11.1	45.7	44.1
15	0.524	0.0431	0.0283	19.3	16.2	17.3	15.6	52.9	51.2
20	0.524	0.0431	0.0283	19.3	19.0	20.6	18.8	58.9	57.1
25	0.524	0.0431	0.0283	19.3	22.3	23.0	21.0	64.7	62.6
29	0.524	0.0431	0.0283	19.3	25.7	24.5	21.9	69.5	66.9

7.2 Comparison with experiments and simulations

Simulations of the equivalent circuit model were carried out in Ansoft Designer. In the simulations, two high-impedance ports were defined at either side of the circuit. In such a setup, the frequency of resonance (f_{res}) can be determined by observing the transmission characteristics, i.e., tracking the position of the dip frequency of the magnitude of S_{21} (the frequency where the phase crosses 0° can also be used for this purpose). Typical S_{21} magnitude and phase plots are shown in Figure 7.8 for the case of $N = 29$, $d = 0$ and $l = 0$. It can be observed that $f_{res} = 440$ MHz for that particular case.

The variation of f_{res} for every N from 3 to 29 were compared with full-wave simulations carried out in CST Microwave Studio for $d = 0$ and $l = 0$. The specifications of the NSRR used in the simulation are as in Table 7.2: $w = 0.800$ mm, $D = 0.800$ mm, $l_s = 21.6$ mm, $h = 0.508$ mm and $\epsilon_r = 3.2$. The number of line segments, m , was taken as 10. The results are shown in Figure 7.9. Figure 7.9 demonstrates that there is a correlation between the full-wave simulation and the proposed model. The discrepancy is observed to be higher for lower N values but the slopes of the decreasing frequency for both cases agree well as N is increased. The measurement and full-wave simulation results are compared with those of the equivalent model in Figure 7.10 for two different N values: $N = 10$ and $N = 29$. In the plots, the sensing parameter d is varied and the change of f_{res} with d is investigated. l is chosen as 4 cm. For these two cases, NSRRs were fabricated with the set of aforementioned physical dimensions given in Table 7.2. In order to excite the NSRRs, single-slot microstrip antennas designed to work at the resonance frequency of each NSRR were used. In full-wave simulations, the full system setup was simulated including the antenna. In both measurements and simulations, f_{res} is recorded and compared with the result obtained from the proposed equivalent circuit model. As shown before, the resonance of the NSRR can be observed in the form of a peak at the reflection coefficient of the antenna whereas the frequency of this peak may be slightly different than the actual

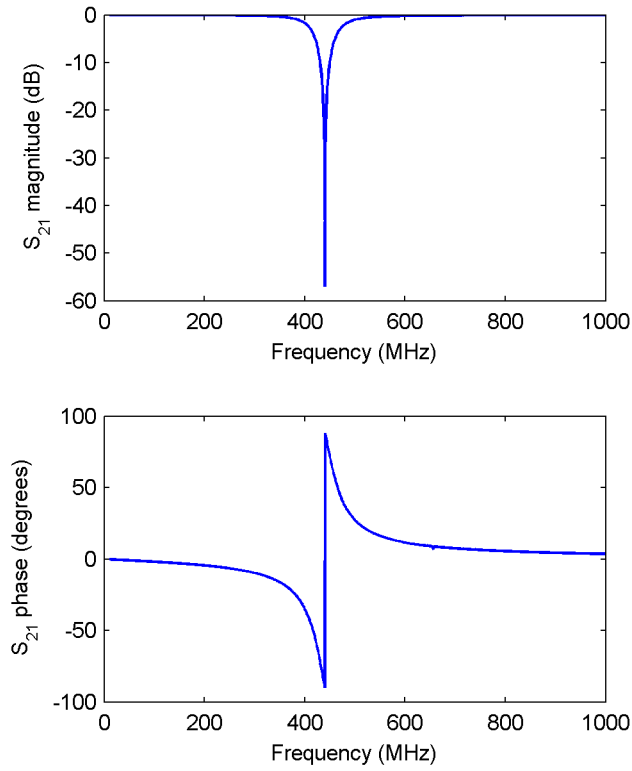


Figure 7.8: A typical transmission spectrum plot obtained via the proposed equivalent model, where the magnitude and phase of S_{21} are shown. Here, $N = 29$, $d = 0$ and $l = 0$.

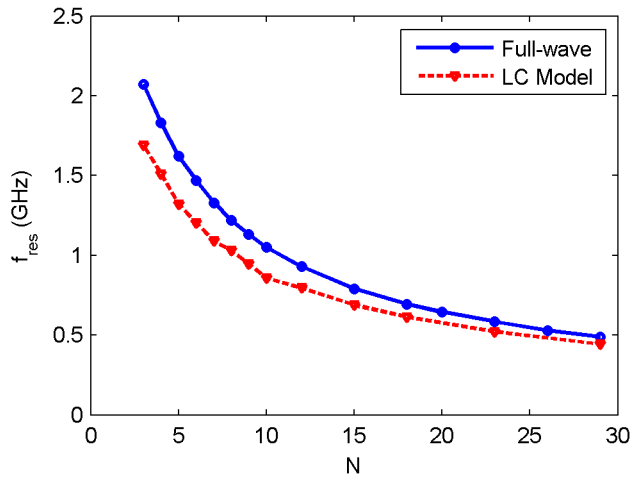


Figure 7.9: The change of f_{res} with N , shown for both equivalent model and full-wave simulations. Here, $d = 0$ and $l = 0$.

NSRR resonance frequency due to the coupling (see Figure 2.16). However, an examination of Figure 7.10 reveals that the results are in agreement for both $N = 10$ and $N = 29$. The agreement of the results of the model with those of the measurement and the simulation is observed to be better for $N = 29$ since the frequency shift for $N = 10$ is higher than the measurement and full-wave simulation.

The change of f_{res} with the tuning parameter l is also of interest for the modified NSRR geometry. In the experiments performed to characterize this change, the shorting wire length was changed from 2 to 9 cm whilst d was kept constant at 4 mm. The measurement results are compared with those of the equivalent model in Figure 7.11 again for $N = 10$ and $N = 29$, where the physical dimensions given in Table 7.2 were used in fabrication. The measurement and the model are observed to be in perfect agreement for $N = 29$. For $N = 10$, the coherence of model and measurement results can still be considered reasonable in terms of the percentage error. The slopes of the curves are observed to be very close for the full-wave and equivalent circuit model results, and the differences in the measurement can be attributed to imperfections at the experiment setup, such as the lack of a perfect coplanarity of the two NSRR parts. When $N = 29$, with the used set of physical dimensions, a square-shaped structure is obtained. However, for $N = 10$, the result is a flat shaped structure. This makes the latter structure more prone to the disruptive effects of the misalignments in the experiment.

The adaptability of the proposed model to the change in physical dimensions such as the width or length of each strip is examined in Figure 7.12. In the top graph, the change of f_{res} with the strip width, w , is shown. D , the gap between each width is also taken equal to w and is automatically changed. In the bottom graph, the effect of the change of the strip length, l_t , is displayed. In both simulations, $N = 29$, while d and l are 0. In Figure 7.12, it can be observed that the model is not as successful in adapting to the changes in w or D as it is in adapting to l_s .

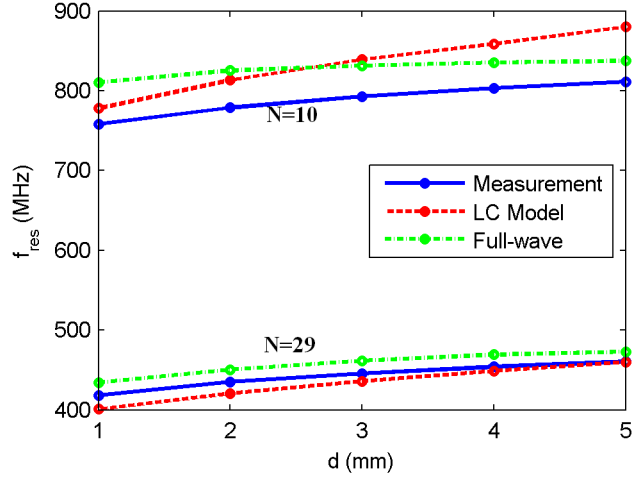


Figure 7.10: Change of resonance frequency, f_{res} , with displacement between the opposing strips, d , that is obtained from the equivalent circuit model, is compared to measurement and full-wave simulation. $l = 4$ cm for simulations and measurement.

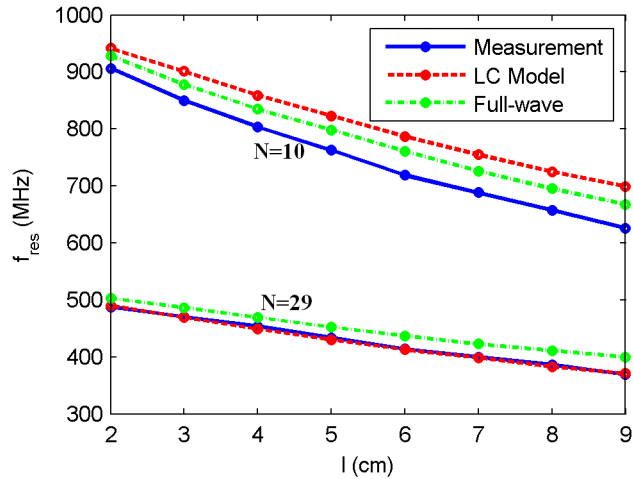


Figure 7.11: Change of resonance frequency, f_{res} , with shorting wire length, l , that is obtained from the equivalent circuit model, compared to measurement and full-wave simulation. $d = 4$ mm for simulations and measurement.

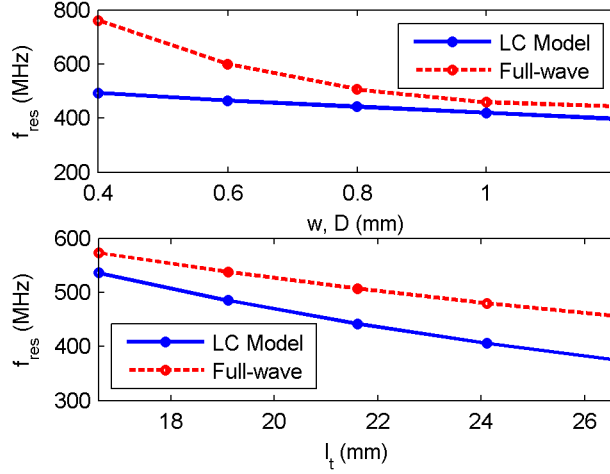


Figure 7.12: Change of resonance frequency, f_{res} , with physical NSRR parameters, w , D and l_t , that is obtained from the equivalent circuit model, compared to full-wave simulation ($N = 29$, $d = 0$, and $l = 0$).

The results of the equivalent circuit model are observed to be generally agreeing with the full-wave simulations and measurements, demonstrating that the approach to the problem is correct in essence. The discrepancies can be enhanced by derivation of exact formulas used for certain model parameters instead of employing approximate formulas available in the literature. Through modification of parameters and employing the suitable formulas, the approach embraced here can be adapted to other types of planar metamaterial-inspired structures, mainly other variants of split-ring resonators.

Chapter 8

Conclusions

In this study, a novel, wireless and passive displacement/strain sensing system is proposed. The system incorporates a modified nested split-ring resonator probe geometry and a transceiver antenna. The electromagnetic coupling between these structures yields an enhanced sensitivity and resolution along with a wide dynamic range, compared to similar sensors in literature. The sensing system is able to track displacement/strain at both the elastic and plastic deformation regions of steel, which enables it to be used successfully for both structural health monitoring and post-earthquake damage assessment. The effects of the complex medium constituted by the combination of the steel rebar grid and concrete on sensing are also studied. Understanding these effects is important for real-life applications, which has not been studied actively until now for wireless sensors. Based on the experimental procedure carried out for the realization of the effects of several scenarios of complex media, the most destructive scenario is observed to be the case when a concrete block (either reinforced or unreinforced) is placed immediately behind the NSRR probe, e.g., in a touching position. For this scenario, the local resonance peak corresponding to the NSRR probe observed through the antenna is lost, which makes the sensing impossible. A possible remedy is to attach a 1-cm thick separator made of polystyrene foam to two mechanically separated NSRR probe parts. This way, the sensing system is able to function thoroughly in the simply supported beam experiments, where the NSRR probes are

attached onto different rebars of a grid inside a beam, and the antenna monitors the frequency shift from outside the beam. The curve which is used for calibration/transformation of measured frequency shift into displacement, is vital for an accurate measurement. This d - f curve is obtained at a controlled displacement setup via an xyz -translation stage, and a numerical fit based on an exponential-type function is used for conversion into displacement. However, parameters of this fit become subject to a change as the medium in which the measurements are performed changes electromagnetically. An accurate characterization of these changes is important for a correct conversion. A future improvement of the operation of the sensing system is increasing the monitoring distance without giving away from the sensitivity and resolution. With this purpose, several methods can be chosen, but it should be mentioned that the strong coupling between the NSRR probe and the antenna is observed to stem from a near-field interaction. Therefore, methods such as employing a radio transceiver system by placing an active external transmitter just outside the beam may imply a reduced sensitivity/resolution. Using other antenna types or changing the NSRR probe geometry may increase D_m , but this increase should not be expected to be very significant as well. A possible method for an increased D_m is to adopt energy harvesting, where the NSRR probe geometry can be in a semi-passive structure which powers up by converting the RF signal into DC bias current, and uses the internal transmitter to reflect back the signal. Another approach is to limit the effect of the clutter which acts as noise on the backscattered NSRR probe signal. For this, a method based on frequency doubling can be employed, where a nonlinear element (such as a diode) integrated on the NSRR probe creates a second or third harmonic, and the shift of this harmonic can be tracked instead of the original resonance frequency peak by another antenna. On the other hand, it should be mentioned that the power of the harmonics are very much reduced compared to the original signal, and this may cause a problem in detection and tracking.

In this dissertation, we also propose multi-point sensing by multiple probes and a single antenna, where each probe in the sensor array is assigned a resonance frequency and a non-overlapping spectral interval for frequency shift (frequency shift range). It is shown that the antenna is capable of capturing the responses

from all probes by a single frequency sweep. This approach is employed in the simply supported beam experiment both in the elastic and the plastic region experiments, where the antenna monitors two NSRR probes simultaneously. The characterization of the undesired inter-coupling between the array elements is also important and studied. A future application where this high sensitivity and resolution multi-point single-antenna sensing scheme can be exploited is the two-dimensional surface strain mapping of industrial materials for early diagnosis of damage/deformation before it actually happens.

Finally, we propose an equivalent lumped circuit model for the NSRR geometry. The model is tested for accuracy via comparison to full wave simulations as well as measurements for two different strip pair numbers, and a good matching is obtained between the results. The model is observed to be valid for both the original (unseparated) and modified (separated) NSRR structures. It is also observed to work for any number of strip pairs. On the other hand, since the formulas used for the inductance and capacitance of the structures of the model (strips, gaps, a thin wire, etc.) are not exact but only approximate, the model has room for improvement.

Appendix A

Coefficient of determination (R^2)

In order to assign a numerical value to linearity of a curve, a parameter called the coefficient of determination, or, R^2 can be used. R^2 is a statistical parameter which shows the deviation of an actual curve from a fitted linear curve. If a linear curve is fit to a set of observed data points, and if we name each of those data points as y_i , the corresponding fitted value as \hat{y}_i , and the mean of the observed data as \bar{y} , then SSR, SST and R^2 can be defined as below:

$$\begin{aligned} \text{SSR} &= \sum_i (\hat{y}_i - \bar{y})^2, \\ \text{SST} &= \sum_i (y_i - \bar{y})^2, \\ R^2 &= \frac{\text{SSR}}{\text{SST}}. \end{aligned}$$

Bibliography

- [1] Y. Ikemoto, S. Suzuki, H. Okamoto, H. Murakami, X. Lin, H. Itoh, and H. Asama, “Force sensor system for structural health monitoring using passive RFID tags for structural health monitoring,” in *2nd IEEE International Interdisciplinary Conference on Portable Information Devices, 2008 and the 2008 7th IEEE Conference on Polymers and Adhesives in Microelectronics and Photonics. PORTABLE-POLYTRONIC 2008*, pp. 1–6, Aug. 2008.
- [2] C. Occhiuzzi, C. Paggi, and G. Marrocco, “Passive RFID strain-sensor based on meander-line antennas,” *IEEE Trans. Antennas Propag.*, vol. 59, pp. 4836–4840, Dec. 2011.
- [3] C. Paggi, C. Occhiuzzi, and G. Marrocco, “Sub-millimeter displacement sensing by passive UHF RFID antennas,” *IEEE Trans. Antennas Propag.*, vol. 62, pp. 905–912, Feb. 2014.
- [4] X. Yi, T. Wu, Y. Wang, and M. M. Tentzeris, “Sensitivity modeling of an RFID-based strain-sensing antenna with dielectric constant change,” *IEEE Sensors J.*, vol. 15, pp. 6147–6155, Nov. 2015.
- [5] X. Yi, C. Cho, J. Cooper, Y. Wang, M. M. Tentzeris, and R. T. Leon, “Passive wireless antenna sensor for strain and crack sensing-electromagnetic modeling, simulation, and testing,” *Smart Mater. Struct.*, vol. 22, p. 085009, Aug. 2013.
- [6] B. Cook, R. Vyas, S. Kim, T. Thai, T. Le, A. Traille, H. Aubert, and M. Tentzeris, “RFID-based sensors for zero-power autonomous wireless sensor networks,” *IEEE Sensors J.*, vol. 14, pp. 2419–2431, Aug. 2014.

- [7] J. Humphries and D. Malocha, "Passive, wireless SAW OFC strain sensor," in *Frequency Control Symposium (FCS), 2012 IEEE International*, pp. 1–6, May 2012.
- [8] W. Wilson, M. Rogge, B. Fisher, D. Malocha, and G. Atkinson, "Fastener failure detection using a surface acoustic wave strain sensor," *IEEE Sensors J.*, vol. 12, pp. 1993–2000, June 2012.
- [9] Bao, Zhongqing, M. Hara, M. Mitsui, K. Sano, S. Nagasawa, and H. Kuwano, "Experimental study of highly sensitive sensor using a surface acoustic wave resonator for wireless strain detection," *Jpn. J. Appl. Phys.*, vol. 51, p. 07GC23, July 2012.
- [10] O. Focke, M. Salas, A. S. Herrmann, and W. Lang, "Inductive Wireless Sensor- Actuator Node for Structural Health Monitoring of Fiber Reinforced Polymers by means of Lamb-waves," in *Sensors and Smart Structures Technologies for Civil, Mechanical, and Aerospace Systems 2015*, vol. 9435, p. 94352V, Bellingham: Spie-Int Soc Optical Engineering, 2015.
- [11] W.-E. Bulst, G. Fischerauer, and L. Reindl, "State of the art in wireless sensing with surface acoustic waves," *IEEE Trans. Ind. Electron.*, vol. 48, pp. 265–271, Apr. 2001.
- [12] A. Pohl, "A review of wireless SAW sensors," *IEEE Trans. Ultrason., Ferroelect., Freq. Control*, vol. 47, pp. 317–332, Mar. 2000.
- [13] A. Daliri, A. Galehdar, S. John, C. H. Wang, W. S. T. Rowe, and K. Ghorbani, "Wireless strain measurement using circular microstrip patch antennas," *Sensor. Actuat. A-Phys.*, vol. 184, pp. 86–92, Sept. 2012.
- [14] U. Tata, H. Huang, R. L. Carter, and J. C. Chiao, "Exploiting a patch antenna for strain measurements," *Meas. Sci. Technol.*, vol. 20, p. 015201, Jan. 2009.
- [15] T. Rai, P. Dantes, B. Bahreyni, and W. Kim, "A stretchable RF antenna with silver nanowires," *IEEE Electron Device Lett.*, vol. 34, pp. 544–546, Apr. 2013.

- [16] T. T. Thai, H. Aubert, P. Pons, G. DeJean, M. M. Tentzeris, and R. Plana, “Novel design of a highly sensitive RF strain transducer for passive and remote sensing in two dimensions,” *IEEE Trans. Microw. Theory Tech.*, vol. 61, pp. 1385–1396, Mar. 2013.
- [17] T. Huber, B. Bergmair, C. Vogler, F. Bruckner, G. Hrkac, and D. Suess, “Magnetoelastic resonance sensor for remote strain measurements,” *Appl. Phys. Lett.*, vol. 101, p. 042402, July 2012.
- [18] V. Pepakayala, S. Green, and Y. Gianchandani, “Passive wireless strain sensors using microfabricated magnetoelastic beam elements,” *Journal of Microelectromechanical Systems*, vol. 23, pp. 1374–1382, Dec. 2014.
- [19] S. Cheng and Z. Wu, “A microfluidic, reversibly stretchable, large-area wireless strain sensor,” *Adv. Funct. Mater.*, vol. 21, pp. 2282–2290, June 2011.
- [20] F. Gattiker, F. Umbrecht, J. Neuenschwander, U. Sennhauser, and C. Hierold, “Novel ultrasound read-out for a wireless implantable passive strain sensor (WIPSS),” *Sensor. Actuat. A-Phys.*, vol. 145-146, pp. 291–298, July 2008.
- [21] H. Lee, G. Shaker, V. Lakafosis, R. Vyas, T. Thai, S. Kim, X. Yi, Y. Wang, and M. Tentzeris, “Antenna-based ”smart skin” sensors for sustainable, wireless sensor networks,” in *2012 IEEE International Conference on Industrial Technology (ICIT)*, pp. 189–193, Mar. 2012.
- [22] Y. Li, W. Li, and Q. Ye, “A Compact UWB Antenna With Dual Band-Notch Characteristics Using Nested Split Ring Resonator and Stepped Impedance Resonator,” *Microw. Opt. Technol. Lett.*, vol. 55, pp. 2827–2830, Dec. 2013.
- [23] D. Wu, N. Fang, C. Sun, X. Zhang, W. J. Padilla, D. N. Basov, D. R. Smith, and S. Schultz, “Terahertz plasmonic high pass filter,” *Appl. Phys. Lett.*, vol. 83, pp. 201–203, July 2003.

- [24] D. J. Thomson, D. Card, and G. E. Bridges, “RF cavity passive wireless sensors with time-domain gating-based interrogation for SHM of civil structures,” *IEEE Sensors J.*, vol. 9, pp. 1430–1438, Nov. 2009.
- [25] D. G. Watters, P. Jayaweera, and A. J. Bahr, “Design and performance of wireless sensors for structural health monitoring,” in *Review of Progress in Quantitative Nondestructive Evaluation, Vols 21a & B* (D. O. Thompson and D. E. Chimenti, eds.), vol. 615, pp. 969–976, Melville: Amer Inst Physics, 2002. WOS:000177511400127.
- [26] J. C. Butler, A. J. Vigliotti, F. W. Verdi, and S. M. Walsh, “Wireless, passive, resonant-circuit, inductively coupled, inductive strain sensor,” *Sensor. Actuat. A-Phys.*, vol. 102, pp. 61–66, Dec. 2002.
- [27] S. Deshmukh and H. Huang, “Wireless interrogation of passive antenna sensors,” *Meas. Sci. Technol.*, vol. 21, Jan. 2010.
- [28] A. Mita and S. Takhira, “A smart sensor using mechanical memory for structural health monitoring of a damage-controlled building,” *Smart Mater. Struct.*, vol. 12, no. 2, 2003.
- [29] Y. Jia, K. Sun, F. J. A. Agosto, and M. T. Quinones, “Design and characterization of a passive wireless strain sensor,” *Meas. Sci. Technol.*, vol. 17, Sept. 2006.
- [30] A. K. Horestani, C. Fumeaux, S. Al-Sarawi, and D. Abbott, “Displacement sensor based on diamond-shaped tapered split ring resonator,” *IEEE Sensors J.*, vol. 13, pp. 1153–1160, Apr. 2013.
- [31] M. Hasani, A. Vena, L. Sydänheimo, L. Ukkonen, and M. M. Tentzeris, “Implementation of a dual-interrogation-mode embroidered RFID-enabled strain sensor,” *IEEE Antennas Wireless Propag. Lett.*, vol. 12, pp. 1272–1275, Oct. 2013.
- [32] A. Vena, K. Koski, E. Moradi, A. A. Babar, L. Sydänheimo, L. Ukkonen, and M. M. Tentzeris, “An embroidered two-dimensional chipless strain sensor for wireless structural deformation monitoring,” *IEEE Sensors J.*, vol. 13, pp. 4627–4637, Dec. 2013.

- [33] A. K. Horestani, J. Naqui, Z. Shaterian, D. Abbott, C. Fumeaux, and F. Martín, “Two-dimensional alignment and displacement sensor based on movable broadside-coupled split ring resonators,” *Sensor. Actuat. A-Phys.*, vol. 210, pp. 18–24, Apr. 2014.
- [34] H.-S. Yoon, S.-h. Kim, M.-H. Kim, D. Jung, J.-H. Kim, H.-J. Kim, and H.-S. Lee, “Wireless piezoelectric strain sensing measurement using a frequency modulation technique,” *J. Intell. Mater. Syst. Struct.*, vol. 26, pp. 1103–1109, June 2015.
- [35] C. Cho, X. Yi, Y. Wang, and M. M. Tentzeris, “Multi-physics modeling and simulation of a frequency doubling antenna sensor for passive wireless strain sensing,” *Structural Health Monitoring 2015: System Reliability for Verification and Implementation, Vols. 1 and 2*, pp. 864–872, 2015.
- [36] A. Deivasigamani, A. Daliri, C. H. Wang, and S. John, “A review of passive wireless sensors for structural health monitoring,” *Modern Applied Science*, vol. 7, Jan. 2013.
- [37] J. M. Lee and Y. Hwang, “A novel online rotor condition monitoring system using fiber Bragg grating (FBG) sensors and a rotary optical coupler,” *Meas. Sci. Technol.*, vol. 19, p. 065303, June 2008.
- [38] R. Matsuzaki, A. Todoroki, and K. Takahashi, “Time-synchronized wireless strain and damage measurements at multiple locations in CFRP laminate using oscillating frequency changes and spectral analysis,” *Smart Mater. Struct.*, vol. 17, p. 055001, Oct. 2008.
- [39] S. Park, T. Park, and K. Han, “Real-time monitoring of composite wind turbine blades using fiber Bragg grating sensors,” *Advanced Composite Materials*, vol. 20, pp. 39–51, Jan. 2011.
- [40] K. Schroeder, W. Ecke, J. Apitz, E. Lembke, and G. Lenschow, “A fibre Bragg grating sensor system monitors operational load in a wind turbine rotor blade,” *Meas. Sci. Technol.*, vol. 17, p. 1167, May 2006.

- [41] L. Bger, M. H. G. Wichmann, L. O. Meyer, and K. Schulte, “Load and health monitoring in glass fibre reinforced composites with an electrically conductive nanocomposite epoxy matrix,” *Composites Science and Technology*, vol. 68, pp. 1886–1894, June 2008.
- [42] T. J. Arsenault, A. Achuthan, P. Marzocca, C. Grappasonni, and G. Coppotelli, “Development of a FBG based distributed strain sensor system for wind turbine structural health monitoring,” *Smart Mater. Struct.*, vol. 22, p. 075027, July 2013.
- [43] P. Procházka and F. Vaněk, “Contactless diagnostics of turbine blade vibration and damage,” *J. Phys.: Conf. Ser.*, vol. 305, p. 012116, July 2011.
- [44] M. Luczak, B. Peeters, and K. Dziedziech, “Static and dynamic testing of the full scale helicopter rotor blades,” in *PROCEEDINGS OF ISMA2010 INCLUDING USD2010*, (Leuven, Belgium), pp. 2131–2143, Sept. 2010.
- [45] K. E. Robison, S. E. Watkins, J. Nicholas, K. Chandrashekhara, and J. L. Rovey, “Instrumented composite turbine blade for health monitoring,” in *Proceedings of the SPIE*, vol. 8347, pp. 83472J–83472J–9, 2012.
- [46] L. Glavind, I. S. Olesen, B. F. Skipper, and M. Kristensen, “Fiber-optical grating sensors for wind turbine blades: A review,” *Opt. Eng.*, vol. 52, no. 3, pp. 030901–030901, 2013.
- [47] D. C. Seo and J. J. Lee, “Effect of embedded optical fiber sensors on transverse crack spacing of smart composite structures,” *Composite Structures*, vol. 32, no. 1-4, pp. 51–58, 1995.
- [48] D. C. Lee, J. J. Lee, and S. J. Yun, “The mechanical characteristics of smart composite structures with embedded optical fiber sensors,” *Composite Structures*, vol. 32, no. 1-4, pp. 39–50, 1995.
- [49] A. Todoroki, Y. Tanaka, and Y. Shimamura, “Delamination monitoring of graphite/epoxy laminated composite plate of electric resistance change method,” *Composites Science and Technology*, vol. 62, pp. 1151–1160, July 2002.

- [50] A. Todoroki and Y. Tanaka, “Delamination identification of cross-ply graphite/epoxy composite beams using electric resistance change method,” *Composites Science and Technology*, vol. 62, pp. 629–639, Apr. 2002.
- [51] R. Matsuzaki, M. Melnykowycz, and A. Todoroki, “Antenna/sensor multifunctional composites for the wireless detection of damage,” *Composites Science and Technology*, vol. 69, pp. 2507–2513, Dec. 2009.
- [52] A. Todoroki, H. Kurokawa, Y. Mizutani, R. Matsuzaki, and T. Yasuoka, “Self-sensing time domain reflectometry method for damage monitoring of a CFRP plate using a narrow-strip transmission line,” *Composites Part B: Engineering*, vol. 58, pp. 59–65, Mar. 2014.
- [53] A. Sanchez Ramirez, R. Loendersloot, and T. Tinga, “Helicopter rotor blade monitoring using autonomous wireless sensor network,” in *Key Engineering Materials* (B. Basu, ed.), vol. 569-570, (Krakow, Poland), pp. 775–782, The British Institute of Non-Destructive Testing, 2013.
- [54] M. Kurata, X. Li, K. Fujita, and M. Yamaguchi, “Piezoelectric dynamic strain monitoring for detecting local seismic damage in steel buildings,” *Smart Mater. Struct.*, vol. 22, p. 115002, Nov. 2013.
- [55] J.-W. Park, S.-H. Sim, and H.-J. Jung, “Wireless displacement sensing system for bridges using multi-sensor fusion,” *Smart Mater. Struct.*, vol. 23, p. 045022, Apr. 2014.
- [56] Z. Qiu, J. Wu, and S. Yuan, “A wireless sensor network design and evaluation for large structural strain field monitoring,” *Meas. Sci. Technol.*, vol. 22, p. 075205, July 2011.
- [57] T. Torfs, T. Sterken, S. Brebels, J. Santana, R. van den Hoven, V. Spiering, N. Bertsch, D. Trapani, and D. Zonta, “Low power wireless sensor network for building monitoring,” *IEEE Sensors J.*, vol. 13, pp. 909–915, Mar. 2013.
- [58] A. Sanchez Ramirez, K. Das, R. Loendersloot, T. Tinga, and P. Havinga, “Wireless sensor network for helicopter rotor blade vibration monitoring: Requirements definition and technological aspects,” *Key Engineering Materials*, vol. 569-570, pp. 775–782, July 2013.

- [59] M. Eltoweissy, A. Wadaa, S. Olariu, and L. Wilson, "Group key management scheme for large-scale sensor networks," *Ad Hoc Networks*, vol. 3, pp. 668–688, Sept. 2005.
- [60] H.-J. Lee and J.-G. Yook, "Biosensing using split-ring resonators at microwave regime," *Appl. Phys. Lett.*, vol. 92, p. 254103, June 2008.
- [61] I. A. I. Al-Naib, C. Jansen, and M. Koch, "Thin-film sensing with planar asymmetric metamaterial resonators," *Appl. Phys. Lett.*, vol. 93, p. 083507, Aug. 2008.
- [62] R. Melik, E. Unal, N. K. Perkgoz, B. Santoni, D. Kamstock, C. Puttlitz, and H. V. Demir, "Nested metamaterials for wireless strain sensing," *IEEE J. Sel. Topics Quantum Electron.*, vol. 16, pp. 450–458, Mar. 2010.
- [63] R. Melik, E. Unal, N. K. Perkgoz, C. Puttlitz, and H. V. Demir, "Flexible metamaterials for wireless strain sensing," *Appl. Phys. Lett.*, vol. 95, p. 181105, Nov. 2009.
- [64] R. Melik, E. Unal, N. K. Perkgoz, C. Puttlitz, and H. V. Demir, "Metamaterial-based wireless strain sensors," *Appl. Phys. Lett.*, vol. 95, p. 011106, July 2009.
- [65] R. Melik, E. Unal, N. K. Perkgoz, C. Puttlitz, and H. Demir, "Metamaterial-based wireless RF-MEMS strain sensors," in *2010 IEEE Sensors*, pp. 2173–2176, Nov. 2010.
- [66] R. Melik, E. Unal, N. K. Perkgoz, C. Puttlitz, and H. V. Demir, "Metamaterial based telemetric strain sensing in different materials," *Opt. Express*, vol. 18, pp. 5000–5007, Feb. 2010.
- [67] C. Mandel, B. Kubina, M. Schubler, and R. Jakoby, "Passive chipless wireless sensor for two-dimensional displacement measurement," in *Microwave Conference (EuMC), 2011 41st European*, pp. 79–82, Oct. 2011.
- [68] S.-D. Jang, B.-W. Kang, and J. Kim, "Frequency selective surface based passive wireless sensor for structural health monitoring," *Smart Mater. Struct.*, vol. 22, no. 2, 2013.

- [69] T. Chen, S. Li, and H. Sun, “Metamaterials application in sensing,” *Sensors*, vol. 12, pp. 2742–2765, Feb. 2012.
- [70] H. Ertuğrul, “Wireless radio frequency sensors for structural health monitoring,” Master’s thesis, Department of Electrical and Electronics Engineering, Bilkent University, Ankara, Turkey, 2011.
- [71] B. Ozbey, E. Unal, H. Ertugrul, O. Kurc, C. M. Puttlitz, V. B. Erturk, A. Altintas, and H. V. Demir, “Wireless displacement sensing enabled by metamaterial probes for remote structural health monitoring,” *Sensors*, vol. 14, pp. 1691–1704, Jan. 2014.
- [72] B. Ozbey, H. V. Demir, O. Kurc, V. B. Erturk, and A. Altintas, “Wireless measurement of elastic and plastic deformation by a metamaterial-based sensor,” *Sensors*, vol. 14, pp. 19609–19621, Oct. 2014.
- [73] B. Ozbey, H. Demir, O. Kurc, V. Erturk, and A. Altintas, “Wireless sensing in complex electromagnetic media: Construction materials and structural monitoring,” *IEEE Sensors J.*, vol. 15, pp. 5545–5554, Oct. 2015.
- [74] B. Ozbey, V. B. Erturk, H. V. Demir, A. Altintas, and O. Kurc, “A Wireless Passive Sensing System for Displacement/Strain Measurement in Reinforced Concrete Members,” *Sensors*, vol. 16, p. 496, Apr. 2016.
- [75] W. Withayachumnankul, K. Jaruwongrungse, C. Fumeaux, and D. Abbott, “Metamaterial-inspired multichannel thin-film sensor,” *IEEE Sensors J.*, vol. 12, no. 5, pp. 1455–1458, 2012.
- [76] M. Puentes, M. Maasch, M. Schussler, and R. Jakoby, “Frequency multiplexed 2-dimensional sensor array based on split-ring resonators for organic tissue analysis,” *IEEE Trans. Microw. Theory Tech.*, vol. 60, pp. 1720–1727, June 2012.
- [77] X. Xu and H. Huang, “Multiplexing passive wireless antenna sensors for multi-site crack detection and monitoring,” *Smart Mater. Struct.*, vol. 21, no. 1, p. 015004, 2012.

- [78] S. Naoui, L. Latrach, and A. Gharsallah, “Nested metamaterials antenna for RFID traceability,” *Microw. Opt. Technol. Lett.*, vol. 56, pp. 1622–1626, July 2014.
- [79] V. T. Kilic, V. B. Erturk, and H. V. Demir, “Optical antenna of comb-shaped split ring architecture for increased field localization in NIR and MIR,” *Opt. Express*, vol. 21, p. 29455, Dec. 2013.
- [80] Y. Liu, N. Xie, X. Tang, and F. Xiao, “A compact low-phase noise oscillator with superior harmonic suppression characteristics based on novel nested split-ring resonator (NSRR),” *Int. J. Microw. Wirel T.*, vol. 9, pp. 1–7, Sept. 2015.
- [81] Y. Liu, X. Tang, Z. X. Zhang, and X. L. Huang, “Novel nested split-ring-resonator (SRR) for compact filter application,” *Prog. Electromagn. Res.*, vol. 136, pp. 765–773, 2013.
- [82] X.-J. He, L. Qiu, Y. Wang, Z.-X. Geng, J.-M. Wang, and T.-l. Gui, “A compact thin-film sensor based on nested split-ring-resonator (SRR) metamaterials for microwave applications,” *J. Infrared, Millimeter, Terahertz Waves*, vol. 32, pp. 902–913, July 2011.
- [83] R. Marqués, F. Medina, and R. Rafii-El-Idrissi, “Role of bianisotropy in negative permeability and left-handed metamaterials,” *Phys. Rev. B*, vol. 65, p. 144440, Apr. 2002.
- [84] G. Eleftheriades, O. Siddiqui, and A. Iyer, “Transmission line models for negative refractive index media and associated implementations without excess resonators,” *IEEE Microw. Wireless Compon. Lett.*, vol. 13, pp. 51–53, Feb. 2003.
- [85] H. Chen, L. Ran, J. Huangfu, T. M. Grzegorzcyk, and J. A. Kong, “Equivalent circuit model for left-handed metamaterials,” *J. Appl. Phys.*, vol. 100, p. 024915, July 2006.
- [86] L. Rogla, J. Carbonell, and V. Boria, “Study of equivalent circuits for open-ring and split-ring resonators in coplanar waveguide technology,” *IET Microw. Antenna. P.*, vol. 1, pp. 170–176, Feb. 2007.

- [87] T. D. Corrigan, P. W. Kolb, A. B. Sushkov, H. D. Drew, D. C. Schmadel, and R. J. Phaneuf, "Optical plasmonic resonances in split-ring resonator structures: An improved LC model," *Opt. Express*, vol. 16, pp. 19850–19864, Nov. 2008.
- [88] H. Bahrami, M. Hakkak, and A. Pirhadi, "Analysis and design of highly compact bandpass waveguide filter utilizing complementary split ring resonators (CSRR)," *Prog. Electromagn. Res.*, vol. 80, pp. 107–122, 2008.
- [89] S. Li, H.-W. Zhang, Q.-Y. Wen, Y.-S. Xie, D.-B. Tian, and Y.-X. Li, "Improved TL-RLC model for terahertz circular split-ring resonators," *Appl. Phys. A: Mater. Sci. Process.*, vol. 100, pp. 461–466, May 2010.
- [90] O. Abu Safia, L. Talbi, and K. Hettak, "A New Type of Transmission Line-Based Metamaterial Resonator and Its Implementation in Original Applications," *IEEE Trans. Magn.*, vol. 49, pp. 968–973, Mar. 2013.
- [91] A. Ebrahimi, W. Withayachumnankul, S. F. Al-Sarawi, and D. Abbott, "Dual-mode behavior of the complementary electric-LC resonators loaded on transmission line: Analysis and applications," *J. Appl. Phys.*, vol. 116, p. 083705, Aug. 2014.
- [92] T. Zhang, W. Xiong, B. Zhao, J. Shen, C. Qiu, and X. Luo, "Equivalent circuit analysis of 'U'-shaped split ring resonators," *J. Mod. Opt.*, vol. 62, pp. 901–907, June 2015.
- [93] A. Abduljabar, X. Yang, D. Barrow, and A. Porch, "Modelling and Measurements of the Microwave Dielectric Properties of Microspheres," *IEEE Trans. Microw. Theory Tech.*, vol. 63, pp. 4492–4500, Dec. 2015.
- [94] R. Bojanic, V. Milosevic, B. Jokanovic, F. Medina-Mena, and F. Mesa, "Enhanced Modelling of Split-Ring Resonators Couplings in Printed Circuits," *IEEE Trans. Microw. Theory Tech.*, vol. 62, pp. 1605–1615, Aug. 2014.

- [95] J. Baena, J. Bonache, F. Martín, R. Sillero, F. Falcone, T. Lopetegi, M. Laso, J. Garcia-Garcia, I. Gil, M. Portillo, and M. Sorolla, “Equivalent-circuit models for split-ring resonators and complementary split-ring resonators coupled to planar transmission lines,” *IEEE Trans. Microw. Theory Tech.*, vol. 53, pp. 1451–1461, Apr. 2005.
- [96] A. Borja, A. Belenguer, J. Cascon, H. Esteban, and V. Boria, “Wideband Passband Transmission Line Based on Metamaterial-Inspired CPW Balanced Cells,” *IEEE Antennas Wireless Propag. Lett.*, vol. 10, pp. 1421–1424, 2011.
- [97] J. Naqui, M. Duran-Sindreu, and F. Martín, “Modeling Split-Ring Resonator (SRR) and Complementary Split-Ring Resonator (CSR) Loaded Transmission Lines Exhibiting Cross-Polarization Effects,” *IEEE Antennas Wireless Propag. Lett.*, vol. 12, pp. 178–181, 2013.
- [98] J. Naqui, L. Su, J. Mata, and F. Martín, “Analysis of transmission lines loaded with pairs of coupled resonant elements and application to sensors,” *J. Magn. Magn. Mater.*, vol. 383, pp. 144–151, June 2015.
- [99] L. Su, J. Naqui, J. Mata-Contreras, and F. Martín, “Modeling metamaterial transmission lines loaded with pairs of coupled split-ring resonators,” *IEEE Antennas Wireless Propag. Lett.*, vol. 14, pp. 68–71, 2015.
- [100] S. I. Latif, L. Shafai, and S. K. Sharma, “Bandwidth enhancement and size reduction of microstrip slot antennas,” *IEEE Trans. Antennas Propag.*, vol. 53, pp. 994–1003, Mar. 2005.
- [101] H. C. Rhim and O. Buyukozturk, “Electromagnetic properties of concrete at microwave frequency range,” *ACI Mater. J.*, vol. 95, pp. 262–271, May 1998.
- [102] R. A. Dalke, C. L. Holloway, P. McKenna, M. Johansson, and A. S. Ali, “Effects of reinforced concrete structures on RF communications,” *IEEE Trans. Electromagn. Compat.*, vol. 42, pp. 486–496, Nov. 2000.

- [103] W. Su, O. A. Hazim, I. L. Al-Qadi, and S. M. Riad, "Permittivity of portland cement concrete at low RF frequencies," *Mater. Eval.*, vol. 52, pp. 496–502, Apr. 1994.
- [104] E. Richalot, M. Bonilla, M.-F. Wong, V. Fouad-Hanna, H. Baudrand, and J. Wiart, "Electromagnetic propagation into reinforced-concrete walls," *IEEE Trans. Microw. Theory Tech.*, vol. 48, pp. 357–366, Mar. 2000.
- [105] R. Paknys, "Reflection and transmission by reinforced concrete – numerical and asymptotic analysis," *IEEE Trans. Antennas Propag.*, vol. 51, pp. 2852–2861, Oct. 2003.
- [106] M. Dehmollaian and K. Sarabandi, "An approximate solution of scattering from reinforced concrete walls," *IEEE Trans. Antennas Propag.*, vol. 56, pp. 2681–2690, Aug. 2008.
- [107] S. Jiang and S. V. Georgakopoulos, "Optimum wireless powering of sensors embedded in concrete," *IEEE Trans. Antennas Propag.*, vol. 60, pp. 1106–1113, Feb. 2012.
- [108] B. C. Wadell, *Transmission Line Design Handbook*. Boston: Artech Print on Demand, May 1991.
- [109] E. Chen and S. Chou, "Characteristics of coplanar transmission lines on multilayer substrates: modeling and experiments," *IEEE Trans. Microw. Theory Tech.*, vol. 45, pp. 939–945, June 1997.
- [110] R. N. Simons, *Coplanar Waveguide Circuits, Components, and Systems*. New York: Wiley-IEEE Press, 1 edition ed., Apr. 2001.
- [111] Y. Y. Iossel, *The Calculation of Electrical Capacitance*. PN, 1971.
- [112] F. E. Terman, *Radio Engineers' Handbook*. McGraw-Hill Book Company, inc, 1st edition ed., 1943.
- [113] F. W. Grover, *Inductance Calculations: Working Formulas and Tables*. Courier Corporation, 2004.